Ubiquitin-mediated Regulation of Necroptosis

Thesis submitted for the degree of
Doctor of Philosophy (PhD)

by

Laura Ramos García

Cell Death and Immunity Team
The Institute of Cancer Research
University of London

October, 2019

Declaration

Work for this thesis was conducted under the supervision of Professor Pascal Meier in the Cell Death and Immunity Team, The Breast Cancer Now Toby Robins Research Centre, The Institute of Cancer Research, London.

I confirm that the work presented in this thesis is my own. Where information has been derived from other sources, I confirm that this has been clearly stated in this thesis.

Laura Ramos García

London, October 2019

Abstract

Regulated cell death is a fundamental cellular process that is critical for the development and survival of multicellular organisms. Cell death and inflammation are essential to restore tissue homeostasis following tissue malfunction, injury or infection. Deregulation of the signalling pathways that trigger cell death can lead to the development of diseases such as cancer or autoimmunity. Necroptosis is a type of regulated cell death characterized by the rupture of the plasma membrane and the release of the inflammatory components into the tissue microenvironment thereby triggering inflammation and immune responses. The pseudokinase MLKL constitutes the last effector of the necroptotic pathway. Currently, little is known about the mechanism of regulation of MLKL and how it mediates cell death execution.

In this thesis, I studied the role of Ubiquitin (Ub) in regulating MLKL-mediated necroptosis. I discovered that MLKL is heavily ubiquitylated during necroptosis and that this contributes to its killing activity. Ubiquitylation of MLKL occurs downstream of its phosphorylation by RIPK3. Using mass spectrometry, I have identified four lysine (K) residues of MLKL that serve as ubiquitin acceptor sites. Among these, I have focused on K219 which is positioned within MLKL's pseudoactive site. Ubiquitylation at this site is important in controlling MLKL's killing potential as cells derived from *Mlkl*^{K219R} knockin animals are less sensitive to undergo necroptosis. Mechanistically, ubiquitylation enhances the ability of phosphorylated MLKL (P-MLKL) to form higher order oligomers at the plasma membrane.

I have also investigated MLKL's interactome and its localization during necroptosis. I identified several desmosomal proteins that interact with MLKL. In line with this, I found that P-MLKL preferentially localizes to regions of the plasma membrane where cells are in contact with one another.

In summary, my study describes how the Ub system modulates MLKL activity and identifies cell-cell contact points as 'hotspots' for MLKL recruitment.

Acknowledgements

I would first like to thank my supervisor Professor Pascal Meier for giving me the opportunity to do my PhD in his lab. Pascal has been an invaluable mentor and has guided me through the difficulties and exciting discoveries in the past four years. His support, guidance and contagious passion for science have been motivational for me. I am also grateful for all his contribution with time and immense knowledge that have made my PhD experience truly stimulating.

To the members of the Meier Lab, both past (Otto, Isabel, Celia, Agnes, Giammy and Ale) and present (Rebecca, Sidonie, Tencho, Kunzah, Emily, Jazz, Marta, Maria, Hyojin, Arnaud and Carmo): you have contributed immensely to my professional and personal development during this time and it has been a pleasure working with you all. In particular, I would like to thank Tencho, for teaching me cloning and Sidonie, for her help with my project and continuous support. Special thanks to Giammy, who closely supervised me during the early stages of my PhD and whose ideas and constant positivity have been instrumental. I am also particularly grateful to Ale, who never failed to give me good advice and support at the most challenging times. Ale, not only you are a great scientist, but also an amazing person. Marta and Hyojin, thanks for your friendship and for always being there to enjoy life outside the lab.

To all my collaborators outside the Meier Lab: thanks to Dr. Lu Yu and Dr. Mercedes Pardo Calvo, from the lab of Dr. Jyoti Choudhary, who performed all mass spec analysis described in this thesis. Thanks to Professor James Murphy, who has provided insightful advice for the MLKL project and will be performing the *in vitro* ATP binding assays. Special thanks to Professor Jason Upton, who has provided the MCMV virus, as well as to Anne Bridgeman and Professor Jan Rehwinkel, who will be conducting future *in vivo* experiments with such virus.

To all my friends at the ICR (Aaron, Andri, Doug, Erik, Eva, Joe, Mara, Nikos, Patty and Radhika): I am immensely happy to have you during my Ph.D. The group has been a source of friendship, good advice and incredible time outside the ICR. Thanks for all the great memories of Friday evenings and the trips to

Lake District and the Basque Country. You have been a wonderful support network.

To Itzi: we both embarked on PhD studies at the same time and undoubtedly, you have been a key person during all this time. Thanks for all the great moments we have shared- your friendship is one the best things I have gained from my time in London.

Many people have supported me and encouraged me during the high and lows of my PhD (and during my whole life). Nothing would have been the same without my friends and family from Spain. In particular, I would like to thank:

Agur and Jokin: for their continuous support and for sending me plenty of serrano ham and croquettes during my time in London.

Nazaret, my beloved cousin: thanks for always encouraging me to take on new adventures. You are an amazing person!

Carolina: we clicked the first day of university and you have been a best friend ever since.

Nagore: my oldest friend, thanks for always being there for me. I cannot be more excited for the times coming ahead!

Julen, my other half: for supporting me in my decision to study abroad. You are smart, caring, supportive and a fascinating person. Thanks for all your love throughout these years. *Maite zaitut!*

Finally, I thank my parents and sister, Begoña, Alvaro and Elisa: for your unconditional love and continuous support during all my life. I wholly attribute everything I have accomplished so far to your endless encouragement. *Ama y aita*, thanks for all the efforts you have made to satisfy my curiosity for learning.

Table of Contents

List of Figures

List of Tables

Abbreviations

4HB	4-Helix bundle
A	Alanine
ACD	Accidental cell death
ACN	Acetonitrile
Ambic	Ammonium Bicarbonate
AMP	Adenosine monophosphate
AP	Affinity Purification
APC/C	Anaphase promoting complex cyclosome
ATP	Adenosine triphosphate
BIR	Baculovirus IAP repeat
BMDM	Bone marrow derived macrophage
BN-PAGE	Blue native-PAGE
BSA	Bovine serum albumin
C-	Carboxi- (COO^-)
C-spine	Catalytic spine
C/ Cys	Cysteine
Cas9	Crispr associated protein 9
CCD	Catalytic cysteine domain
cDAMP	constitutive DAMP
cDNA	Complementary DNA
cFLIP	FLICE inhibitory protein
$cFLIP_L$	cFLIP long isoform
cFLIPs	cFLIP short isoform
cGAMP	sensor cGMP-AMP
cGAS	cGMP-AMP (cGAMP) synthase
CHIP	Hsp70-interacting protein
ChlAA	Chloroacetamide

cIAP	Cellular inhibitor of apoptosis protein
CIM	cIAP interacting motif
CIP	Calf Intestinal phosphatase
CLRs	C-type lectin receptors
COO^-	Carboxyl group
CRISPR	Clustered regularly interspaced short palindromic repeats
Ctrol	Control
CYLD	Cylindromatosis
DAI	DNA-dependent activator of IFN-Regulatory Factors
DAMP	Danger associated molecular pattern
DAPI	4′,6-diamidino-2-phenylindole
DD	Death domain
DED	Death effector domains
dH_2O	Deionized water
Di-Gly (K-GG)	Di-glycine
DISC	Death inducing signaling complex
DKO	Double Knock out
DMEM	Dulbecco's modified eagle medium
DMSO	Dimethyl sulfoxide
DNA	Deoxyribonucleic acid
dNTP	Deoxynucleotide
DOX	Doxycycline
DR3	Death receptor 3
DR6	Death receptor 6
Ds	Double stranded
DTT	Dithiothreitol
DUB	Deubiquitinating enzyme
E	Glutamate
e.g.	Exempli gratia (for example)

E1	Enzyme 1 (Ubiquitin activating)
E2	Enzyme 2 (Ubiquitin conjugating)
E3	Enzyme 3 (Ubiquitin ligase)
ECL	Enhanced chemiluminescence
EDTA	Ethylene diamine tetra acetic acid
ESCRT-III	Endosomal sorting complexes required for transport III machinery
et al.	et alia
F	Phenylalanine
FA	Formic acid
FACS	Fluorescence activated cell sorting
FADD	Fas-associated dead domain
FBS	Fetal bovine serum
G	Glycine
GFP	Green fluorescence protein
GMP	Guanisine monophosphate
GSH	Glutathione
GST	Glutatione-S-transferase
GTP	Guanosine triphosphate
h	Human
H	Histidine
HECT	Homologous to E6AP C-terminus
hMLKL	Human MLKL
HP	Hydrophobic patches
HRP	Horse-radish peroxidase
HSV	Herpes simplex virus
I	Isoleucine
i.e.	id est
IAV	Influenza A virus
IBR	In-between RING

ICD	Immunogenic cell death
iDAMPs	Inducible DAMPs
IFN	Interferon
IKK	IkB kinases
IL-1β	Interleukin 1 beta
IP	Immunoprecipitation
IRF	IFN-regulatory factors
ISGs	Interferon stimulated genes
IκBα	Inhibitor of Kappa B Alpha
K (Lys)	Lysine
K63-UIM	K63-linkage ubiquitin interacting motif
KD	Kinase Domain
KDa	Kilodalton
KI	Knockin
KO	Knockout
KSR1	Kinase suppressor of Ras 1
L	Leucine
LB medium	Luria Broth Medium
LC-MS/MS	Liquid Chromatography-Tandem Mass Spectroscopy
LPS	Lipopolysaccharides
LUBAC	Linear Ub chain assembly complex
Lys	Lysine
Lys-C	Lysyl Endopeptidase
m	Murine
M1	N-terminal Methionine
M1-SUB	M1-linkage specific Ub binder
MAPK	Mitogen activated protein kinase
MAVS	Mitochondrial antiviral signalling
MCMV	Murine cytomegalovirus

MDF	Mouse dermal fibroblast
MEF	Mouse embryonic fibroblasts
MK2	MAPK-activated protein kinase-2
MLKL	Mixed lineage kinase domain-Like
mMLKL	Murine MLKL
MOMP	Membrane outer membrane permeabilization
mRNA	Messenger RNA
MS	Mass Spectrometry
mTNF	Membrane-bound TNF
MyD88	Myeloid differentiation primary response 88
N-	Amino- ($NH3^{+}$)
Nec-1	Necrostatin-1
NEMO	NF-κB essential modulator
NF-κB	Nuclear Factor-κB
NLR	NOD-like receptors
NMR	Nuclear magnetic resonance
NOD2	Nucleotide binding oligomerization domain containing protein 2
NSA	Necrosulfanamide
NZF	Npl4 zinc finger
P-MLKL	Phosphorylated MLKL
P/S	Penicillin/ Streptomycin
PAGE	Polyacrylamide gel electrophoresis
PAM	Protospacer adjacent motif
PAMP	Pathogen associated molecular pattern
PCR	Polymerase chain reaction
Peli1	Pellino 1
PI	Propidium iodide
PIP	Phosphatidylinositol Phosphate
PKA	Protein kinase A

PLA	Proximity ligation assay
PRR	Pattern recognition receptors
PsKD	Pseudokinase domain
PTM	Post-translational modification
Q	Glutamine
R	Arginine
R-spine	Regulatory spine
RBR	Ring between ring
RCD	Regulated cell death
RHIM	Rip homotypic interaction motif
RING	Really interesting new gene
RIPK1	Receptor interacting protein kinase 1
RIPK1i	RIPK1 kinase inhibitor
RIPK3	Receptor interacting protein kinase 3
RIPK3i	RIPK3 kinase inhibitor
RLRs	RIG-I-like receptors
RNA	Ribonucleic Acid
RT	Room Temperature
RT-qPCR	Real Time quantitative PCR
S	Smac Mimetics
SD	Standard Deviation
SDS	Sodium dodecyl sulfate
SDS-PAGE	SDS-polyacrylamide electrophoresis
Ser	Serine
siRNA	Short-interfering RNA
sTNF	Soluble TNF
SV40	Simian Vacuolating 40
T	Threonine
T1-IFN	Type I Interferon

TAB1/2	TAK binding protein 1 and 2
TACE	TNF-converting enzyme
TAK1	Transforming growth factor beta-activated kinase 1
TBK1	Tank binding kinase 1
TFA	Trifluoroacetic acid
TGF	Transforming growth factor
TLR	Toll-Like receptor
TMT	Tandem mass tag
TNF /T	Tumor necrosis factor
TNFR1	TNF receptor 1
TNFR2	TNF receptor 2
TNFSF	TNF superfamily
TRADD	TNFR-associated DD protein
TRAF	TNF receptor-associated Factor
TRAIL	TNF-related apoptosis inducing ligand
TRAILR1	TRAIL receptor 1
TRAILR2	TRAIL receptor 2
TRIF	Toll/IL-1 receptor (TIR) domain-containing adaptor protein inducing IFNβ
TRIM25	Tripartite motif 25
TSZ	Tumor necrosis factor, Smac Mimetics, Caspase inhibitor zVAD-fmk
TUBE	Tandem ubiquitin binding entity
Ub	Ubiquitin
UBA	Ubiquitin associated
UBAN	Ubiquitin binding in ABIN and NEMO
UBD	Ub binding domain
UCD	Ub conjugating domain
UF	Ultrafiltration
UFD	Ub fold domain
V	Valine

vMLKL	Viral MLKL
WGA	Wheat germ agglutinin
WT	Wild-type
Z	Caspase inhibitor zVAD-fmk
ZBP1	Z-DNA binding protein 1
β-ME	β-mercaptoethanol

Symbols and Units

α	Alpha
γ	Gamma
μ	10^{-6}
°C	Degree centigrade
h	Hour
M	Molar
m	10^{-3}
min	Minutes
n	10^{-9}
o/n	overnight
sec	Second
β	Beta
ε	Epsilon
κ	Kappa
g	Grams
L	Litter

1. Introduction

1.1. The Ubiquitin System

Proteins are decorated with an array of reversible chemical post-translational modifications (PTMs) that regulate their spacial and temporal functions [1]. Considering their high occurrence, ~480.000 unique PTM sites have been catalogued in the mammalian proteome, they have emerged as an important regulatory layer that greatly expands the functional diversity of a proteome [1, 2]. Indeed, PTMs are crucial to control many dynamic cellular processes such as cell proliferation, migration and death [3]. While the human proteome contains hundreds of different types of PTMs, one of the most studied of these modification is ubiquitylation [4], which regulates many essential cellular processes in eukaryotes. Ubiquitylation refers to the covalent attachment of ubiquitin (Ub) to residues on substrate proteins. Although it was first discovered as a signal for protein degradation, it is now clear that it also controls the assembly of signalling hubs by regulating protein interactions and activities [5-8].

1.1.1. Ubiquitin

Ub is a small (76 amino acid, 8.6 KDa) protein present in all eukaryotes that can be conjugated via its C-terminal glycine (G) residue to one or more lysine (K, Lys) residues of a substrate protein [9]. Ub is highly conserved among all eukaryotes, which suggests a high evolutionary pressure to maintain its structure [10]. The cellular Ub pool is derived from four genes. *Uba52* and *Rsp27a* encode a single copy of Ub fused to the ribosomal proteins L40 and S27A, respectively. In contrast, *Ubb* and *Ubc* encode multiple Ub~Ub fusion proteins [11]. Therefore, following *Ubb* and *Ubc* translation, a single Ub molecule is generated by cleavage of the peptide bond between the individual Ub moieties [5].

1.1.2. Ubiquitylation

Ubiquitylation is a sequential multi-enzyme cascade that results in the formation of an isopeptide bond between the carboxy group of the C-terminus of Ub and the ε-amino group of the K residue in the substrate protein **(Figure 1.1B)** [11, 12]. When a substrate is modified via conjugation of a single molecule of Ub the process is known as monoubiquitylation, whereas if several sites within the substrate are conjugated with a Ub molecule it is referred to as multi-monoubiquitylation [10].

Ub itself contains seven K residues (K6, K11, K27, K29, K33, K48 and K63), which together with its N-terminal methionine (M1) provide eight attachment sites for additional Ub molecules **(Figure 1.1A)** [13]. Thus, successive rounds of Ub attachment can give rise to substrates with polyubiquitin (polyUb) chains **(Figure 1.1B,** bottom). In this process, the Ub molecule attached to the substrate is conjugated with a second molecule of Ub via any of the eight possible attachment sites giving rise to a di-Ub chain. Further rounds of catalysis may result in polyUb chains which can be homotypic, when all the Ub molecules within a chain are connected though the same K or M1, or heterotypic, (also known as mixed linkages chains) if the conjugation is made via different Ks of Ub [14, 15]. Homotypic polyUb chains are also named based on the residue used for the conjugation of Ub molecules (e.g. K48-linked chains). While conjugation of Ub to a K is made via an isopeptide bond, when M1 is utilized for conjugation, instead of a K, it creates a canonical peptide bond **(Figure 1.1B)** [16, 17]. Linkages occurring between the C- and N-termini of Ub result in a head-to-tail polyUb chain and thus M1-linked chains are also known as linear chains [18]. An extra layer of complexity is added by the fact that a Ub molecule in a chain may be ubiquitylated at multiple K residues, forming a ‘branched’ (also known as ‘forked’) structures [19]. Altogether, the different types of Ub chains result in distinct chain topologies that act as a highly complex ‘Ub code’ to transmit information.

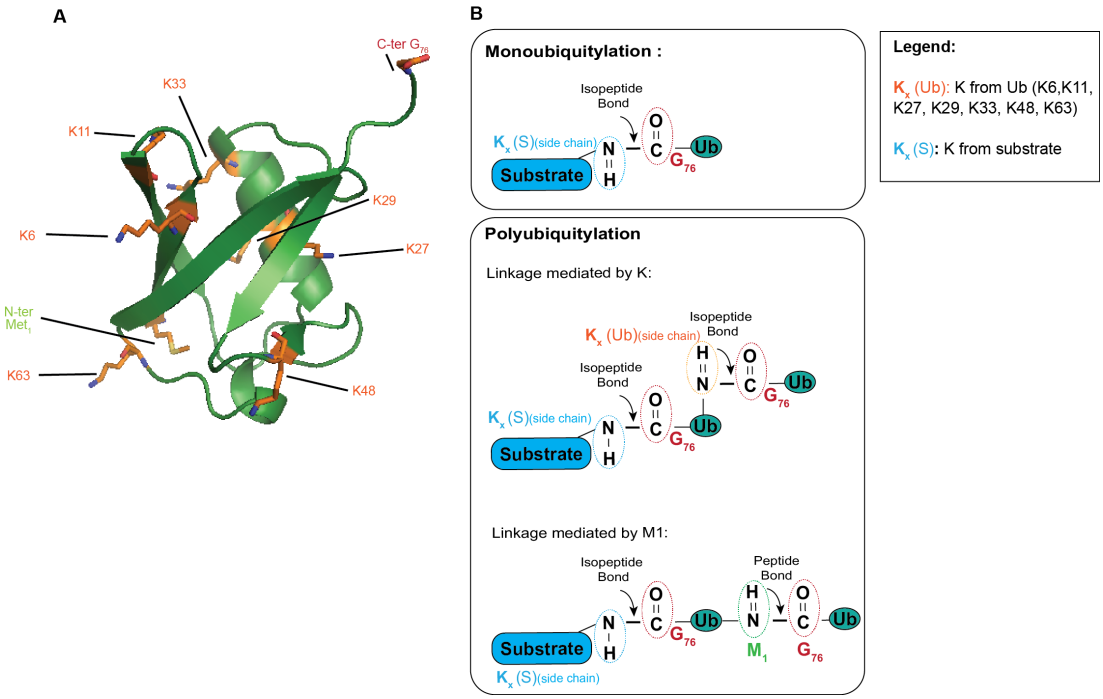

Figure 1.1. Ub linkages and types of Ub chains.

(A) Structure of Ub (green) showing the seven K residues (K), the N-terminal methionine (M1) and the C-terminal glycine (G76). Any of the seven K or the M1 residue in the molecule of Ub can serve as an attachment site for Ub chain formation. The side chains of the seven K, the M1 and G76 residues are represented as sticks and colored by atom type (carbon atoms in orange, nitrogen atoms in blue, oxygen atoms in red and sulfur atoms in yellow). PBD: 1UBQ [20]. **(B)** Schematic representation of the isopeptide bond formed between the carboxyl group (COO-) of the Ub's G76 and the epsilon-amino group (ε-NH3+) of the substrate's K (monoubiquitylation). Any of the eight potential attachment sites within the molecule of Ub can be used to form Ub chains (polyubiquitylation). Conjugation of Ub to any of the K residues is made via an isopeptide bond, whereas if Ub is attached to the M1 residue, a canonical peptide bond is formed. When the same acceptor residue is utilized along the entire Ub chain, they are referred to as 'homotypic' chains. If different acceptors are used to form a chain, they are named 'heterotypic' chains. Branched chains may occur when a single molecule of Ub is conjugated via more than one of its acceptor sites.

1.1.2.1. Enzymes mediating the Ub cascade

The Ub code is dynamically regulated by specific (1) sets of enzymes (E) that mediate ubiquitylation of a given substrate ('writers'): E1s, E2s and E3 ligases; (2) a set of deubiquitinating enzymes (DUBs) that cleave Ub ('erasers') or edit the type of linkage and (3) a set of Ub-binding proteins that recognize ubiquitylated substrates and transmit the Ub signal into a cellular outcome ('readers') [21-24].

The human E1 enzymes UBA1 and UBA6 control ubiquitylation of all targets [21]. They carry MoeB/ThiF motifs, which serve to provide structural stability and bind adenosine triphosphate (ATP) as well as Ub. They also harbor a catalytic cysteine domain (CCD) that contains the E1 active site cysteine (C, Cys) which acts as a receptor for Ub. Moreover, they have a Ub fold domain (UFD) that mediates the recruitment of specific E2s [21, 22, 25, 26]. E1-mediated activation of Ub involves three steps: First, the E1 binds ATP and Ub, catalyzing the adenylation of Ub. Second, the adenylated Ub reacts with the catalytic Cys, producing a covalent thioester bond between the catalytic Cys and the C-terminus of Ub **(Figure 1.2A step 1)**. A second molecule of Ub is then loaded and remains associated to the adenylation active site. Third, as a consequence of charging the E1 with Ub, it undergoes conformational changes that expose binding sites for E2s, thereby forming E1-E2 complexes. The recruitment of E2s by the Ub-loaded E1 allows the transfer of Ub from the E1 to the E2's catalytic C [26] **(Figure 1.2A step 2)**.

There are at least 40 E2s in the human genome [27]. All E2 enzymes possess a core Ub conjugating domain (UCD), which contains the catalytic Cys. This domain also interacts with the Ub-charged E1s with high affinity [22, 26]. Following Ub transfer to E2s, E2~Ub enzymes interact with E3 ligases to catalyze substrate ubiquitylation [22] **(Figure 1.2A step 3)**. Once Ub has been transferred to the substrate, the E2 dissociates from the E3 allowing it to be recharged with Ub for the next round of transfer. Individual E2s can interact with different E3s [22]. While some E2s initiate the formation of Ub chains, other E2s mediate chain elongation [22]. In addition, E2s can sometimes determine the

linkage specificity of the Ub chains, such as the UBE2N-UBE2V2 E2 complex that exclusively forms K63-linked chains [22, 28].

E3 ligases present the largest group of enzymes in the ubiquitylation cascade, and their main role is to provide specificity due to their interaction with the substrate as well as with the Ub-loaded E2 [22, 29]. All E3s harbor a specific E2~Ub binding domain and are classified based on their mechanism of Ub transfer to substrates [12]. To date, three classes of E3 ligases have been identified **(Figure 1.2B)**. These are grouped based on the presence of a RING (Really Interesting New Gene), HECT (Homologous to E6AP C-terminus) or RBR (Ring Between Ring) domain. RING-bearing E3s make up the largest class, with over 600 E3s identified in the human genome [30]. The RING domain confers the Ub ligase activity by directly binding to the Ub-conjugated E2 to stimulate Ub transfer [30]. A substrate binding domain within the RING E3 ligase simultaneously recruits the substrate, bringing it in close proximity to the Ub-loaded E2 and thereby allowing the transfer of Ub from the catalytic Cys of the E2 to the Ub-acceptor Lys of the substrate [12]. In contrast to the RING-E3 ligases, HECT and RBR E3s contain catalytic C that first accepts Ub from the E2, forming a covalent Ub~E3 thioester intermediate, prior to conjugation of Ub to the substrate. There are 28 HECT E3s and 12 RBR E3s in humans [31, 32]. RBR E3s contain two RING domains (RING1 and RING2) and an in-between RING (IBR) domain. Thus, in RBR E3 ligases the RING1 interacts with the Ub~E2 complex (similarly to RING-E3s) and the Ub is then transferred to the catalytic Cys located in the RING2 domain [32]. Subsequently, Ub is transferred to the target substrate **(Figure 1.2A step 4)**. Since the mechanism of catalysis in HECT and RBR E3s involves the transfer of Ub to the E3, the Ub chain linkage specificity depends on the E3 itself [12].

Ubiquitylation is a reversible event and the conjugated Ub chains can be cleaved by DUBs, a family of Ub specific proteases [5] **(Figure 1.2A step 5)**. The Ub molecules that are cleaved from substrates can be recycled for subsequent ubiquitylation events of other substrates **(Figure 1.2A step 6)**.

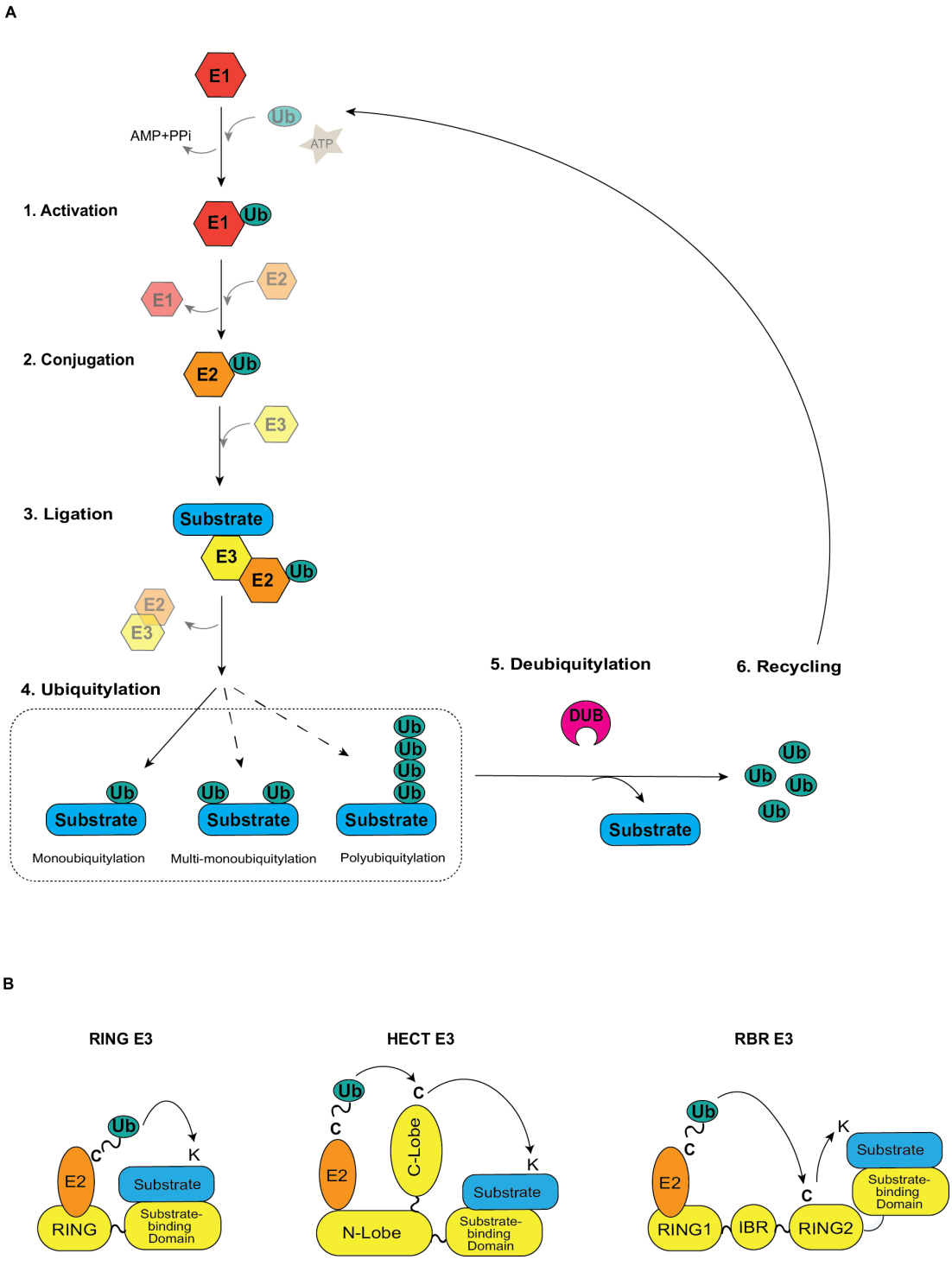

Figure 1.2. The enzymatic cascade of ubiquitylation and types of E3 ligases

(A) First, the E1 is loaded with two Ub molecules, one at its adenylation domain and the other linked to the catalytic Cys **(1. Activation)**. The activated Ub linked to the E1 C, is then transferred to the C in the active site of the E2 **(2. Conjugation)**. The E2 dissociates from the E1 and engages with a cognate Ub ligase (E3), which recruits substrates **(3. Ligation)**.

The E3 mediates the transfer of Ub to the substrate **(4. Ubiquitylation)** and the E2 dissociates from the E3 allowing it to be recharged with Ub for the next round of transfers. Substrates can be ubiquitylated in single K (monoubiquitylation) or in two or more K (multi-monoubiquitylation) residues. Alternatively, Ub might be conjugated to an existing Ub molecule on a substrate, giving rise to polyubiquitylated substrates. Ubiquitylation of substrates can be reversed by the action of DUBs **(5. Deubiquitylation)**. Deubiquitylation leads to the release of free Ub, which subsequently can be recycled to ubiquitylate other substrates **(6. Recycling)**. **(B)** Schematic representation of the mode of action of each class of E3 ligases.

1.1.3. The structure behind the Ub Code and its recognition by UBDs

Ub is structurally characterized by a β-grasp fold with a flexible six-residue C-terminal tail that allows its conjugation to target proteins [20]. The Ub surface presents hydrophobic patches (HP) centered around isoleucine 36 (I36 patch), isoleucine 4 (I4 patch) and 44 (I44 patch) [10] **(Figure 1.3A)**. These patches are critical for the recognition of Ub by proteins with Ub-binding domains (UBDs). UBDs are structurally diverse domains that can non-covalently bind to ubiquitylated substrates, distinguishing different types of Ub modifications with high specificity [33]. Importantly, the different type of Ub chains take up distinct topologies, resulting in unique structural properties and therefore allowing efficient recognition by specific UBDs [34]. For instance the Npl4 Zinc Finger (NZF) UBD of Tak1-binding protein (TAB2) preferentially binds to K63-linked chains whereas the Ub Associated Domain (UBAN) domain of NF-κB essential modulator (NEMO) specifically recognizes M1-linked chains [35].

MonoUb is often recognized by different types of UBD, via interaction with the I44 patch, although other structural features might also contribute to its recognition [33]. Additionally, the conformational diversity that the Ub molecule presents in solution also plays a role in the Ub-UBD interaction [36]. In the case of polyUb chains, their topology is very diverse and has been best characterized in the context of homogenous chains [10]. In particular, K48-, K6- and K11-chains usually acquire a compact conformation, where the Ub molecules within the chain might interact via their hydrophobic patches **(Figure 1.3 B.1 and 2)** [10]. On the other hand, K63-, K29-, K26- and M1-chains mostly display an 'open conformation' with minimal contact between the individual Ub molecules **(Figure 1.3 B3 and 4)** [35].

To achieve this linkage-specificity a variety of mechanisms are exploited by UBDs. For instance, UBDs might recognize the specific positioning of the HPs along the chain as well as adjacent binding surfaces on the Ub molecule [33]. Additionally, the tandem arrangement of UBDs also define linkage specificity based on the length of the linker sequence between the UBDs [37]. Lastly, structures of Ub chains in complex with UBDs have revealed that the structure of

K48-, K63- and M1-linked chains adopt slightly different conformations when they are bound by UBDs [33, 38, 39]. Although the binding affinity of individual UBDs for Ub is generally low (in the 1-15 μM range) [15], the aforementioned mechanisms allow a high avidity interaction. Additionally, other factors might affect the Ub-UBD interaction, including the oligomerization, specific localization or PTMs affecting the Ub-binding protein [33].

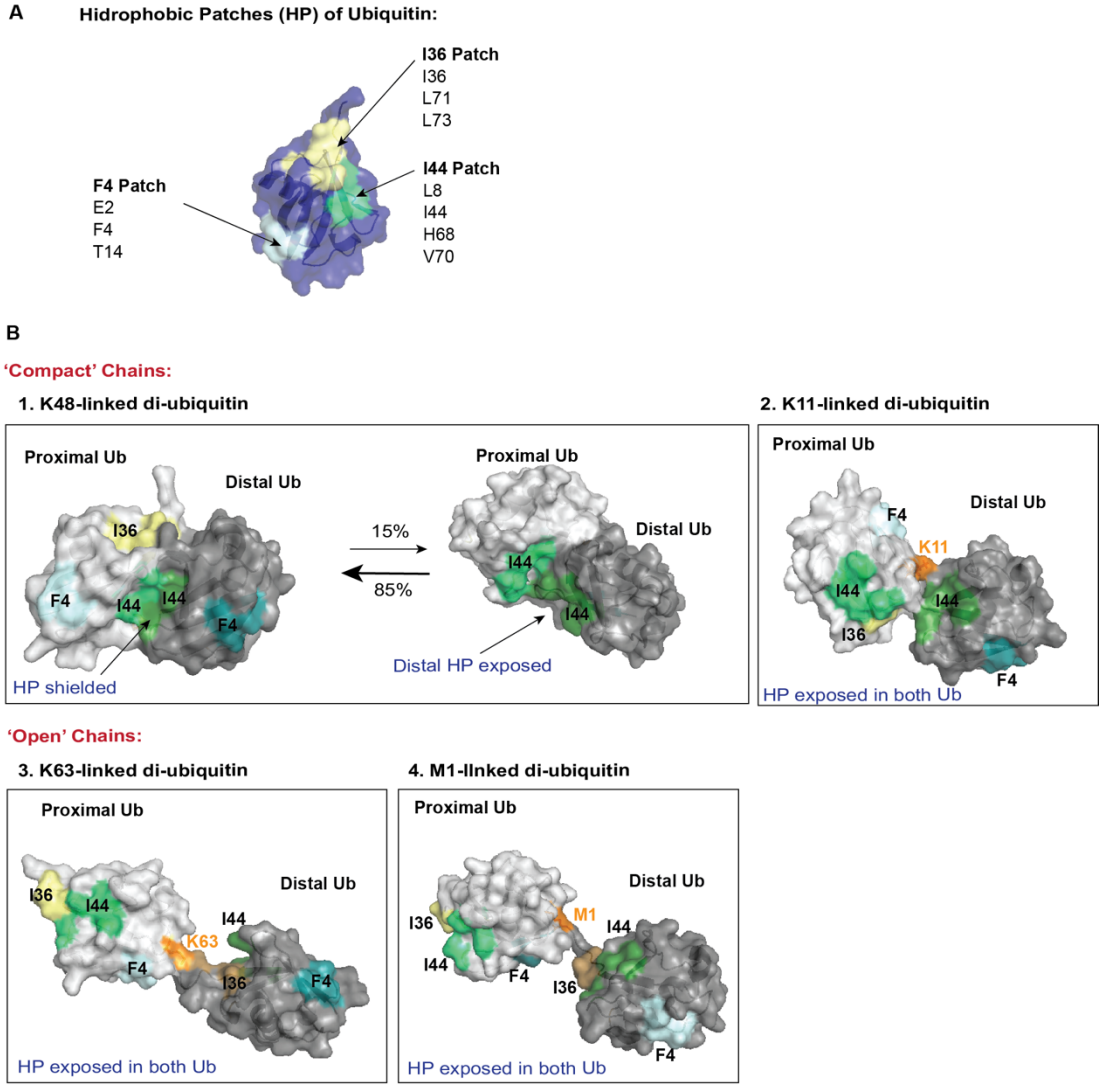

Figure 1.3. Structural representation of Ub and di-Ub chains.

(A) Crystal structure of Ub (PDB:1UBQ [20]) indicating the hydrophobic patches (HP). I44 HP (green) is comprised by L8, I44, H68 and V70. The I36 HP (yellow) is made of I36, L71 and L73 residues and the F4 HP (blue) includes residues Q2, F4 and T14. **(B)** Ub conformation of di-Ub chains. Proximal (that is, linked via its K residue) and distal (that is, linked via its C terminus) Ub are shown in light or dark grey, respectively. The surface of Ub is represented and the HP are indicated using the same color scheme as in A. K48-linked **(B1)** and K11-linked **(B2)** di-Ub are shown as examples of 'compact' chains. For K48- two alternative conformations are represented, one showing a partial exposure of the I44 HP (right), whereas in the other (left) is shielded. PDB K48-diUb: 1AAR left [40]; 2PE9 right [41]. PDB K11-diUb: 2MBO [42]. K63-linked **(B3)** and M1-linked **(B4)** di-Ub chains represent 'open' conformations. PDB K63-diUb: 2JF5 [35]. PDB M1-diUb:2W9N [35].

1.1.4. Biological consequences of ubiquitylation

The different topologies of Ub chains are recognized by specialized UBDs, resulting in a particular cellular outcome. The downstream signalling triggered will depend on various factors, including the type of Ub linkage, the anchoring site of Ub within the substrate or the length of polyUb chains [34].

K48-linked polyUb chains constitute the most common type of linkage, targeting substrates for proteasomal degradation [19]. Although an initial study indicated that proteins require at least a tetra-Ub chain to be efficiently targeted for degradation [43], more recent studies have shown that two di-Ub modifications were a better signal for degradation compared to a single tetra-Ub chain [44]. In addition, K48-linked chains have been shown to be present in substrates that are not degraded, suggesting that this type of linkage can have a regulatory role independent of proteolysis [45].

The K63-linked chain type has many well-studied non-degradative roles, including the regulation of endocytosis, vesicular trafficking, DNA damage response and immune signalling [46]. For instance, following a DNA double strand break, several E3 ligases are recruited to the site of damage. These E3s ubiquitylate histones to assemble a stable signalling platform [47]. As a result, this ubiquitylation induces the arrest of the cell cycle, pausing transcription and allowing DNA repair [47]. Additionally, K63-linked chains play a key role in the activation of Nuclear Factor κB (NF-κB) signalling downstream of many inflammatory pathways (described below) [10].

M1-linked chains are also important modulators of inflammatory signalling pathways, acting in conjunction with K48- and K63-linked chains to induce NF-κB activation [18]. To date, the linear Ub chain assembly complex (LUBAC) is the only known mammalian E3 ligase that mediates this type of Ub linkage [48]. Stimulation of Tumor Necrosis Factor (TNF) or Nucleotide binding Oligomerization Domain Containing protein 2 (NOD2) signalling leads to the formation of signalling complexes, which are conjugated with K63-linked chains and other types of Ub chains. As a result, these polyUb chains recruit the

Transforming growth Factor beta-activated kinase 1 (TAK1) complex via its K63-linked Ub binding subunits TAK binding protein 1 and 2 (TAB1/2). The K63-linked chains also recruit LUBAC that in turn conjugates M1-linked chains to components of the signalling complex [49, 50]. This enables recruitment of the IkB kinase α (IKK) complex via its Ub adaptor NEMO [51, 52]. The proximity between TAK1 and IKK allows TAK1-mediated activation of IKK, resulting in efficient activation of NF-κB-mediated transcription.

Similar to K48-, K11-linked chains also act as signal for proteasomal degradation. K11-linked chains mainly target cell cycle regulatory proteins for degradation. UBE2S is currently the only known K11-specific E2. This E2 is preferentially used by the Anaphase Promoting Complex Cyclosome (APC/C) [19]. Nonetheless, recent studies suggest that APC/C can also form branched chains, which seem to be more efficient than homotypic K11-chains in targeting protein for degradation [53-55].

The biological functions of K6-, K27-, K29- and K33-linked chains are less clear as they have not been studied extensively. K6-linked chains are present at low abundance (less than 1% of total linkages) and accumulate on mitochondria during mitophagy [56, 57]. Similarly, K27-linked chains have also been linked to mitophagy [58]. K29-linked polyUb chains are involved in Wnt-signalling and epigenetic regulation [19, 59, 60]. Lastly, K33-linkages have been implicated in post-Golgi membrane protein trafficking [61].

Of note, the formation of heterotypic and branched chains allows for more complex signalling outputs [47]. Accordingly, K63/M1-linked hybrid Ub chains occur during NF-κB signalling, and might account for the necessary proximity of TAK1 to activate IKK [17, 62]. Substrate recognition by the proteasome may also be influenced by the presence of hybrid chains. For example, K11/K48-branched Ub chains interact with the proteasome with higher affinity than homotypic chains [54]. Lastly, K48/K63-branched chains can protect chains from deubiquitylation by Cylindromatosis (CYLD) [63].

Compared with polyubiquitylation, the functions of monoubiquitylation are less well characterized. Monoubiquitylation has been implicated in the modulation of transcription, DNA damage repair and DNA replication [64]. Additionally, site-specific monoubiquitylation has also been described to affect the activation state of proteins. For instance, monoubiquitylation of K-Ras at K147 (located in the guanine nucleotide-binding motif) leads to enhanced guanosine triphosphate (GTP) loading and consequently enhanced K-Ras activation [65].

Together, the conjugation of Ub to target proteins influences diverse biological processes, ranging from protein degradation to inflammation, cell death and immunity.

1.2. Inflammation and maintenance of tissue homeostasis

Homeostasis refers to the body's capability of maintaining a stable internal environment [66]. Tissue homeostasis is essential to prevent diseases, such as diabetes and cancer, and thus contributes to the survival of multicellular organisms. Different external challenges, including infection or injury, as well as non-pathogenic factors such as certain chemicals, trauma, or tissue malfunction can result in tissue damage, and disrupt tissue homeostasis. Multicellular organisms respond to tissue damage by coordinating an inflammatory response that helps to restore tissue homeostasis.

Local inflammation is initiated by stimulation of a defined repertoire of Pattern Recognition Receptors (PRRs). These receptors are highly expressed in cells of the immune system, such as macrophages, dendritic cells and neutrophils. They recognise conserved features of pathogens, known as Pathogen Associated Molecular Patterns (PAMPs) [66]. PRRs can also be activated upon recognition of certain endogenous factors known as Danger Associated Molecular Patterns (DAMPs), which are released by damaged or dying cells, leading to an inflammatory response under sterile conditions [67]. In particular, barrier tissues (such as the skin, the intestine, the lung and the liver), which are continuously exposed to exogenous agents, contain tissue resident immune cells that can initiate an inflammatory response upon pathogen detection or tissue malfunction [68].

The best-characterized PRRs comprise the Toll-Like Receptors (TLRs), the RIG-I-like receptors (RLRs), NOD-like receptors (NLR) and C-type lectin receptors (CLRs) (**Figure 1.4)** [69]. The cytosolic DNA sensor cGMP-AMP (cGAMP) synthase (cGAS) and DNA-Dependent Activator of IFN-Regulatory Factors (DAI; also termed ZBP1) are also important sensors of damage or tissue malfunction [70]. The aforementioned receptors are activated following infection or tissue damage. In particular, viruses can induce the activation of RIG-I-like receptors as well as DNA sensors. Toll-like receptors as well as NOD-like receptors are known to be engaged following bacterial infections, and C-type lectin receptors are activated in response to fungi and some bacteria [69].

Once activated, PRR transduce signals that converge on the activation of the IFN-regulatory factors (IRF) family of transcription factors, which lead to the transcription of Type I Interferon (T1-IFN) and/or NF-κB activation. In general, T1-IFN is the predominant response following viral infections whereas acute bacterial infections are associated with strong NF-κB activation. The activation of these transcriptional responses, results in the production of a plethora of pro-inflammatory cytokines as well as genes involved in antiviral/microbicidal responses. The inflammatory mediators also recruit lymphocytes and other immune mediators from the circulation. Together, this results in the elimination of the infection and/ or injury, and the restoration of tissue homeostasis. Importantly, such inflammatory responses need to be tightly regulated because inflammation needs to be resolved once the source of infection and/or damage is removed. Otherwise, excessive and uncontrolled inflammation can lead to the development of chronic inflammatory diseases such as cancer [71].

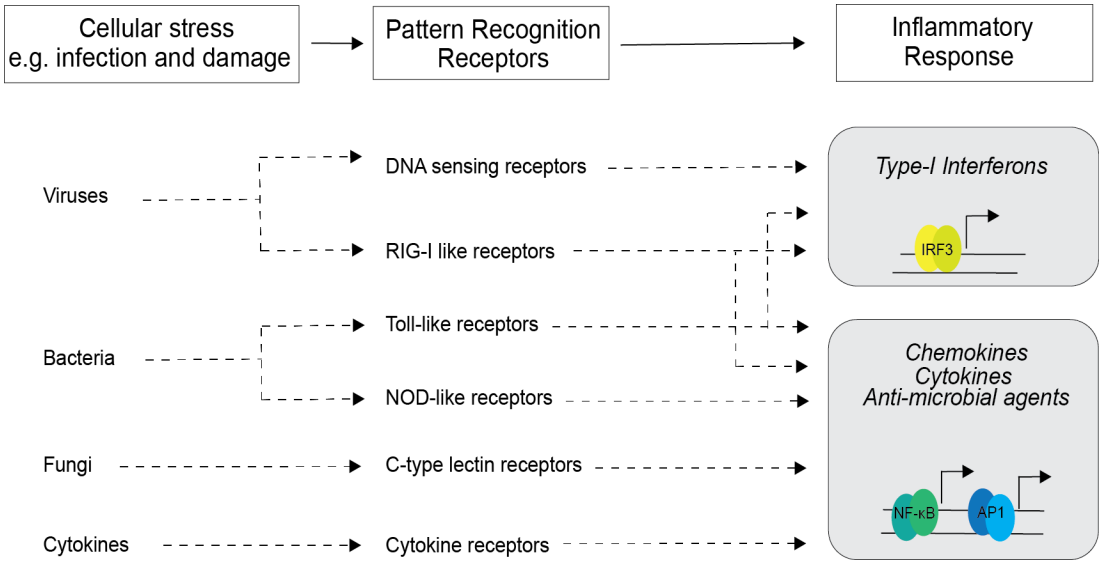

Figure 1.4. Pattern recognition signalling.

Schematic representation of the major types of pattern recognition receptors (PRRs), their ligands and the transcription factors that are activated upon receptor stimulation.

1.2.1. Role of cell death in inflammation and the immune response

Cell death constitutes a central characteristic of tissues undergoing an inflammatory response [72]. Cell death can be triggered in many different ways. Cells can die in an unregulated manner through accidental necrosis (accidental cell death, ACD) following physical damage, or via regulated cell death (RCD). RCD refers to the type of cell death that is actively initiated and executed by controlled mechanisms [73, 74]. Importantly, it is becoming clear that RCD, hereinafter 'cell death', has a physiological role during inflammation and host defense response. Mechanistically, pro-inflammatory cytokines, induced upon PRR stimulation, such as TNF and T1-IFN, are capable of inducing cell death in an autocrine/paracrine fashion through stimulation of their receptors, TNFR1 and IFNAR, respectively. Additionally, stimulation of some PRRs (such as certain TLRs or ZBP1) can intrinsically trigger cell death programmes [70].

The contribution of cell death as a host defense mechanism has been best characterized in the context of pathogen infection. Upon infection by intracellular pathogens, such as viruses and certain bacteria, cell death constitutes a crucial defense strategy in various ways. On one hand, engagement of cell death pathways in infected cells helps to prevent pathogen dissemination and damage to the tissue by ending the potential replicative niche. Additionally, the death of an infected cell might result in the release of a set of inflammatory molecules, providing a mechanism to amplify/modulate the inflammatory response.

Of note, contemporary studies have defined an important role for dying cells in the initiation of adaptive immune responses [75, 76]. In this case, the dying cell not only provides the source of antigen (e.g. antigens from pathogens or neoantigens generated during carcinogenesis) but also releases a set of immune stimulatory molecules (adjuvants) that mobilize the immune system [75]. Importantly, the ability of a dying cell to activate the immune system is influenced by the modality of cell death that is triggered, since this affects the type of molecules that are released upon death. Thus, the term 'immunogenic cell death (ICD)' refers to those cell death modalities that are capable of promoting an adaptive immune response [75]. Of note, ICD can occur not only

upon pathogen infection but also in sterile conditions, particularly following chemotherapy and radiotherapy [77]. In this context, mutations, genomic instability and cellular stress give rise to neo-antigens. Adjuvancy is provided by the release of DAMPs that stimulate PRRs. Two different classes of DAMPs have been described: constitutive DAMPs (cDAMPs) and inducible DAMPs (iDAMPs) [75]. The former refers to those immune-stimulatory cellular factors, which are constitutively present and are released upon death. On the other hand, iDAMPs are factors that are produced or modified following stimulation of certain cell death and/or inflammatory pathways [75]. For instance, production of NF-κB-dependent cytokine expression or release of Interleukin 1 beta (IL-1β), as a result of Caspase-1 activation, are considered iDAMPs [75, 78]. The specific cocktail of iDAMPs produced upon engagement of different types of cell death pathways and their efficacy to stimulate adaptive immune responses remains ill-defined.

1.3. Regulated Cell Death Modalities

RCD pathways are triggered as a mechanism to guarantee tissue homeostasis in both physiological and pathological settings. There are many different pathways that control RCD [79]. These include (but are not limited to): (1) intrinsic apoptosis: characterized by mitochondrial outer membrane permeabilization (MOMP); (2) extrinsic apoptosis: triggered by plasma membrane receptors and propagated by caspase-8; (3) necroptosis: relying on Receptor Interacting Protein Kinase 3 (RIPK3) and Mixed Lineage Kinase Like (MLKL); and (4) pyroptosis: depending on the formation of plasma membrane pores by Gasdermin-D [79].

Each type of RCD manifests distinct morphological changes upon cell demise. Indeed, these features were historically utilized to classify cell death modalities. Apoptotic cells are characterized by cytoplasmic shrinkage, chromatin condensation, nuclear fragmentation and plasma membrane blebbing. Additionally, apoptotic cells also form small vesicles (apoptotic bodies) which are engulfed and degraded by neighboring cells **(Figure 1.5, left).** In contrast, necroptosis involves the swelling of the cytoplasm and organelles, followed by rupture of the plasma membrane, and the release of the cellular content into the tissue micro-environment [80] **(Figure 1.5, right)**.

The extent to which these RCD modalities are more or less immunogenic is still a matter of intense investigation. Because apoptotic cells retain plasma membrane integrity, this cell death modality is generally considered to be immunologically silent. In contrast, cell death by necroptosis or pyroptosis, both characterized by plasma membrane disruption is thought to be immunogenic. Nevertheless, it is now clear that apoptosis can also be immunogenic in certain settings [78, 81].

In the following Sections I will focus on the regulation of extrinsic apoptosis and necroptosis as they are closely connected.

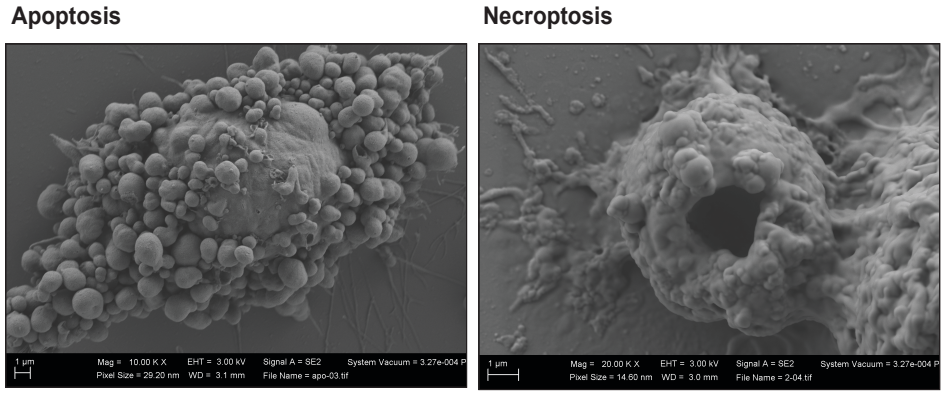

Figure 1.5. Necroptotic and apoptotic cell death

Representative electron microscope image of a cell (HT-29) undergoing extrinsic apoptosis (left) and necroptosis (right). Images were acquired by David Robertson and Gianmaria Liccardi.

1.3.1. Discovery of the necroptotic pathway

Although the morphological features of necrotic cell death were described in the 19th century [82], it was always considered to be accidental and thus, without a molecular mechanism. Nonetheless, in 2005 a new type of caspase-independent cell death was described, presenting necrosis-like morphology. This type of cell death occurred following activation of death receptors under conditions where caspase-8 was inhibited [83]. The fact that cell death was prevented by necrostatin-1 (Nec-1), which inhibits the activity of the kinase Receptor Interacting Protein Kinase 1 (RIPK1), indicates that this cell death modality, thereafter named necroptosis, is molecularly regulated [84].

Mechanistically, two core components comprise the necroptotic machinery: the kinase RIPK3 and the pseudokinase MLKL, the executioner of necroptosis. RIPK3 activates MLKL, which drives cell death by compromising plasma membrane integrity. Although RIPK3 can be activated by different stimuli, necroptosis is best studied following TNF signalling (described in Section 1.4 and 1.5) where the activation of kinase RIPK1 is also required to trigger necroptosis. The remaining necroptotic triggers are described in Section 1.6.

One important role of necroptosis is to limit viral infections, particularly suppressing the spread of viruses that can block apoptosis via inhibition of caspase-8. Besides suppressing viral infections, necroptosis may also suppress tumorigenesis, particularly in situations where the activity of caspase-8 is compromised or lost [85-87]. Considering the above, it is generally thought that necroptosis might have evolved as a 'back-up' strategy to kill cells in which caspase activity is compromised [88]. However, recent evidence indicates that apoptosis and necroptosis programmes can sometimes run in parallel [89, 90]. Importantly, not every tissue has the same propensity to die by necroptosis. Keratinocytes of the skin, for example, readily die by necroptosis [91]. In contrast to the skin, cells in the intestine mainly undergo apoptosis [91, 92]. This raises the question as to whether the relative abundance of the various signaling effectors within the apoptotic and necroptotic pathways also regulate the engagement of one pathway or another.

1.4. TNF-induced cell death

1.4.1. TNF Superfamily

TNF constitutes one of the most extensively studied cytokines. This is due to its important role in mediating inflammation and cell death. TNF belongs to the TNF superfamily (TNFSF) of proteins, which is comprised of 19 ligands (cytokines) and 29 receptors in humans [93]. Upon binding of these cytokines to their cognate receptors, they initiate a transcriptional response of proinflammatory genes or may also in certain cases trigger cell death (extrinsic apoptosis/necroptosis). Although members of the TNF superfamily share structural similarities, each cytokine only binds to a selective set of receptors, thereby enhancing the regulatory flexibility and complexity of the system [94]. Binding of the cytokine to the receptor induces clustering of the receptors via their cytoplasmic tails. This in turn promotes the recruitment of key adaptor proteins, which ultimately initiate signal transduction [93]. TNFSF of receptors can be classified into (1) signaling receptors and (2) death receptors **(Figure 1.6).**

On the one hand, the signaling receptors promote the recruitment of TNF Receptor-associated Factor (TRAF) proteins though a TRAF-binding motif, which is localized in the cytoplasmic tail of these receptors [94]. These adaptor proteins are crucial for activation of NF-κB and Mitogen Activated Protein (MAP) kinase signaling cascades, ultimately coordinating cellular responses that mediate proliferation, differentiation and inflammation. On the other hand, the other subfamily of receptors (death receptors) harbor a ‘death domain’ (DD) within the cytoplasmic region. The DD is a six alpha helical fold that mediates homotypic interactions. Accordingly, these receptors recruit other DD-containing adaptor proteins [94]. In humans there are six DD-containing receptors TNFR1, FAS, DR3, TRAILR1, TRAILR2 and DR6 [95]. They are referred as ‘death receptors’ due to their ability to trigger cell death upon overexpression or cytokine binding [96-98]. Indeed, FAS and TRAILR1/2 recruit the adaptor Fas-Associated Dead Domain Protein (FADD), which in turn binds to caspase-8 resulting in the activation of extrinsic apoptosis [95]. On the other hand, TNFR1,

DR3 and possibly, DR6 recruit the adaptor TNFR-associated DD protein (TRADD). TRADD harbors both a DD in the C-terminus and a TRAF-binding motif in the N-terminus [99]. Consequently, receptors that recruit TRADD have the ability to drive both TRAF-mediated NF-κB activation and cell death. Therefore, these receptors are 'dual signaling' receptors [96]. In addition to the subfamilies described above, some TNFSF receptors lack a functional signalling domain and therefore function as 'decoy receptors' that inhibit TNFSF signalling [100].

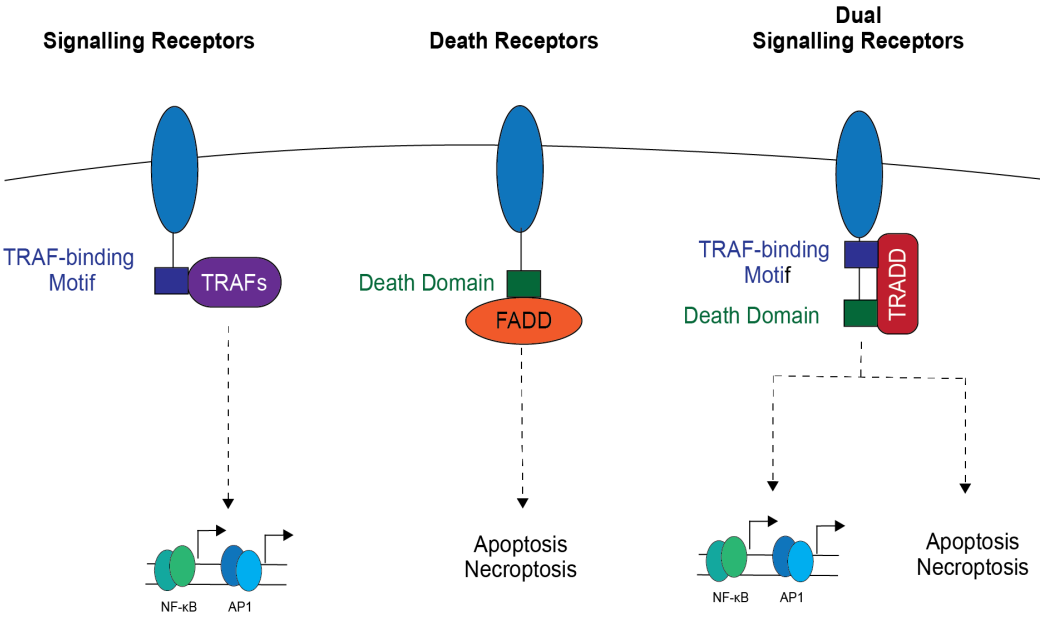

Figure 1.6. Signalling pathways initiated by the TNFSF.

The 29 receptors of the TNFSF of proteins in the human genome can be classified into three subtypes based on the adaptor proteins recruited to their cytoplasmic tails in addition to 'decoy receptors' which lack functional intracellular domains. The largest group of receptors contain a TRAF binding motif and recruit TRAF proteins leading to inflammatory signalling cascades. The death receptor family recruits the adaptor protein FADD, which can initiate cell death programs. Dual signalling receptors induce the engagement of TRADD that can lead to both, activation of inflammatory programs as well as cell death.

1.4.2. Signalling induced by TNF

TNF is initially produced as a Type II transmembrane protein and is secreted upon cleavage by the metalloprotease TNF-converting enzyme (TACE) [101]. Both, the transmembrane form and the soluble TNF (mTNF and sTNF, respectively) act as homotrimers [93]. The production and secretion of TNF takes place in response to engagement of PAMP/DAMP receptors by cells of the immune system, and constitutes a key cytokine for restoration of tissue homeostasis following tissue damage. mTNF and sTNF can bind to TNF Receptor 1 and 2 (TNFR1 and TNFR2). While TNFR1 can be activated by both forms of TNF, TNFR2 is only activated by mTNF, despite the binding of sTNF with high affinity [102]. Consequently, sTNF is capable of signaling in a paracrine and systemic fashion though TNFR1 engagement whereas mTNF-mediated signaling relies on cell-cell contacts. These differences are dictated by an extracellular region in the TNFR2 known as the 'stalk region', which effectively prevents responsiveness to sTNF [102].Moreover, only TNFR1 contains a DD. Therefore, TNFR2 is unable to drive cell death. Further, while TNFR1 is ubiquitously expressed in most tissues (although at low levels), the expression of TNFR2 is highly regulated and restricted to certain cells of the immune system (mainly the lymphoid compartment) as well as to endothelial and neurological tissues [100]. Despite these differences, commonalities exist nonetheless. Namely, both receptors are capable of activating cell survival mechanisms. The best characterized signaling events downstream of TNFR2 involve the activation of canonical and non-canonical NF-κB pathways. Similarly, the default response upon activation of TNFR1 in most human and mouse cells is survival via NF-κB activation [103]. In fact, TNF-induced killing upon TNFR1 engagement is actively repressed my multiple checkpoints and only unleashed under certain circumstances (discussed below) [104].

1.4.2.1. TNFR1-signalling for survival: Complex-I

Binding of TNF to TNFR1 leads to the oligomerization of the receptor and formation of a membrane-bound pro-inflammatory multiprotein complex referred to as Complex-I of TNFR1 signaling [103]. The DD of TNFR1 mediates the

assembly of this complex, by binding to TRADD and the kinase RIPK1 through their respective DDs [105-107]. Although the interaction of RIPK1 with TNFR1 is relatively weak in comparison to TRADD [108], RIPK1 interaction with TRADD is strong, making TRADD necessary for RIPK1 recruitment to TNFR1 upon TNF stimulation [107]. RIPK1 constitutes a central player in the TNF signaling transduction pathway by actively controlling the balance between cell survival and cell death (discussed in 1.4.2.2). Besides recruiting RIPK1, TRADD also serves as a platform for TRAF2, which in turn brings in the E3 Ub ligases cellular Inhibitor of Apoptosis Protein 1 and 2 (cIAP1 and cIAP2) [50, 109-111]. TRAF2 interacts through its N-terminal cIAP Interacting Motif (CIM) with the BIR1 and UBA domains of the cIAPs [112, 113]. Within this complex, RIPK1, and other components recruited to the complex, are rapidly conjugated with Ub chains of various types [114]. In particular, cIAP-mediated conjugation of K63- and K11-linked Ub chains to RIPK1 allows the recruitment of LUBAC, comprised by HOIL-1, SHARPIN and the central catalytic subunit HOIP [50]. LUBAC linearly ubiquitylates several components of Complex-I including RIPK1, TRADD and TNFR1. Together, these Ub chains serve as a scaffold for recruitment and efficient retention of the kinase complexes TAK1/TAB2/TAB3 and IKKα/IKKβ/NEMO (IKK complex) [50, 51, 115, 116]. Ub-mediated recruitment allows TAK1-mediated phosphorylation of IKKβ. This leads to its autophosphorylation inducing IKK activation [117]. Active IKK phosphorylates the NF-κB inhibitor IκBα, inducing its proteasomal degradation and allowing the translocation of NF-κB to the nucleus to initiate gene transcription [118]. TAK1 also initiates mitogen activated protein kinases (MAPKs) signalling pathways [119, 120]. Thus, formation of Complex-I results in the activation of transcriptional programmes inducing the expression of pro-survival and pro-inflammatory genes **(Figure 1.7A)**. Of note, the requirement of RIPK1 for TNFR1-induced activation of NF-κB is cell type dependent [121].

1.4.2.2. RIPK1 as a key player in TNFR1-signalling

Although in most cell types TNF stimulation has a pro-survival function, it also induces the formation of a secondary cytosolic complex, referred to as Complex-II, which can trigger cell death. The decision between activation of cell survival

(NF-κB) or cell death relies on several checkpoints. These checkpoints directly control the cytotoxic potential of RIPK1 via complex PTMs including phosphorylation, ubiquitylation and caspase-mediated cleavage [104].

RIPK1 is one of the most heavily ubiquitylated proteins in Complex-I. While this can contribute to Ub-dependent activation of NF-κB, ubiquitylation of RIPK1 also suppresses its cytotoxic potential. This is mediated by at least two mechanisms. First, Ub chains seem to tether RIPK1 to Complex-I, thereby suppressing its transition to the death-inducing Complex-II. Second, the Ub chains on RIPK1 allow activation of TAK1, IKK and MAPK-activated Protein Kinase-2 (MK2) [51] [122]. The activation of these kinases not only facilitates NF-κB-mediated expression of pro-survival genes, such as FLICE inhibitory protein (cFLIP) which suppress Complex-II formation (described in 1.4.3.1) [123] but also allows kinase mediated phosphorylation and inactivation of RIPK1 (described below).

In line with the key role of RIPK1 ubiquitylation in preventing cell death, genetic deletion of the main E3 ligases for RIPK1, namely *cIAP1/2*-/- and *HOIP*-/- (catalytic subunit of LUBAC) in mice, results in embryonic lethality. Such embryos die during early embryonic development due to aberrant RIPK1-dependent cell death of endothelial cells [124, 125]. Similarly, pharmacological depletion of the cIAPs impairs TNF-induced RIPK1 ubiquitylation, and enhances Complex-II formation, resulting in cell death in many human and murine cell types [126, 127]. Mechanistically, the UBA domain of cIAP1 is necessary to repress RIPK1 autoactivation [113]. A functional UBA domain in cIAP1 (*cIAP1*^{UBAwt}) increases the number of ubiquitylated K on RIPK1 and enhances K48-linked polyubiquitin chains on RIPK1 in comparison to *cIAP1*^{UBAmut} cells [113]. Thus, ubiquitylation of RIPK1 directly controls RIPK1 kinase activity by suppressing its auto-activation and targeting active RIPK1 for proteasomal degradation independently of IKK and MK2 [113]. In addition to cIAPs and LUBAC, the E3 Ubiquitin ligase Mind Bomb-2 (MIB2) also represses the cytotoxic potential of RIPK1 by ubiquitylating K residues in the linker and C-terminal portion [128]. Mechanistically, ubiquitylation of RIPK1 in Complex-I by MIB2 interferes with RIPK1 oligomersation and suppresses its kinase activity and cell death [128]. The ubiquitylation status of RIPK1 can also be modulated

by DUBs, such as CYLD. CYLD is recruited to Complex-I via SPATA2-mediated binding to HOIP and can hydrolyze the Ub modifications present in the complex, thereby regulating NF-κB signalling and cell death [129-133]. Some other DUBs, such as A20, which is induced upon NF-κB activation, functions as a negative feedback mechanism to terminate signalling [134].

As indicated above, RIPK1's cytotoxic activity is also modulated in a phosphorylation-dependent manner. Depending on cell type, TAK1 and IKK can suppress RIPK1-mediated cell death independently of their role in driving NF-κB activation [104, 135]. Mechanistically, TAK1-mediated activation of p38 results in the activation of MK2, which directly phosphorylates RIPK1, suppressing its killing activity [136-138]. In particular, MK2 phosphorylates RIPK1 at serine (S) 320 and S335 (S321 and SS336 in mice) preventing its activation [136-138]. Additionally, IKKα and IKKβ both directly phosphorylate RIPK1 in Complex-I at multiple sites, also suppressing its cytotoxic potential [139]. In particular, IKK-mediated phosphorylation of RIPK1 at S25 inhibits RIPK1 kinase activity preventing TNF-mediated RIPK1-kinase dependent cell death [140]. Lastly, the kinases Tank Binding Kinase 1 (TBK1) and IKKε have also been reported to phosphorylate RIPK1 in Complex-I, thereby limiting Complex-II formation [140, 141].

1.4.2.3. Formation and regulation of Complex-II

The assembly of Complex-II occurs in the cytoplasm several hours after the formation of Complex-I [103]. The regulation of RIPK1 by ubiquitylation and phosphorylation is crucial as RIPK1 can nucleate Complex-II. In addition to RIPK1, Complex-II assembly involves the adaptor protein FADD, procaspase-8 and c-FLIP. In certain tissues where it is present, the kinase RIPK3 is also recruited. Likewise, caspase-10, which is present only in human cells, can also be recruited to Complex-II [103, 142] **(Figure 1.7B)**. The formation of Complex-II is initiated when RIPK1 dissociates from Complex-I and recruits the adaptor protein FADD, procaspase-8, cFLIP and RIPK3 [143]. The potential of Complex-II to trigger either apoptosis or necroptosis critically depends on caspase-8,

cFLIP and RIPK3 [144]. While caspase-8 activation is essential to trigger apoptosis, the activation of RIPK3 is required for necroptosis.

Expression of cFLIP (induced upon NF-κB activation) plays a key role in suppressing Complex-II-mediated cell death. The long isoform of cFLIP ($cFLIP_L$) closely resembles the domain architecture of full-length procaspase-8, but lacks the active site catalytic Cys residue and proteolytic activity. Binding of pro-caspase-8 to FADD, promotes the recruitment of $cFLIP_L$ via heterodimerization with caspase-8 through a cooperative and hierarchical binding mechanism [145]. The heterodimers of procaspase-8: $cFLIP_L$ exhibit localized enzymatic activity and reportedly cleave RIPK1, RIPK3 and CYLD [146-150]. In particular, caspase-8 cleaves RIPK1 after D325 and cleavage at this site is crucial to prevent RIPK1-dependent aberrant cell death (apoptosis and necroptosis) during development, as shown with the generation of *Ripk1*$^{D325A/D325A}$ mice that died at mid-gestation [149]. Considering this, it is likely that cleavage of RIPK1 might cause cell death signalling complexes to fall apart, thereby terminating death signal. Cleavage of CYLD by caspase-8 is reported to take place after D215 [149, 150]. However, *Cyld*$^{D215A/D215A}$ mice are viable, indicating that cleavage by caspase-8 at this site is not required to prevent necroptosis [149]. Of note, this cleavage is unlikely to affect its catalytic activity, given that CYLD's USP catalytic domain spans amino acids 589-947. Caspase-8 reportedly cleaves RIPK3 after D328 to prevent necroptosis [147]. Nonetheless, the *in vivo* relevance this cleavage site remains to be investigated.

Recruitment of $cFLIP_L$ to pro-caspase-8-FADD complexes also precludes the assembly of procaspase-8 oligomers inhibiting full activation of Caspase-8 thereby preventing apoptosis [145]. Consequently, TNF kills when its NF-κB activation capacity is reduced or blocked so that $cFLIP_L$ is not upregulated. Absence (or low levels) of $cFLIP_L$ allows FADD-mediated recruitment of procaspase-8, via interaction through their respective Death Effector Domains (DEDs). Subsequently, additional procaspase-8 molecules are recruited leading to the formation of a filamentous activation platform [151, 152]. This filamentous structure allows proximity-induced dimerization of procaspase-8 molecules which in turn leads to autoproteolytic cleavage allowing full caspase-8 activation.

This form of caspase-8 can cleave downstream effectors caspases such as caspase-3 and -7, as well as the protein BID engaging apoptosis [153].

As indicated above, activation of caspase-8 also inhibits the necroptotic pathway by cleaving RIPK1, RIPK3 and CYLD [146-150]. Therefore, under conditions where caspase-8 activity is suppressed, active RIPK1 accumulates to high levels, which allows the activation of RIPK3 and necroptosis (detailed in Section 1.5). Accordingly, *caspase-8*$^{-/-}$ mice die at embryonic development stage E10.5 due to defects in the vascularization of the yolk sac [154, 155]. The lethality of *Caspase8*$^{-/-}$ mice is partially rescued by co-deletion of TNFR1 (lethality delayed to E17.5), and completely rescued by co-deletion of RIPK3 and MLKL, indicating that the phenotype is due to aberrant necroptosis [156, 157]. Consistent with the importance of caspase-8's catalytic activity to inhibit necroptosis, catalytically inactive caspase-8 (*Casp8*^{C362A}) knock-in mice also die at E10.5 due to MLKL-driven necroptosis [149]. Likewise, mutant animals that harbor a non-cleavable RIPK1 variant (*Ripk1*^{D325A}) also die at E10.5, highlighting the importance of caspase-8-mediated cleavage of RIPK1 in safeguarding cell viability [148, 149].

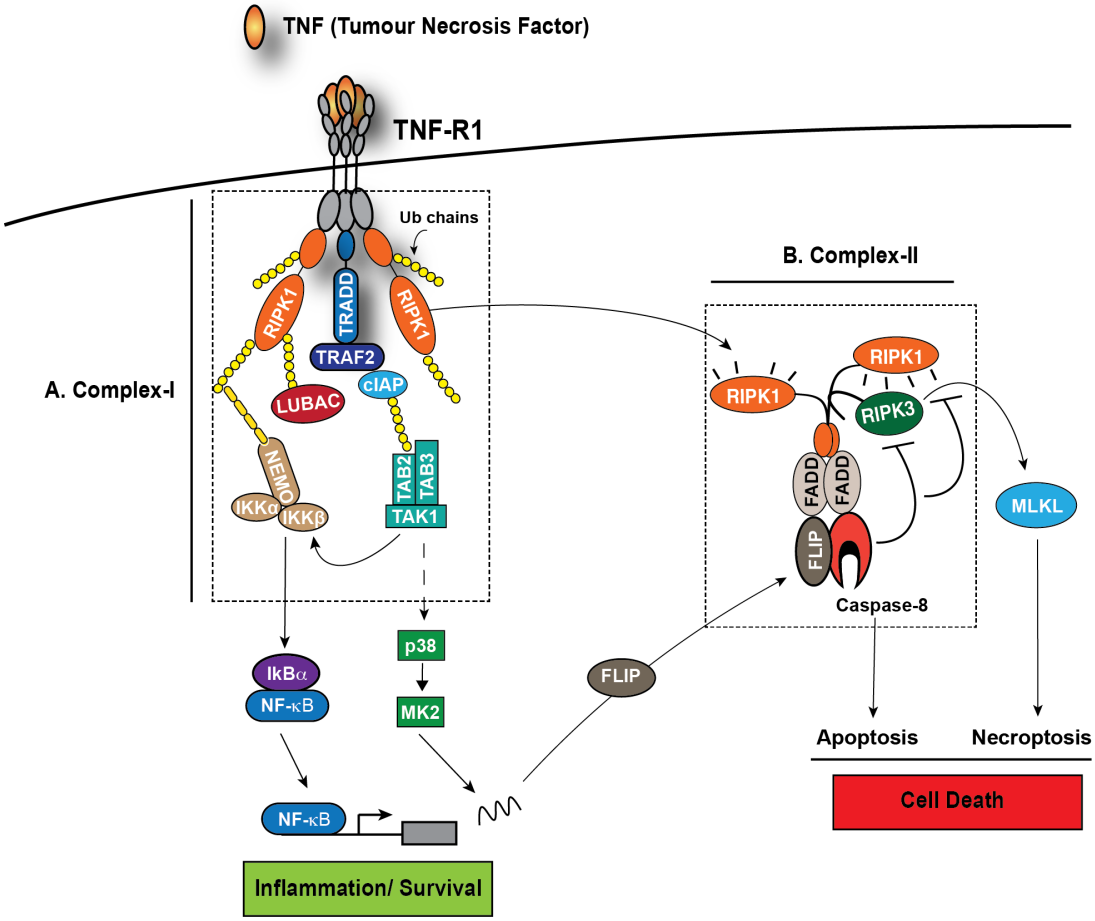

Figure 1.7. TNFR1 signalling and the crosstalk of cell survival and cell death.

(A) Following the binding of TNF to TNFR1, TNFR1 binds to TRADD, which recruits RIPK1, TRAF2 and cIAP1/2 to form TNFR1 signalling Complex-I. The E3 Ub ligases cIAP1 and 2 add polyUb chains to RIPK1 and other components of the signalling complex. These Ub chains also recruit LUBAC, which adds M1-linked polyUb chains to components of Complex-I. Polyubiquitylated RIPK1 recruits TAB2, TAB3 and TAK1. TAK1 subsequently activates the p38>MK2 axis as well as IKK complex (made up of NEMO, IKKα and IKKβ). The IKK complex then activates NF-κB signalling, which leads to the transcription of anti-apoptotic genes — such as FLIP. When the integrity of Complex-I is perturbed (e.g. upon loss of cIAPs), a secondary cytoplasmic complex is formed, termed Complex-II. **(B)** Complex-II can contain TRADD, RIPK1, FADD, Caspase-8, FLIP, and RIPK3. The formation of caspase-8: FLIP heterodimers results in sublethal activation of caspase-8. This results in the suppression of both apoptosis and necroptosis. Upon loss of cFLIP, for example when NF-kB-mediated induction of cFLIP is compromised, caspase-8 is fully activated and triggers apoptosis. If Caspase-8 activity is compromised, RIPK1 accumulates and induces RIPK3 activation. This, in turn, activates MLKL to induce necroptosis. Figure adapted from [104].

1.5. Key events in TNF-induced necroptosis

Necroptosis is best characterized downstream of TNFR1 signalling. Nonetheless, other pathways, which are described in Section 1.6, can also engage necroptosis (e.g. other DRs, TLRs and ZBP1). Of note, they all converge at the level of RIPK3 activation.

1.5.1. RIPK1-mediated activation of RIPK3

TNF-induced necroptosis requires activation of RIPK1 and RIPK3. Both kinases are comprised by an N-terminal Serine/Threonine (Ser/Thr) kinase domain and a C-terminal disordered region harboring a RIP Homotypic Interaction Motif (RHIM domain) **(Figure 1.8A)**. The RHIM domain consists of a 10 amino acids sequence that mediates the interaction between RIPK1 and RIPK3 [142, 158]. Mechanistically, the RHIMs of RIPK1 and RIPK3 assemble into heterodimeric filamentous structures, which present biochemical and biophysical characteristics of β-amyloids. These characteristics include a filamentous morphology, the propensity to bind thioflavin and Congo red, and the high stability [159]. Assembly of this amyloid-like structure, frequently referred to as the 'necrosome', is essential to activate RIPK3 [160, 161]. A Nuclear magnetic resonance (NMR) spectroscopy study indicates that the consensus sequence of four amino acids, present at the end of the RHIM domain (IQIG in RIPK1 and VQVG in RIPK3), assemble into β-sheet fibrils that are typical of amyloids [159, 161]. Importantly, the different amino acids in this peptide sequence (I in RIPK1 and V in RIPK3) are key to favor the formation of hetero-amyloids complexes (RIPK1-RIPK3) over homo-amyloids (RIPK1-RIPK1 / RIPK3-RIPK3) [161, 162] **(Figure 1.8B).**

A crucial step to initiate the assembly of these hetero-amyloid complex and trigger necroptosis is the activation of RIPK1. Accordingly, blocking RIPK1 activation with RIPK1 kinase inhibitors prevents necrosome formation and thus, necroptosis [84, 142].

It is thought that RIPK1, similarly to other kinases, behaves as a highly dynamic molecular switch that toggles between active and inactive conformational states [163]. In protein kinases, the switch between these states is determined by the assembly and disassembly of two structural elements which are known as the 'regulatory' and 'catalytic' spines (R- and C- spines, respectively) [164]. The spines consist of two stacks of four to six hydrophobic residues, which are aligned in every active kinase but 'broken' in inactive kinases [163]. Of note, binding of ATP allows the kinase to complete the assembly of the C-spine, whereas kinase-specific regulatory mechanisms function to assemble the R-spine [163]. In particular, phosphorylation in the activation loop frequently stabilises the R-spine.

When compared to other kinases, RIPK1 is a poor kinase as its only substrate is itself [84, 135, 165]. Autophosphorylation of RIPK1 occurs at S14/15, S20, S161, and S166 [84] and is promoted by dimerization of RIPK1 molecules via their DDs [166]. In particular, autophosphorylation of the activation loop at S166 serves as a marker for RIPK1 activation [84]. Nevertheless, mutation of S166 does not influence mutant RIPK1^{S166A} to promote cell death [84, 135, 167]. Similarly, mutating the remaining autophosphorylation sites did not influence cell death, with the exception of S161, for which contrasting results have been reported [84, 167]. Together, although it is clear that RIPK1 activation is important for TNF-induced activation of necroptosis, the precise molecular mechanism of RIPK1 activation remains unclear [83, 84].

Once active, RIPK1 can bind to RIPK3 via their respective RHIM domain. This then allows additional RIPK3 molecules to oligomerize via their RHIM domains to induce RIPK3 activation [168]. During this process, the kinase domains of RIPK3 also interact with one another, inducing the assembly of the R-spine and stimulating the activation of RIPK3 through autophosphorylation [163, 165, 169]. In particular, human RIPK3 is autophosphorylated on S227 (S232 and T231 of murine RIPK3) [168, 170, 171]. RIPK3 oligomers are not only triggered by active RIPK1. Other RHIM containing proteins, such as DAI (ZBP1) and TRIF, can also induce RIPK3 oligomerisation and activation, independently of RIPK1 (see Section 1.6).

Together, the current model dictates that RIPK1 activation (via autophosphorylation or additional regulatory mechanisms) results in conformational changes that lead to an 'open conformation' allowing the exposure of its RHIM domain for interaction with RIPK3. This allows the formation of hetero-amyloid complexes. These RHIM-RHIM-mediated interactions might act as a 'seed' to promote RIPK3 homo-oligomerization and activation via autophosphorylation. Once RIPK3 is activated it binds and activates MLKL, thereby triggering necroptosis. The importance of RHIM-RHIM interactions is also evidenced by the fact that certain pathogens encode RHIM antagonists or proteases that target RHIM-containing proteins, thereby blocking necrosome assembly and necroptosis [172-176]. Evasion of necroptosis can allow pathogen growth and dissemination.

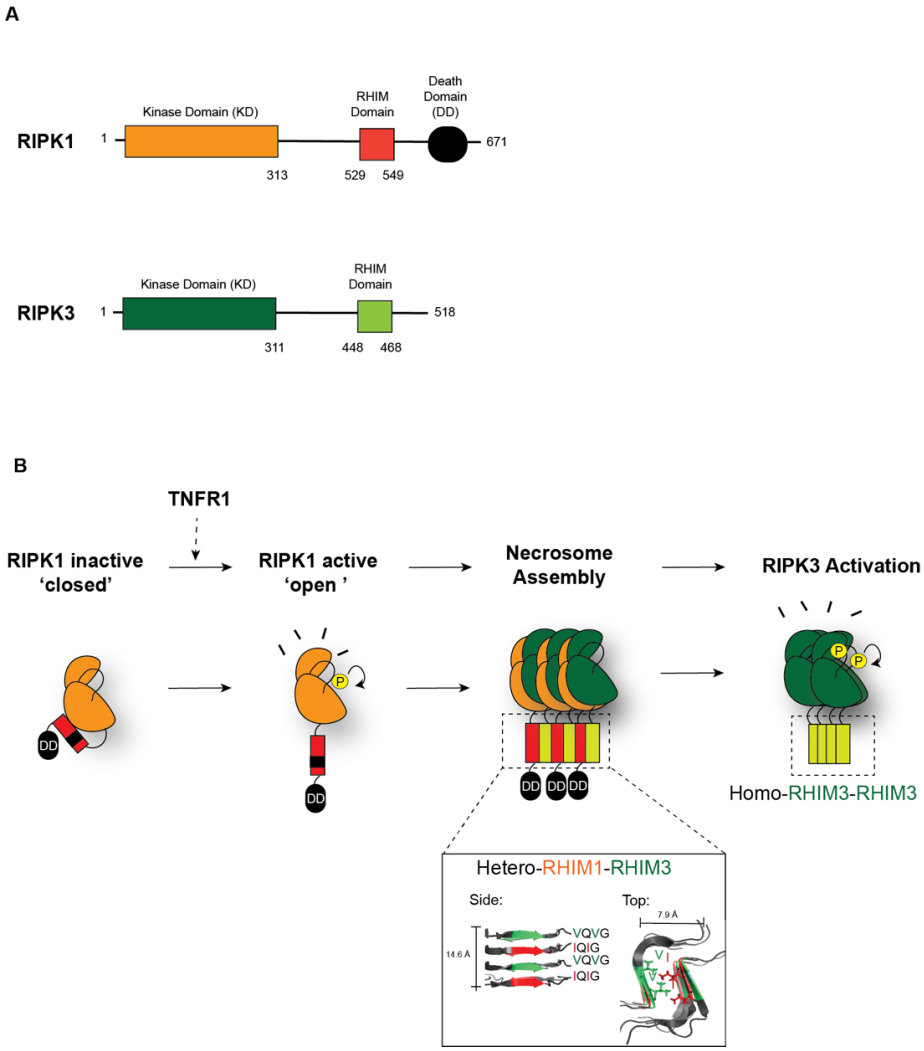

Figure 1.8. Necrosome assembly by RIPK1 and RIPK3

(A) The domain architecture of hRIPK1 and hRIPK3 is shown (top and bottom, respectively), comprising the KD, a RHIM domain and, in the case of RIPK1, a DD. **(B)** Assembly of the necrosome via RIPK1-RIPK3 interaction. TNFR1 stimulation induces the activation of RIPK1, which in the absence of caspase-8, recruits RIPK3 to form the necrosome. The interaction between RIPK1 and RIPK3 occurs via their respective RHIM domains forming a hetero-oligomer. Magnification: two views of the amyloid-like fibril are shown (top and side) with the RHIM domains for RIPK1 and RIPK3 colored in red and green, respectively. The two RHIM domains (from RIPK1 and RIPK3) stack in parallel on top of each other making a hetero-amyloid sheet (as seen in the side view). Two hetero-amyloid sheets arrange face-to-face with the side chains of V and I from the core tetrapeptide motifs located in the RHIM domains (VQVG (RIPK1) and IQIG (RIPK3)) forming a hydrophobic interface (as seen in the top view). The side chains of V and I are shown as sticks. (drawn from PDB 5V7Z [161]). The assembly of the necrosome facilitates RIPK3 activation via oligomerization-induced autophosphorylation.

1.5.2. MLKL

To date, MLKL is considered to be the last effector of the necroptotic pathway. Phosphorylation of MLKL by RIPK3 induces its activation and translocation to the plasma membrane to induce cell death [170, 177].

1.5.2.1. Structure of the pseudokinase MLKL

MLKL is a pseudokinase [163, 178]. Although it structurally resembles a conventional protein kinase, MLKL lacks two of the three conserved catalytic residues, which are crucial for phosphoryl transfer activity [178, 179]. Therefore, the C-terminal pseudokinase domain of MLKL solely functions as a regulatory domain for protein-protein interactions [165].

MLKL is made up of 3 domains. The N-terminal region (amino acids 1-170) of MLKL assembles into a four-helix bundle domain (4HB) and is followed by a brace domain. At the C-terminus MLKL carries a pseudokinase domain (PsKD, amino acids 171-464) [178] **(Figure 1.9A)**. Of these domains, the 4HB constitutes the effector domain, being indispensable for cell death execution [180]. Under base-line conditions (viable state), the 4HB is kept inactive via interaction with the pseudokinase domain [180, 181]. Such an interaction is stabilised by residues of the brace region and therefore, the brace domain serves to transmit the necroptotic signal, induced by RIPK3-mediated phosphorylation, from the pseudokinase domain to the 4HB domain [165, 182]. Mechanistically, following necroptotic stimuli, RIPK3 phosphorylates MLKL in the pseudokinase domain. This results in a conformational change of the PsKD, leading to the release of the 4HBD. This also exposes the brace that subsequently allows brace-mediated oligomerization of MLKL, a requirement for MLKL killing function [178, 180].

1.5.2.2. Mechanism of MLKL activation and cell death execution

RIPK3 is currently the sole kinase capable of activating MLKL. Structural data indicate that the murine MLKL (mMLKL) PsKD interacts with the KD of murine

RIPK3 (mRIPK3) in a 1:1 ratio [183]. In this complex, RIPK3 and MLKL molecules aligned in a parallel fashion, with the N- and C-lobes of RIPK3 packing closely against the N- and C-lobes of MLKL, respectively **(Figure 1.9B)** [183].

The murine RIPK3-MLKL interaction involves extensive van der Waals contacts and hydrogen bonds, which are key for complex formation. Noteworthy, the phosphate group of S232 (autophosphorylation site) in RIPK3 forms a hydrogen bond with the hydroxyl group of S404 on MLKL, strongly suggesting an important role for S232 phosphorylation in MLKL recruitment **(Figure 1.9B,** magnification bottom panel) [183]. Additionally, the phenyl ring of F373 in MLKL inserts into a hydrophobic pocket, formed by several residues of RIPK3 **(Figure 1.9B,** magnification top panel) [183]. In line with a role for these residues in stabilising the interaction, mutation of these residues (S404A or F373A in MLKL, S232A in RIPK3) interfered with complex formation [183]. The aforementioned interactions are conserved in the human setting, based on structural modeling of the hRIPK3 kinase domain [183]. For instance, F386 of hMLKL (corresponding to F373 of mMLKL) is surrounded by a highly conserved hydrophobic pocket present in hRIPK3. Additionally, the phosphorylated S227 of hRIPK3 forms a hydrogen bond with S417 of hMLKL [183].

Nonetheless, a number of species-specific interactions were also observed in the interface between the C- and N-lobes [183], These species-specific differences help to explain why hRIPK3 and mMLKL fail to form stable complexes [170, 171]. Detailed analysis of the necroptotic pathways in human and mouse have revealed fundamental differences between these species [165, 181]. While a transient interaction between RIPK3 and MLKL is sufficient to induce MLKL activation in mouse (‘kiss-and-run’ activation mechanism), the interaction between RIPK3 and MLKL is more stable in humans, as shown by biochemical approaches [165, 181].

RIPK3 phosphorylates MLKL in its activation loop at residues S345 in mouse and T357/S358 in human [170, 177]. Of note, these sites are proximal to the ‘pseudoactive site’ of MLKL, which is positioned in the cleft between the N- and

C-lobes of the pseudokinase domain. Importantly, substitutions in key residues within the pseudoactive site of mMLKL (K219M or Q343A) resulted in constitutive activation [178]. Thus, a potential model emerged whereby RIPK3 phosphorylation could induce rearrangements in the pseudoactive site resulting in a conformational change that releases the inhibition of the 4HBD **(Figure 1.9C)** [178]. While additional sites of phosphorylation by RIPK3 have been reported in mMLKL (S347 and T349) they do not seem to be critical for the killing activity [184]. Additional phosphorylation sites located outside of the activation loop of mMLKL have been reported and appear to fine-tune MLKL's killing activity, although the responsible kinases remain unknown [185]. Similarly, non-activation loop phosphorylation sites have also been identified via proteomic studies in hMLKL, but their role in MLKL activity is unknown [186, 187].

Upon phosphorylation MLKL forms higher order oligomers and translocates to the plasma membrane [170, 177]. While the precise stoichiometry of the oligomers is controversial, evidence suggest that MLKL forms trimers in mice [180, 182, 188] and tetramers in humans [181]. However, hexamers [189] and octamers [190] have also been reported. At the plasma membrane, MLKL can further polymerize to form higher-order polymers, which are required for necroptosis [191].Mechanistically, the brace helices connecting the 4HBD with the pseudokinase domain, play a crucial role for the assembly of higher order species by providing an interface for oligomerization [182, 192]. In particular, the second brace helix is important for MLKL oligomerization. Accordingly, point mutations of the brace domain interfere with the formation of MLKL homotrimers [182].

MLKL reportedly executes its killing activity at the plasma membrane although the precise mechanism remains unclear [188, 193]. A number of models have been described to explain plasma membrane disruption. Based on the observation that recombinant MLKL is able to permeabilize liposomes *in vitro*, it was suggested that MLKL could directly induce plasma membrane permeabilization. In particular, this was dependent on the presence of Phosphatidylinositol Phosphates (PIPs) in the liposome membrane [177, 194, 195]. Other model suggested that MLKL activates cation channels (such as Ca^{+2}

channels), leading to an influx of cations and resulting in the loss of plasma membrane integrity due to osmotic swelling [188]. However, whether influx of cations and osmotic swelling is a cause or consequence of necroptosis remains unclear. Further, it was suggested that MLKL induces 'nanopores' of ~4 nm diameter [196]. Supporting this pore-forming hypothesis, there are structural similarities between the 4HB of MLKL and the Helo-Like domain in fungi and plants. Helo-Like domain organize into membrane-embedded pores that permeabilize cells [197]. Intriguingly, different MLKL orthologues seem to exhibit different abilities to permeabilize membranes [198]. This may indicate that auxiliary factors might regulate MLKL-mediated cell death in a species-specific manner.

MLKL-mediated necroptosis can be regulated at different levels. While it is clear that activation of RIPK3 is the primary control point of necroptosis, MLKL mediated cell death can also be suppressed downstream of MLKL activation. It has been suggested that activation of the endosomal sorting complexes required for transport (ESCRT)-III can release necroptotic vesicles containing phosphorylated MLKL [199, 200]. Thus, vesicular shedding of active MLKL antagonize the killing potential of MLKL [199, 200].

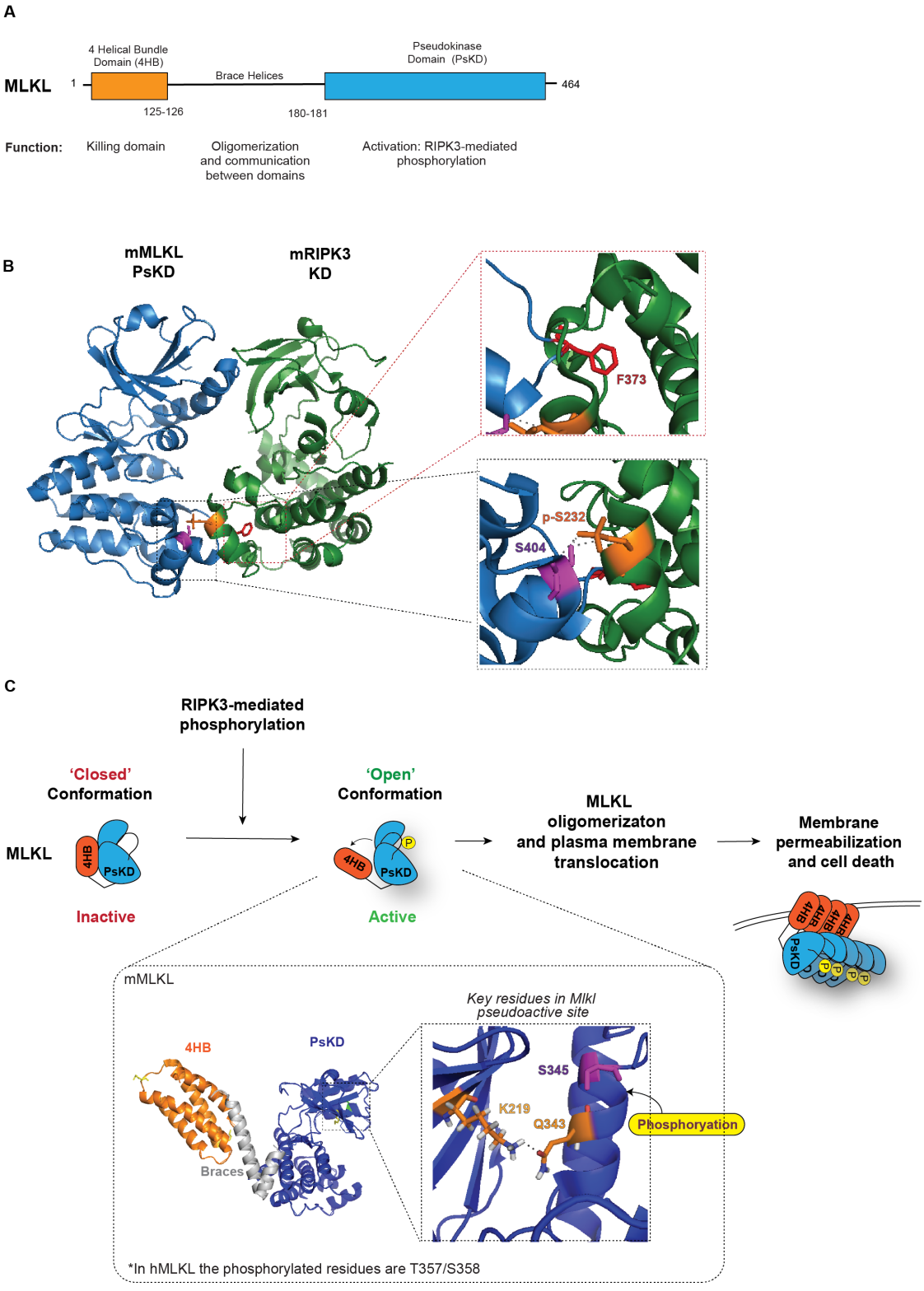

Figure 1.9. Structure of mMLKL and mechanism of activation.

(A) Schematic representation depicting the domains of mMLKL which comprises 4HBD (aa 1-125), the PsKD (aa 181-464) and two brace helices (126-181). **(B)** Structure of the mRIPK3-mMLKL complex and the interface between mRIPK3 and mMLKL (PBD: 4M69 [183]). Magnification showing the interaction between key residues. At the top panel, residue F373 of mMLKL (red) inserts into a hydrophobic pocket formed by side chains of several residues (grey) in mRIPK3. At the bottom panel, the phosphate group of phosphorylated S232 (orange) forms a hydrogen bond with the hydroxyl group of S404 (magenta) in mMLKL. **(C)** Following RIPK3-mediated phosphorylation MLKL undergoes a conformational change leading to the exposure of the 4HBD and becoming active. Magnification: Image of the crystal structure of full length mMLKL (PBD: 4BTF [178]). On the right side, magnification showing the key residues located in mMLKL pseudoactive site (K219, Q343 and S345). The side chains of K219 and Q343 residues are represented as sticks and coloured by atom type (carbon atoms in orange, nitrogen atoms in blue, oxygen atoms in red and hydrogen atoms in grey). Activated MLKL oligomerizes and translocates to the plasma membrane to induce cell death.

1.6. Other triggers of the necroptotic pathway

Much of our mechanistic knowledge of the necroptotic pathway comes from studies of TNFR1-signalling, and thus it is often considered as the canonical pathway. However, stimulation of other receptors and sensors, such as (1) death receptors, (2) TLRs and (3) ZBP1, can also trigger necroptosis [201].

1.6.1. Necroptosis mediated by death receptors

Beside TNFR1, other death receptor super family members can also drive RIPK1 activation and necroptosis. Under certain conditions, such as loss of cIAPs, FAS-R and TRAIL-R can drive the formation of a cytosolic death inducing complex that resembles Complex-II. This FAS-R and TRAIL-R-driven cytosolic complex consists of RIPK1, FADD and Caspase-8 [202-204]. Under conditions where caspase-8 activity is blocked, RIPK1 can recruit and activate RIPK3, driving MLKL-mediated necroptosis [205-207].

The signalling downstream of DR3 and DR6 is less well characterized. It is thought that these receptors can recruit TRADD and RIPK1 to engage a signaling complex similarly to TNFR1-Complex-I [99].

1.6.2. TLR-mediated engagement of necroptosis

Each member of the TLR family senses a particular PAMP, such as pathogen-associated peptidoglycan (TLR2), double-stranded (ds)-RNA (TLR3), LPS (TLR4), flagellin (TLR5), and unmethylated CpG DNA motif (TLR9) [69].

Stimulation of TLR3 and TLR4 can directly induce cell death - apoptosis or necroptosis- in a cell autonomous manner [208-210]. Mechanistically, stimulation of TLR3 and TLR4 leads to the assembly of a death-inducing complex that is similar to complex-II [202, 209, 211]. Importantly, in contrast to the TNF-setting, the formation of the killing platform downstream of these receptors, requires the additional recruitment of the cytosolic adaptor, Toll/IL-1 receptor (TIR) domain-containing adaptor protein inducing IFNβ (TRIF) [209].

TRIF interacts with the two TLRs via its TIR domain and mediates inflammatory and antiviral signaling through NF-κB activation and production of T1-IFN [69, 209, 212]. In addition, TRIF contains a RHIM domain that allows its interaction with RIPK1 and RIPK3 to mediate necroptosis under conditions where caspase-8 is blocked [208, 209]. Of note, the requirement of RIPK1 in TLR3/TLR4-induced cell death seems to be context dependent. In the absence of RIPK1, TRIF can directly engage and activate RIPK3. However, in the presence of inactive RIPK1, such as following genetic (*Ripk1*^{D138N}) or pharmacological inhibition of RIPK1, TLR3/4-induced necroptosis is blocked [209, 210, 213].This suggests that inactive RIPK1 acts as a dominant-negative, and while it is recruited to the TRIF signaling complex it blocks TRIF-mediated RIPK3 activation.

The remaining TLRs (TLR2, TLR5 and TLR9) can only trigger cell death via autocrine/paracrine-mediated engagement of other receptors, namely TNFR1, following activation of NF-κB and IFN-signalling. Accordingly, *Tnf*-/- BMDMs undergo necroptosis upon stimulation with TLR3/-4 agonist in presence of caspase inhibition but not upon treatment with agonists for TLR2,-5,or-9 [209].

1.6.3. ZBP1-mediated engagement of necroptosis

The intracellular innate immune sensor ZBP1 can also trigger necroptosis [201]. ZBP1 carries an N-terminal Z-DNA binding domain and two RHIM domains, which are crucial for its role in modulating cell death and inflammation [214-216]. Although, ZBP1 can act as DNA sensor more recent work indicate that ZBP1 can also detect viral and endogenous RNAs [217-219]. Upon its activation it can activate T1-IFN, NF-κB as well as cell death [220]. Interestingly, RIPK1 and RIPK3 are necessary for Type I IFN and NF-κB activation in response to immune stimulatory DNA [215, 221].

The ability of ZBP1 to intrinsically trigger cell death is best characterized in the context of viral infections, namely upon infection with Influenza A Virus (IAV), Murine Cytomegalovirus (MCMV) or Herpes Simplex Virus (HSV) [222]. Intriguingly, certain viruses encode proteins that contain RHIM-like domains.

These viral proteins compete with RIPK3 for ZBP1 binding, and hence block necroptosis [176, 223, 224]. Accordingly, viruses with mutations in the RHIM-like domain trigger ZBP1-mediated activation of RIPK3 and necroptosis [225, 226].

Studies on ZBP1 indicate that ZBP1 can also be activated in a non-infectious setting. For example, when RIPK1 has a defective RHIM, such as a mutation in the IQIG motif of the RHIM domain (*Ripk1*^{RHIMMut}), ZBP1 spontaneously activates RIPK3, resulting in perinatal lethality of those mutant mice [227, 228]. Therefore, the RHIM domain of RIPK1 keeps the activation of ZBP1 under check during embryonic development. Lack of this inhibition results in ZBP1-mediated interaction with RIPK3 and engagement of necroptosis, as demonstrated via immunoprecipitation experiments showing interaction between the RHIMs of ZBP1 and RIPK3 in *Ripk1* ^{RHIMMut} cells [227, 228]. Additionally, ZBP1 can induce keratinocyte necroptosis and trigger skin inflammation in mice, as demonstrated by genetic studies using epidermis specific *Ripk1*^{RHIMMut} knock-in mice [227]. Despite these data, it remains unclear what the endogenous trigger are that initiates ZBP1 activation in these settings, or the mechanisms by which RIPK1 inhibits ZBP1 activation.

1.6.4. Role of IFNs in necroptotic signaling

Several studies have involved IFNs in necroptotic cell death [201]. IFNs are primarily divided in two types: type I and type II (T1/2-IFN). T1-IFN include various subtypes of which IFNα/β are the predominant forms. T2-IFN involves a single cytokine IFNγ [229]. The stimulation of most PRRs induces the production of T1-IFN. Binding of IFNα/β to IFNR1 activates the JAK-STAT signalling pathway, which leads to the expression of Interferon Stimulated Genes (ISGs). ISGs comprise set of antiviral and inflammatory genes, and further induce IFNα/β expression resulting in an amplification feedback loop [229]. Necroptotic effectors MLKL and ZBP1 are important ISG genes [214, 230]. Hence, this autocrine/paracrine loop can regulate necroptosis. Macrophages deficient in IFNR1 are highly resistant to necroptosis triggered by LPS or poly(I:C) in combination with caspase inhibitors [231]. Mechanistically, *Ifnr1-/-* BMDMs present lower levels of MLKL expression following LPS treatment [232].

Therefore, IFNα/β produced in response to LPS, can induce the expression of MLKL, priming BMDMs to undergo necroptosis. IFNs are also regulated by a low-level constitutive feedback loop [233]. This constitutive expression of IFN is also critical for the early initiation of necroptosis in macrophages [233]. Lastly, strong activation of the cGAS-STING signaling pathway has been described to trigger necroptosis via synergistic IFN and TNF signalling [234].

The crosstalk between IFNs and necroptosis has also been studied genetically in the context of RIPK1 deficiency [235]. *Ripk1*-/- mice are perinatally lethal, dying 48 h after birth due aberrant apoptotic and necroptotic cell death in various tissues [236]. Thus, the lethality of these mice can be rescued to adulthood by co-deletion of *Ripk3* or *Mlkl* (preventing necroptosis) and *Fadd or Caspase-8* (preventing apoptosis) [236-238]. Intriguingly, co-deletion of *Tnfr1* results in only a slight delay in lethality, if at all, suggesting that the exacerbated cell death observed in the absence of RIPK1 is mediated by pathways other than TNFR1-signalling [236, 237]. Genetic studies suggest that IFN-signalling activates RIPK3-dependent cell death when RIPK1 is absent [235]. Accordingly, genetic deletion of T1/2 IFN-signalling in *Ripk1*-/- mice (*Ripk1-/-, Tnfr1-/-*, *Ifnar1-/-, Ifrgr1-/-*) delays RIPK3-dependent lethality to almost 3 months [235]. Likewise, co-deletion of *Zbp1* in a *Ripk1-/-*, *Casp8-/-* background (Casp-8 is deleted to neutralize TNF-dependent apoptosis), also delayed the lethality (up to 5 weeks) [235]. This data suggests that during mammalian parturition, IFNs can induce expression of ZBP1 via Jak-STAT signaling, and if RIPK1 is absent, ZBP1 associates with RIPK3 to drive MLKL-mediated necroptosis [235]. The precise mechanism why loss of RIPK1 results in IFN signalling, and how ZBP1 activates RIPK3 in this context remains unclear.

Lastly, combination of Type1/2 IFNs with certain cell cycle arrest inducing compounds (i.e. nocodazole, polo-like kinase 1 inhibitor) upon caspase inhibition triggers ZBP1-dependent necroptosis [239].

1.7. Ub-mediated control of key necroptotic players

The regulation of necroptosis has been mostly studied in the context of TNFR1-signalling. In this setting, the decision between survival and cell death is determined by complex PTMs, mostly affecting RIPK1. Since TNF signalling has been covered above (Section 1.4.3), this Section focusses on Ub-mediated regulation of components of the necroptotic pathway, such as RIPK1, RIPK3, ZBP1 and MLKL.

Under certain conditions, TNF-signalling can trigger the assembly of RIPK1-RIPK3 complexes. Both, RIPK1 and RIPK3 can be ubiquitylated in necrosome complexes. RIPK1 is modified by M1- and K63-linked Ub chains [240]. The conjugation of such chains appears to occur independently of cIAP1/2 (involved in ubiquitylation of RIPK1 in Complex-I) suggesting that other E3 ligases may be involved in regulating necroptosis [240]. Likewise, neither RIPK3 or MLKL were required [241]. The E3 ligase Pellino 1 (Peli1) is thought to mediate K63-linked ubiquitylation of RIPK1 in the necrosome, which appears to contribute to necrosome stability [242]. Since RIPK1 from Complex-I nucleates the necrosome, it remains unclear whether the Ub chains on RIPK1 in the necrosome might actually derive from RIPK1 ubiquitylation in Complex-I.

During necroptosis, RIPK3 is conjugated with K63- and K48-linked Ub chains [243-246]. The E3 ligase carboxyl terminus of Hsp70-interacting protein (CHIP) was reported to mediate ubiquitylation of both, RIPK1 and RIPK3 leading to their lysosomal degradation. Additionally, a more recent study implicates the E3 ligase Parkin in the modulation of necrosome assembly [244]. Mechanistically, Parkin mediates K33-linked polyUb chains on RIPK3, thereby preventing the formation of the necrosome [244].

Besides RIPK1 and RIPK3, ZBP1 is also ubiquitylated upon necroptosis engagement [247]. Infection of fibroblast with IAV triggers prominent ZBP1 ubiquitylation at K17 and K43, which are located in the Z-DNA-binding domain [247]. However, the functional consequence of this PTM is currently unclear.

MLKL also is subject to ubiquitylation under necroptotic conditions. Accordingly, treatment with LPS/SM/zVAD results in prominent MLKL ubiquitylation [248]. However, the role of MLKL ubiquitylation remains to be investigated.

1.8. Aims of the study

MLKL is the last effector of the necroptotic pathway, yet its regulation and mechanism for cell death execution remains unclear. Particularly, very little is known about Ub-mediated regulation of MLKL during necroptosis. To gain a better understanding of necroptosis regulation, I focused on the molecular mechanisms that control the cytotoxic potential of MLKL.

The aim of this study is to gain a better understanding of MLKL-mediated cell death. My work focusses on two aspects:

I. Investigate the role of the Ub system in regulating MLKL-mediated cell death
    1. Characterize the Ub modification of MLKL
    2. Identify Ub-acceptor K of MLKL
    3. Determine the functional consequences of MLKL ubiquitylation

II. Characterize novel mechanistic insights of MLKL-mediated cell death
    1. Evaluate the involvement of potential binding partners of MLKL based on preliminary data generated in the Meier Lab
    2. Identify novel binding partners of MLKL
    3. Investigate the localization of MLKL at the plasma membrane

2. Materials and Methods

2.1. Reagents, Kits, Chemicals and Enzymes

Reagents, Chemicals or Enzymes	Supplier /Code
4′,6-diamidino-2-phenylindole (DAPI)	Thermo Fisher Scientific/ D3571
Acetic Acid	VWR /20104.312P
Acetonitrile CHROMASOLV LC-MS (ACN)	Fisher Scientific / 34967
Acetonitrile, 99.9%, Extra Dry, AcroSeal, ACROS Organics (For TMT labelling)	Fisher Scientific / 12317103
Agarose (molecular biology grade)	ThermoFisher Scientific / 17852
Amersham ECL prime western blotting detection reagent	GE Healthcare / RPN2106
Ammonium bicarbonate, BioUltra, ≥99.5%	Sigma-Aldrich / 09830
Ampicillin	Sigma-Aldrich / A9518
Anti-FLAG M2 Affinity Gel	Sigma-Aldrich / A2220
BCA Protein Assay	ThermoFisher Scientific / 500-0114, 500-0113, 500-0115
Blotting paper (Grade 17 Cellulose paper)	GE Healthcare / 3017-1915
Bromophenol Blue	Sigma-Aldrich / B61-31
Chloroacetamide (ChlAA)	Sigma-Aldrich / C0267-100G
Chloroform	Sigma-Aldrich / 22711-290
Clarity Western ECL chemiluminescence detection reagents	Bio-Rad / 1705061
Complete mini EDTA free Protease Inhibitor cocktail tablets	Roche / 11836170001
Cryogenic Tubes	Fisher Scientific / 374081
CutSmart Buffer	New England Biolabs / B7204S
DharmaFECT 4 transfection reagent	GE Healthcare / T-2004-03

Digitonin 5%	Thermo Fisher Scientific / BN2006
Dimethyl sulfoxide (DMSO)	Sigma-Aldrich / D2650
DNA ladder 1 Kb	New England Biolabs / N32325
DNA loading dye, purple (6X)	New England Biolabs / N7025
dNTPs solution	ThermoFisher Scientific / R0193
Doxycycline	Clontech / NC0424034
Dual Color molecular weight marker	Bio-Rad / 1610394
Dulbecco's Modified Eagle Medium (DMEM)	ThermoFisher Scientific / 41966-029
Duolink In situ Detection Reagents Green	Sigma-Aldrich / DUO92014
Duran AR Glass Disposable Culture Tubes	Fisher Scientific / 231751459
Fetal Bovine Serum (FBS) heat inactivated	ThermoFisher Scientific / 10500064
Gel Red nuceic acid stain	Biotium / 41003
Glutathione Agarose beads	GE Healthcare / 17075601
Glycerol	Sigma-Aldrich / G5516
Guanidine Hydrochloride	Sigma-Aldrich / G3272
Hoechst 33342 solution (20 mM)	ThermoFisher Scientific / H1399
Hydroxylamine 50%	Thermo Fisher Scientific / 90115
K63-linkage Ubiquitin Interacting Motif (K63-UIM) and K63-Mutant UIM Ctrol	Made in house
Lysyl Endopeptidase Mass Spectrometry Grade (Lys-C)	Alpha Labs / 125-05061
Met1-linkage Specific Ub-Binder (M1-SUB) and GST Ctrol.	Made in house (Rahighi et al., 2009)
Methanol, UHPLC, for mass spectrometry	Sigma-Aldrich / 900688-1L
MG132	Sigma-Aldrich / C2211

Milk powder	Marvel
Minisart Syringe Filter 45 μm	Sartorius / 16555
N-ethylmaleimide	Sigma-Aldrich / E3876
NativePAGE 4-16% Bis-Tris Protein Gels, 1.0 mm, 15-well	ThermoFisher Scientific / BN1004BOX
NativePAGE Cathode Buffer Additive (20X)	ThermoFisher Scientific / BN2002
NativePAGE Running Buffer (20X)	ThermoFisher Scientific / BN2001
NativePAGE Sample Buffer (4X)	ThermoFisher Scientific / BN-2003
NativePAGETM 5% G250 Sample Additive	ThermoFisher Scientific / BN-2004
Necrosulfonamide (NSA)	Tocris / 5025
Neon Transfection System 10 µL Kit	ThermoFisher Scientific / MPK1025
NuPAGE MOPS SDS Running buffer (20x)	ThermoFisher Scientific / NP000102
NuPAGE Novex 4-12% Bis-Tris 1.00 mm	ThermoFisher Scientific / WG1402/ WG1403
One Shot TOP10 Chemically Competent E. coli	ThermoFisher Scientific / C404010
Opti-MEM Reduced Serum Medium	ThermoFisher Scientific / 31985062
Paraformaldehyde solution 4% in PBS	Insight biot / sc-281692
PfuUltra High Fidelity DNA polymerase	Stratagene / 600670
Phosphatase Alkaline from bovine intestinal mucosa	Sigma-Aldrich / P0114
PhosStop EasyPack (Phosphatase inhibitors)	Roche / 4906837001
Pierce C18 Tips, 100 µL bed	Thermo Fisher Scientific / 87784
Pierce Protein A/G Plus Agarose	ThermoFisher Scientific / 20423
Pierce Streptavidin Agarose	ThermoFisher Scientific /

	20349
Polybrene Transfection Reagent	Millipore/ TR-1003-G
PR-619 (DUB inhibitor)	LifeSensors / SI9619
ProLong Gold Antifade Mountant	Thermo Fisher Scientific /P36930
Propidium Iodide	Sigma-Aldrich/ p4864
PTMScan Ubiquitin Remnant Motif (K-ε-GG)	Cell signalling / 5562
Puromycin	Invivogen / ant-pr-1
PVDF membrane (Immobilon P)	GE Healthcare / IPVH00010
Q5 Hot Start High Fidelity DNA polymerase	New England Biolabs / M0493S
Qiafilter Plasmid midi/mini kit	Qiagen / 12945
QIAquick Gel extraction kit	Qiagen / 28706
QuantiTech Reverse Transcription Kit	Qiagen / 205314
QuantiTect Reverse transcription kit	Qiagen / 205313
Recombinant M-CSF	Peprotech / 315-02
Restriction enzymes and corresponding buffers	New England Biolabs
RIPK1 inhibitor	GlaxoSmithKline / GSK'963
RIPK3 inhibitor	GlaxoSmithKline / GSK'843
RNeasy Mini kit	Qiagen/ 74106
Sep-Pak Vac tC18 cartridges	Waters / WAT036790
Sequencing Grade Modified Trypsin	Promega / V5113
Sequencing grade modified trypsin (Form LC-MS/MS)	Promega / V5113
SMAC mimetic (SM164)	Gift from Wang Shaomeng, North Campus Research Complex, University of Michigan
Sodium Azide	Sigma / S2002
Sodium dodecyl sulfate (SDS)	Sigma-Aldrich / 436143
Sterilin uncoated 140 cm dishes	Thermo Fisher Scientific / 11339283

Sucrose	VWR Chemicals / 24480.260
SuperSignal West Femto Maximum Sensitivity Substrate	ThermoFisher Scientific / 34095
T4 DNA ligase and buffer	New England Biolabs / M02025
Tandem Ubiquitin Binding Entities (TUBEs)	Made in house
TaqMan Gene Expression Master Mix	ThermoFisher Scientific / 4369016
Thiourea	Sigma-Aldrich / T8656
Tissue culture consumables	All tissue culture flasks were purchased from Falcon. Plates and dishes were purchased from NUNC.
TMT10plex Isobaric Label Reagent Set, 1 x 0.8 mg	Thermo Fisher Scientific / 90111
TNFα (Recombinant human and mouse)	Enzo / ALX-522-008-C050
TRAIL	Gift from Henning Walczak, UCL
Triethylammonium bicarbonate (TEAB), 1M	Thermo Fisher Scientific / 90114
Trifluoroacetic acid (TFA)	Sigma-Aldrich / T6508
Triton X-100	Sigma-Aldrich / T8787
Triton X-114	Sigma-Aldrich / X114-100ml
Trypsin-EDTA solution (For MDF isolation)	Sigma-Aldrich / T4049
Tween-20	ThermoFisher Scientific / P1379
Urea	Sigma-Aldrich/ U1250-1KG
USP21	Gift from Prof. David Komander
Viromer YELLOW transfection reagent	Cambridge Bio / VY-01LB-01
Water, HPLC for Gradient Analysis	Fisher-Chemicals / W/0106/17
X-ray Films	Scientific Laboratories (SLS)/ MOL7016

zVAD-fmk	Enzo / A1902
β-mercaptoethanol	Sigma-Aldrich / M6250

Table 2.1. List of reagents, kits, chemicals and enzymes

2.2. General Solutions

Solution	Recipe
10 X DUB digestion Buffer	500 mM Tris (pH 7.5), 500 mM NaCl, 50 mM DTT.
10 X IAP Buffer for di-Gly MS	500 mM MOPS, pH 7.4, 100 mM Na_2HPO_4, 500 mM NaCl.
6x SDS Protein Loading Buffer	3 ml 20% SDS, 4 ml 100% glycerol, 3 ml β-ME, 1g bromophenol blue
6x SDS Protein Loading Buffer for Non-Reducing Conditions	3 ml 20% SDS, 4 ml 100% glycerol, 3 ml H_2O, 1g bromophenol blue
Milk Solution (5%)	5% milk in TBS-T
Bovine Serum Albumin (BSA) 5% Blocking Solution	5% BSA in TBS-T
Complete DISC Lysis Buffer	DISC lysis buffer supplemented with protease inhibitor cocktail (1 tablet per 20 ml) and phosphatase inhibitor (1.5 tablets per 20 ml).
Denaturation buffer for di-Gly MS	6 M Urea, 2 M Thiourea, 50 mM Tris, pH 8.
DISC Lysis Buffer	1 M Tris pH 7.8, 5 M NaCl, 0.5 M EDTA, 40% Glycerol and 1% Triton X-100
Formaldehyde (cell fixing)	10% formaldehyde in PBS
Fractionation lysis buffer by sucrose density gradient centrifugation	20 mM HEPES, pH 7.5, 100 mM KCl, 2.5 mM $MgCl_2$, 100 mM sucrose, 0.025% digitonin, 2 µM N-ethylmaleimide.
Fractionation lysis buffer with Triton X-114	20 mM HEPES, pH 7.4, 150 mM NaCl, 2% Triton X-114
Freezing solution for mammalian cells	10% DMSO in FBS
HEPES pH 7.4	2.3g of HEPES in 100 ml H_2O. pH adjusted with

	5M NaOH
Luria Broth Medium (LB)	10 g of Bacto tryptone, 5g NaCl and 5g of yeast extract in 1 L dH_2O.
Milk secondary antibody solution	5% powder milk in TBS-T
MOPS Running buffer 20x	50 mM MOPS, 50 mM Tris Base, 0.1% SDS, 1 mM EDTA, pH 7.7
PBS-Tx	PBS 1% Triton X-100
Penicillin/Streptomycin (Pen/Strep) solution	12 g/l Benzylpenicillin and 20 g/l Streptomycin sulfate were dissolved in dH_2O for preparation of 200x concentrated solution. After filtration sterilisation the solution was stored at -20°C
Phosphate-buffered Saline (PBS)	137 mM NaCl, 2 mM KCl, 8 mM Na_2HPO_4, 1.5 mM KH_2PO_4 in dH_2O. pH adjusted to 7.4 with 5 M HCl
Reduction buffer for di-Gly MS	1 M DTT, 50 mM Ambic
Sodium Dodecyl Sulfate (SDS)	20% stocks (w/v) were prepared in dH_20
TAE Buffer (50X)	242g Tris Base, 57.1 mL glacial acetic acid, 18.61g EDTA in H_2O up to 1L
Tris Buffered Saline (TBS) 10X	10M Tris-HCl pH 7.5, 5M NaCl, in H_2O, used at 1x concentration.
TBS-T	TBS plus 0.1% Tween 20
Total cell lysis buffer for di-Gly MS	8 M Urea, 50 mM NaCl, 50 mM Tris, pH 8, 5.5 mM ChlAA in 50 mM Ambic
Transfer Buffer	400ml dH_2O, 100ml methanol, 1.5g Trizma base. Stored at RT.
Transformation Storage Buffer (TSB)	5% DMSO, 10% polyethylene glycol (PEG 4000), 10 mM $MgCl_2$ and 10 mM $MgSO_4$ dissolved in LB. Filtered using a 0.2 µM filter
Tris-HCl	1 M Stock. 121.1 g Trizma base was dissolved in 800 ml dH_20, pH adjusted using concentrated HCl and final volume made up to 1 litre.
Trypsin 0.05% in versene	8g/l NaCl, 0.2g/l KCl, 1.15 g/l Na_2HPO_4, 1g/l D-Glucose, 0.2g/l KH_2PO_4, 0.2g/l EDTA, 3g/l Tris, 1.5ml/l Phenol red 1%, 0.5g/l Trypsin Difco 1:250, 0.1g/l Streptomycin sulphate, 0.06g/l

	benzylpenicillin, dissolved in dH_2O and sterile filtered. Stored at −20°C.
Ubiquitin Lysis buffer	Complete DISC buffer supplemented with 10 µM PR-619, 1 mM DTT and GST-TUBE (50 µg/ml).
Wash buffer for endogenous MLKL IP	50 mM Tris (pH 7.5), 150 mM NaCl, 0.1% Triton X-100, and 5% glycerol
Wash buffer for ubiquitylation assays	PBS-Tx supplemented with 10 µM PR-619

Table 2.2. List of general solutions

2.3. Antibodies

2.3.1. Primary Antibodies

Primary Antibodies	Species of Origin	Working Dilution	Supplier/Code
Anti-Actin	Goat	1:2000	Santa Cruz Biotech / sc-1615
Anti-Caveolin-1	Rabbit	1:1000	Santa Cruz Biotech / sc-894
Anti-FLAG tag	Rabbit	1:1000	Cell Signalling/ 14793
Anti-Hsp90	Mouse	1:1000	Santa Cruz Biotech / sc-7947
Anti-K48-specific Ubiquitin	Rabbit	1:1000	Millipore / 05-1307
Anti-K63-specific Ubiquitin	Mouse	1:1000	Millipore / 05-1313
Anti-M1-specific Ubiquitin	human IgG1	1:1000	Genentech / 1F11
Anti-MLKL	Rat	1:1000	Millipore / MABC604
Anti-Phospho-MLKL S345	Rabbit	1:1000	Abcam / ab196436
Anti-Phospho-MLKL S357/T358	Rabbit	1:1000 1:20 (IF)	Abcam / ab187091
Anti-RIPK1	Mouse	1:1000	BD / 610459
Anti-RIPK3	Rabbit	1:1000	Imgenex / IMG-5846A

Anti-Ubiquitin	Rabbit	1:1000	Dako / Z0458

Table 2.3. List of primary antibodies

2.3.2. Secondary Antibodies

Secondary Antibodies	Working Dilution	Supplier /Code
Anti-goat IgG (H+L)-HRP	1:10000	Jackson Immuno Research / 305-035-003
Anti-mouse IgG (H+L)-HRP	1:10000	Jackson Immuno Research / 115-035-003
Anti-rabbit IgG (H+L)-HRP	1:10000	Jackson Immuno Research/ 111-035-003
Anti-rat IgG (H+L)-HRP	1:10000	Jackson Immuno Research 112-035-003

Table 2.4. List of secondary antibodies

2.3.3. Fluorescence conjugated Antibodies

Antibodies	Working Dilution	Supplier/Code
Alexa Fluor anti-rabbit IgG 488	1:500	ThermoFisher Scientific / A11008
Phalloidin, Alexa Fluor 633	1:500	ThermoFisher Scientific / A22284
Wheat Germ Agglutinin, Alexa Fluor 633	1:200	ThermoFisher Scientific / W21404

Table 2.5. List of fluorescence conjugated antibodies

2.4. Plasmids

Plasmid	Origin
TUBE_Ubqx4_pGEX6P1	Prof. M.Gyrd-Hansen
pET104-DEST-UIM3x-(RAP80) wildtype	Prof. Neils Mailand
pET104-DEST-UIM3x-(RAP80) mutant	Prof. Neils Mailand
GST-M1 SUB (NEMO UBAN)_pGEX6P1	Prof. M. Gyrd-Hansen
pBluescript KS	Stratagene
pTRIPZ (Lentiviral)	Open Biosystems
psPAX2 (Lentiviral packaging)	Addgene (Plasmid number 48138)
pMD2.G (Lentiviral packaging)	Addgene (Plasmid number 12259)
pBluescript-mMLKL^{WT}	Generated by Dr. T. Tenev
pBABE SV40 (Large T Antigen ∆89-97-missing Bub1)	Gift from Prof. Parmjit Jat
pF TRE3G rtTAAd-mMLKL^{WT}	Gift from Prof. J. Silke
pF TRE3G rtTAAd-mMLKL $^{(\Delta 4HBD, aa\ 124-464)}$	Gift from Prof. J. Silke
pF TRE3G rtTAAd-mMLKL^{S345D}	Gift from Prof. J. Silke
pF TRE3G rtTAAd- mMLKL (N-ter FLAG)	Gift from Prof. J. Silke
pTRIPZ-mMLKL^{WT}	Generated by L. Ramos Garcia
pTRIPZ-mMLKL^{S345A}	Generated by L. Ramos Garcia
pTRIPZ-mMLKL^{S345D}	Generated by L. Ramos Garcia
pTRIPZ-mMLKL^{K219M}	Generated by L. Ramos Garcia
pTRIPZ-mMLKL^{K219R}	Generated by L. Ramos Garcia
pTRIPZ-mMLKL^{K172R}	Generated by L. Ramos Garcia
pTRIPZ-mMLKL^{K51R}	Generated by L. Ramos Garcia
pTRIPZ-mMLKL^{K77R}	Generated by L. Ramos Garcia
pTRIPZ-mMLKL$^{K51R, K77R}$	Generated by L. Ramos Garcia
pTRIPZ-mMLKL$^{K51R, K77R, K219R}$	Generated by L. Ramos Garcia
pTRIPZ-mMLKL$^{K51R, K77R, K219R, K172R}$	Generated by L. Ramos Garcia

pTRIPZ-mMLKL$^{S345A, T349A (C\text{-}ter\ 3XFLAG)}$	Generated by Dr. Sidonie Wicky-John
pTRIPZ-mMLKL$^{WT (C\text{-}ter\ 3XFLAG)}$	Generated by Dr. Sidonie Wicky-John
pTRIPZ-mMLKL$^{WT (N\text{-}ter\ 3XFLAG)}$	Generated by Dr. Sidonie Wicky-John
pTRIPZ- mMLKL$^{K219R, S345D}$	Generated by L. Ramos Garcia
pTRIPZ-mMLKL^{T217F}	Generated by Dr. S. Wicky-John
pTRIPZ-mMLKL^{T217W}	Generated by Dr. S. Wicky-John
pLC-GFP	Gift form Dr. B.C. Bornhauser
pLC-GFP-mRIPK3_sgRNA5	Generated by Dr. A. Annibaldi
pLC-GFP-mRIPK3_sgRNA8	Generated by Dr. A. Annibaldi
pLC-mCherry-mRIPK1_sgRNA	Generated by Dr. A. Annibaldi
Cas9-GFP	Addgene (Plasmid number 41815)
sgRNA expression plasmid	Synthetically generated by Dr. T. Tenev
hMLKL sgRNA 1 expressing plasmid	Generated by L. Ramos Garcia
hMLKL sgRNA 2 expressing plasmid	Generated by L. Ramos Garcia
mMLKL sgRNA 1 expressing plasmid	Generated by L. Ramos Garcia
mMLKL sgRNA 2 expressing plasmid	Generated by L. Ramos Garcia
hTrim25 sgRNA 1 expressing plasmid	Generated by L. Ramos Garcia
hTrim25 sgRNA 2 expressing plasmid	Generated by L. Ramos Garcia

Table 2.6. List of plasmids

2.5. Oligos

2.5.1. Oligos for Short Interfering RNA (siRNA)

hTrim25 was targeted using the following siRNA oligos or a pool of the following non-overlapping siRNAs. Non-targeting siRNA was used as a control siRNA. All siRNAs utilised are from Dharmacon.

Target gene (siRNA oligo)	Target Sequence (5' – 3')	Cat. no

hTrim25 siRNA 5	CGGAACAGTTAGTGGATTT	J-006585-05
hTrim25 siRNA 6	CAACAAGAATACACGGAAA	J-006585-06
hTrim25 siRNA 7	GCGGATGACTGCAAACAGA	J-006585-07
hTrim25 siRNA 8	GGGATGAGTTCGAGTTTCT	J-006585-08
Non-targeting siRNA	NA	D-001810-0X

Table 2.7. List of oligos for siRNA

2.5.2. Oligos for site-directed mutagenesis

The following forward primers (F) were used with their correspondent reverse compliment (R) for site directed mutagenesis.

Mutagenesis	Sequence of primers (5' – 3')
mMLKL^{S345A}	F: TTAAGCAAAACACAGAATGCCATCAGCCGGACAGCAAAG R: CTTTGCTGTCCGGCTGATGGCATTCTGTGTTTTGCTTAA
mMLKL^{S345D}	F: TTAAGCAAAACACAGAATGACATCAGCCGGACAGCAAAG
mMLKL^{K219R}	F: AGATCTCCAGTTACCATCAGAGTATTCAACAACCCCCAG R: CTTTGCTGTCCGGCTGATGTCATTCTGTGTTTTGCTTAA
mMLKL^{K219M}	F: AGATCTCCAGTTACCATCATGGTATTCAACAACCCCCAG R: CTGGGGGTTGTTGAATACCATGATGGTAACTGGAGATCT
mMLKL^{Q343A}	F: TTTGAGTTAAGCAAAACAGCGAATTCCATCAGCCGGACA R: TGTCCGGCTGATGGAATTCGCTGTTTTGCTTAACTCAAA
mMLKL^{K172R}	F: CTGAAGCAATGCTCACTAAGACCCACACAGGAGATCCCA R: TGGGATCTCCTGTGTGGGTCTTAGTGAGCATTGCTTCAG
mMLKL^{K51R}	F: CTCCAGGCCCAAGGAAAGAGGAACCTGCCCGATGACATTACT R: AGTAATGTCATCGGGCAGGTTCCTCTTTCCTTGGGCCTGGAG
mMLKL^{K77R}	F: GCTAACCAGCAGATAGAAAGATTCAGCAAG R: CTTGCTGAATCTTTCTATCTGCTGGTTAGC
mMLKL$^{S345A, T349A}$	F: TTAAGCAAAACACAGAATGCCATCAGCCGG R: CCGGCTGATGGCATTCTGTGTTTTGCTTAA
mMLKL^{T217F}	F: TATCACAGATCTCCAGTTTTCATCAAAGTATTCAACAACCCC

	R: GGGGTTGTTGAATACTTTGATGAAAACTGGAGATCTGTGATA
mMLKL^{T217W}	F: TATCACAGATCTCCAGTTTGGATCAAAGTATTCAACAACCCC R: GGGGTTGTTGAATACTTTGATCCAAACTGGAGATCTGTGATA

Table 2.8. List of oligos for site-directed mutagenesis

2.5.3 Oligos for CRISPR-Cas9 system

The single guide RNAs (sgRNAs) used for the CRISPR-Cas9 system were designed using *crispr.mit.edu* portal. The forward and reverse primers containing the target sequence were designed so that they pair with each other and result in two overhangs (5'-CACCG in forward oligo, 5'-AAAC…C in the reverse). These oligos are shown in the table below, where the protospacer adjacent motif (PAM) sequence, required for Cas9 to function, is underlined. sgRNA for *hMlkl*, *hTrim25* and *mMlkl* were cloned into an sgRNA expression plasmid and transfected together with Cas9-GFP plasmid, whereas sgRNA for *mRipk1* and *mRipk3* were cloned into a plasmid expressing Cas9 (pLC-GFP).

CRISPR sgRNA guide	Target sequence (5' – 3')
hMlkl (sgRNA 1)	F: CACCGAAGAAACAGTGCCGGCGCCTGGG R: AAACCCCAGGCGCCGGCACTGTTTCTTC
hMlkl (sgRNA 2)	F: CACCGGGAGCTCTCGCTGTTACTTCAGG R: AAACCCTGAAGTAACAGCGAGAGCTCCC
hTrim25 (sgRNA 1)	F: CACCGGAGCCGGTCACCACTCCGTGCGG R: AAACCCGCACGGAGTGGTGACCGGCTCC
hTrim25 (sgRNA 2)	F: CACCGGGGAGCCACCCGCCGACGTCTGG R: AAACCCAGACGTCGGCGGGTGGCTCCCC
mMlkl (sgRNA 1)	F: CACCGCGTCTAGGAAACCGTGTGCACGG R: AAACCCGTGCACACGGTTTCCTAGACGC
mRipk1 (sgRNA1)	F: CACCGAGAAGAAGGGAACTATTCGC R: AAACGCGAATAGTTCCCTTCTTCTC
*mRipk3 (*sgRNA2)	F: CACCGAACCCGAGTGCCCTCGGCCC R: AAACGGGCCGAGGGCACTCGGGTTC

Table 2.9. List of oligos for CRISPR-Cas9 System

2.5.4. Oligos for *Mlkl* amplification and sequencing

***mMlkl* primers**	**Sequence (5' – 3')**
Amplification	F: GCTCACTAAAACCCACACAG R: CCAACACTTTCGGCCTGGGG
Sequencing	F: GCTCACTAAAACCCACACAG

Table 2.10. List of oligos for *Mlkl* amplification

2.5.5. Real Time Quantitative PCR TaqMan Probes

TaqMan Probe	**Cat. no**	**Type**
Trim25	Mm01304226_m	FAM-MGB
β-Actin	Mm00607939_s1	VIC-MGB

Table 2.11. TaqMan Probes

2.6. Cell lines

2.6.1. Parental cell line

Cell line	**Description**	**Origin**
HT-29	Human colorectal adenocarcinoma cell line	ATCC
L929	Mouse fibroblast cell line	ATCC
HEK293T	Human embryonic kidney cells with large T antigen	ATCC
Platinum E	Cells generated based on 293T cell line for retroviral packaging	Cell Biolabs

HaCaT	Transformed Human Keratinocyte cell line	ATCC
MDF	Immortalised Mouse Dermal Fibroblast derived from WT C57BL/6J mouse	Gift from Prof. J. Silke

Table 2.12. Parental cell lines

2.6.2. Genetically modified cell lines

Cell line	Description	Origin
MDF *Mlkl*$^{-/-}$	Immortalized MDF derived from *Mlkl*$^{-/-}$ mice.	Gift from Prof. J. Silke
MDF *Mlkl* $^{K219R/K219R}$ and *Mlkl* $^{WT/WT}$	MDFs from *Mlkl*$^{K219R/K219R}$ and littermate *Mlkl*$^{WT/WT}$ mice immortalized with SV-40 Large T antigen.	L. Ramos Garcia
Primary BMDMs *Mlkl* $^{K219R/K219R}$ and *Mlkl* $^{WT/WT}$	Primary BMDMs isolated from *Mlkl*$^{WT/WT}$ and *Mlkl*$^{K219R/K219R}$ littermate mice.	L. Ramos Garcia
Primary BMDMs *Trim25*$^{WT/WT}$ and *Trim25*$^{-/-}$	Primary BMDMs isolated from *Trim25*$^{WT/WT}$ *and* *Trim25*$^{-/-}$ littermate mice.	L. Ramos Garcia
MDF *Mlkl* ^{K219R}	MDF *Mlkl*$^{-/-}$ reconstituted with *Mlkl* ^{K219R}	L. Ramos Garcia
MDF *Mlkl*^{WT}	MDF *Mlkl*$^{-/-}$ reconstituted with *Mlkl*^{WT}	L. Ramos Garcia
MDF *Mlkl* $^{N-FLAG}$	MDF *Mlkl*$^{-/-}$ reconstituted with *Mlkl* $^{N-FLAG}$	L. Ramos Garcia
MDF *Mlkl* ^{S345A}	MDF *Mlkl*$^{-/-}$ reconstituted with *Mlkl* ^{S345A}	L. Ramos Garcia
MDF *Mlkl* ^{S345D}	MDF *Mlkl*$^{-/-}$ reconstituted with *Mlkl* ^{S345D}	L. Ramos Garcia
MDF *Mlkl* ^{K219M}	MDF *Mlkl*$^{-/-}$ reconstituted	L. Ramos Garcia

	with *Mlkl* ^{K219M}	
MDF *Mlkl* ^{K172R}	MDF *Mlkl*$^{-/-}$ reconstituted with *Mlkl* ^{K172R}	L. Ramos Garcia
MDF *Mlkl* ^{K51R}	MDF *Mlkl*$^{-/-}$ reconstituted with *Mlkl* ^{K51R}	L. Ramos Garcia
MDF *Mlkl* ^{K77R}	MDF *Mlkl*$^{-/-}$ reconstituted with *Mlkl* ^{K77R}	L. Ramos Garcia
MDF *Mlkl* $^{K51R, K77R}$	MDF *Mlkl*$^{-/-}$ reconstituted with *Mlkl* $^{K51R, K77R}$	L. Ramos Garcia
MDF *Mlkl* $^{K51R, K77R, K219R}$	MDF *Mlkl*$^{-/-}$ reconstituted with *Mlkl* $^{K51R, K77R, K219R}$	L. Ramos Garcia
MDF *Mlkl* $^{K51R, K77R, K219R, K172R}$	MDF *Mlkl*$^{-/-}$ reconstituted with *Mlkl* $^{K51R, K77R, K219R, K172R}$	L. Ramos Garcia
MDF *Mlkl* $^{S345A, T349A (C-ter 3XFLAG)}$	MDF *Mlkl*$^{-/-}$ or WT MDFs reconstituted with *Mlkl* $^{S345A, T349A (C-ter 3XFLAG)}$	L. Ramos Garcia
MDF *Mlkl* $^{WT (C-ter 3XFLAG)}$	MDF *Mlkl*$^{-/-}$ or WT MDFs reconstituted with *Mlkl* $^{WT (C-ter 3XFLAG)}$	L. Ramos Garcia
MDF *Mlkl* $^{K219R, S345D}$	MDF *Mlkl*$^{-/-}$ reconstituted with MLKL$^{K219R, S345D}$	L. Ramos Garcia
MDF *Mlkl* ^{T217F}	MDF *Mlkl*$^{-/-}$ reconstituted with MLKL^{T217F}	L. Ramos Garcia
MDF *Mlkl* ^{T217W}	MDF *Mlkl*$^{-/-}$ reconstituted with MLKL^{T217W}	L. Ramos Garcia
L929 *Mlkl*$^{-/-}$	CRISPR-mediated deletion of *mMlkl*	L. Ramos Garcia
MDF *Ripk1*$^{-/-}$	CRISPR-mediated deletion of *mRipk1*	L. Ramos Garcia
MDF *Ripk3*$^{-/-}$	CRISPR-mediated deletion of *mRipk3*	L. Ramos Garcia

HT-29 *Mlkl*$^{-/-}$	CRISPR-mediated deletion of *hMlkl*	L. Ramos Garcia
HaCaT *Mlkl*$^{-/-}$	CRISPR-mediated deletion of *hMlkl*	L. Ramos Garcia
HaCaT *Trim25*$^{-/-}$	CRISPR-mediated deletion of *hTrim25*	L. Ramos Garcia

Table 2.13. Genetically modified cell lines

2.7. Cell Biology

2.7.1. Cell culture

All cell lines were cultured in Dulbecco's modified Eagle's medium (DMEM) supplemented with 10% heat inactivated FBS and 1x Penicillin/Streptomycin. Cells were cultured in a tissue culture incubator with humidified air in 10% CO_2 at 37°C. Cells were grown until confluent in a T150 cm^2 tissue culture flask and passaged approximately every 3 days, or prior to reaching 100% confluency.

To passage cells, the existing media was discarded and cells were washed with phosphate buffer saline (PBS) once prior to adding trypsin solution (5 ml per T150 cm^2 tissue culture flask). Cells were incubated with trypsin for 10 minutes to allow detachment from the plate and resuspended in DMEM medium for replating or experimental purposes.

To maintain the stocks of cell lines, cells were frozen and stored in liquid nitrogen. To this end, cells of a T150 cm^2 tissue culture flask were harvested, resuspended in 5 ml of freezing medium and aliquoted into cryotubes.

2.7.2. Transfection of cells

2.7.2.1. Transient Knockdown of genes by siRNA

siRNA-mediated gene silencing was performed using DharmaFECT4 transfection reagent via reverse transfection of 100 nM siRNA (see Table 2.14). Briefly, the siRNA was diluted in Opti-MEM and mixed with DharmaFECT4 transfection reagent. The mix was vortexed and incubated for 10 min at room temperature (RT). The siRNA/ DharmaFECT4 mix was added to each well (231 µl per 6-well, 20 µl per 96-well plate) and cells were plated at the desired concentration in fresh media. Following 24 h, the media was removed and fresh media was added. After 48 h incubation, cells were treated as desired or left untreated and subsequently harvested for further analysis. HaCaT cells were seeded at a density of $5x10^5$ cells/well in 6-well plates or $3x10^3$ cells/well in 96-well plates.

Plate	10 µM siRNA (µl)	OptiMEM (µl)	DharmaFECT4 (µl)
6-well	11.25	217.5	2.25

Table 2.14. Volumes of siRNA/DharmaFECT4 transfection mix.

2.7.2.2. Transfection of DNA for CRISPR-Cas9-mediated gene deletion

Transient transfection of DNA was performed to induce CRISPR-Cas9-mediated deletion of various genes. MDF and L929 cell lines were transfected using Viromer YELLOW transfection reagent. For a single well of a 6-well plate, 2 µg of total DNA was diluted in the provided buffer into a volume of 180 µl. In a separate tube, a droplet of 0.8 µl of Viromer transfection reagent was mixed with 19.2 µl of Viromer buffer and immediately vortexed. The 180 µl of diluted DNA was added to the 20 µl of Viromer solution, swiftly mixed and incubated for 15 min at RT. The 200 µl of transfection complex was added to the cells, previously seeded at 50% confluency.

HT-29 and HaCaT cell lines were transfected via electroporation using Neon Electroporation System according to manufacturer's instructions. For the 10 µl tip, $5.6x10^6$ cells were resuspended in 10 µl of resuspension buffer containing 1 µg of DNA. Cells were electroporated at 1,300 V for 20 ms with 2 pulses. The

electroporated cells were plated in a well of a 6-well plate containing 2 ml of antibiotic free media.

2.7.2.3. Stable lentiviral transduction

Lentiviral supernatants were generated by co-transfection of each expression vector (pTRIPZ or pF TRE3G rtTAAd) with two packaging vectors (psPAX2 and pMD2.G) into HEK293T cells using Effectene transfection reagent. Briefly, HEK293T cells were seeded in 75 cm^2 flasks (T75) at 45-50% confluency. The following day, HEK293T were transfected by diluting the three plasmids in 1.2 ml of Effectene transfection buffer at the concentrations indicated in Table 2.15. The diluted plasmids were then mixed with 30 µl of Effectene Enhancer solution prior to adding 42 µl of Effectene transfection reagent. The mix was vortexed and incubated for 5 min at RT prior to adding it to HEK293T cells. Following 16 h of transfection, the media was removed and 12 ml of fresh media was added.

Plasmids	µg
psPAX2	4.4
pMD2.G	1.8
pTRIPZ / pF TRE3G rtTAAd	5.8

Table 2.15. Amount of expression and packaging plasmids used to generate lentiviral supernatants.

Lentiviral particles were used to transduce a variety of doxycycline (DOX)-inducible *Mlkl* constructs in MDF *Mlkl*$^{-/-}$ cells. The lentiviral supernatants were harvested 48 hours after transfection, filtered using a 45 µm filter, and added to MDF *Mlkl*$^{-/-}$ cells previously seeded in a T75 flask at 50% confluency alongside polybrene (1:1000 dilution). After 72 hours, the viral supernatant was removed and fresh medium was added containing puromycin (1.5 µg/ml) for selection. The puromycin selection was continued until all cells in a control flask had died.

2.7.2.4 Stable retroviral transduction

Retroviral supernatants were generated to immortalize primary MDFs isolated from *Mlkl*$^{K219R/K219R}$ and *Mlkl*$^{WT/WT}$ littermate mice. Retroviral supernatants were produced by transfection of pBABE SV40 (Large T Antigen Δ89-97-missing Bub1) plasmid in RV101 Platinum E cells using Effectene transfection reagent. Briefly, 1.5 µg of pBABE SV40 was diluted in 1 ml of Effectene transfection buffer and mixed with 25 µl of Effectene Enhancer solution and 35 µl Effectene transfection reagent. The mix was incubated at RT for 5 min and carefully added to Platinum E cells, which had been previously seeded at 50% confluency in T75 flasks. After 16h, the medium was removed and 12 ml of fresh medium was added to the cells. Following 48h, the viral supernatants were harvested, filtered through a 45 µm filter and added alongside polybrene (1:1000 dilution) to the primary MDFs previously seeded in a 6-well plate at 50% confluency.

2.7.3. Cell Death assays

Cell death assays were performed in 96-well plates. Cells were seeded at the cell densities indicated in Table 2.16 and the following day were treated with 200 µl of media containing the corresponding drugs. To determine the % of death cells, 1 µg/ml propidium iodide (PI) and 1 µg/ml Hoechst was diluted in media and added to each well (20 µl/well). Following 30 min of incubation, cell death was measured using the Celigo S Cell Imaging Cytometer (Nexcelom Bioscience).

Cell line	Number of cells/well
MDF	6×10^3
HaCaT	6×10^3
HT-29	8×10^3
L929	6×10^3
BMDMs	2.5×10^4

Table 2.16. Number of cells seeded for cell death assays in 96-well plates

2.7.4. RNA isolation, cDNA synthesis and Real Time Quantitative PCR (RT-qPCR)

Primary BMDMs derived from *Trim25*$^{-/-}$ and *Trim25*$^{WT/WT}$ mice were plated into 12-well plates. The following day, lysis of cells and RNA extraction was performed using RNeasy Mini Kit according to manufacturer's instructions. RNA was eluted in nuclease-free water and stored at –80°C. RNA was quantified on a NanoDrop 8000 Spectrophotometer and the purity was determined by the value of A260nm: A280nm ratio and A260nm: A230nm ratio. The sample was considered relatively pure if both ratios were close to 2.

Following RNA extraction, cDNAs were synthesized using QuantiTect Reverse transcription kit according to manufacturer's instructions. Briefly, 0.5 µg of purified RNA was diluted in RNase-free H_2O to a total volume of 12 µl. Next, 2 µl of genomic DNA wipe-out buffer was added to the diluted RNA and incubated for 5 minutes at 42°C. A master mix was prepared as per Table 2.17. 6 µl of this master mix was added to each RNA sample and samples were incubated for 42°C for 30 min followed by a 3 min incubation at 90°C to inactivate the reverse transcriptase. Resulting cDNA was diluted 1:10 in RNase-free water.

RT-qPCR was performed using TaqMan Gene expression Master mix in 384-well plates as detailed in Table 2.17. RT-qPCR was performed using the Quant Studio 6 Flexi RT-PCR machine (Life Technologies). Relative mRNA levels were calculated after normalization to *β-actin* mRNA values using the ΔCt method. Data were analyzed with the SDS programme v2.2.1 (Applied Biosystems).

Master Mix	Reagent	Volume (µl) /sample
cDNA synthesis	QuantiTech RT Buffer	4
(QuantiTect Reverse	QuantiTech RT Primer Mix	1
Transcription Kit)	QuantiTech RT-PCR Enzyme	1
RT-qPCR	TaqMan Reagent	5
(TaqMan Gene Expression	TaqMan Probe	0.5

Assay)	UF H_2O	3.5
	cDNA	1

Table 2.17. Master Mix for cDNA synthesis and RT-qPCR.

2.8. Molecular Biology

2.8.1. Generation of knock-out (-/-) cell lines with CRISPR-Cas9

sgRNAs design to target the gene of interest (Table 2.9) were cloned into expressing vectors. HT-29 and HaCaT cells were transfected by electroporation whereas MDF and L929 cells were transfected with Viromer YELLOW transfection reagent as described in Section 2.7.2.2. Three days after transfection, GFP^+ or RFP^+ cells were selected and seeded in a 96-well plate via Fluorescence activated cell sorting (FACS). Single clones were isolated and screened for deletion of the correspondent gene. Several positive clones were identified and characterized further.

2.8.2. Plasmid preparation

2.8.2.1. Preparation of competent bacterial cells

One Shot TOP10 Chemically Competent *E. coli* cells were purchased from Invitrogen and used for cloning and plasmid amplification. One Shot TOP10 Chemically Competent *E. coli* cells were grown overnight (o/n) on an agar plate. A single colony was utilized to inoculate 2 ml of Luria Broth Medium (LB) and grown o/n in a 37°C shaking incubator. 1 ml of the resulting culture was added to 100 ml of LB and grown at 37°C with vigorous shaking. The culture was grown until reaching an optical density at 600 nm (OD_{600}) of approximately 0.6, which is indicative of an exponential growth phase. The bacterial culture was chilled on ice for 10 minutes and then pelleted by centrifugation at 2500 g for 15 min in a 4°C centrifuge. The pellet was resuspended in 15 ml of TSB and divided into 500 µl working aliquots. Aliquots were stored at -80°C.

2.8.2.2. Chemical transformation of *E. coli* by heat shock

An aliquot of TOP10 Chemically competent *E.coli* cells was thawed on ice. 50 ng of plasmid DNA was added to 100 µl of TOP10 Chemically competent *E.coli* cells and incubated on ice for 20 minutes. Cells were then incubated at 42°C for 30 seconds and were returned to ice immediately for 5 minutes. 1 ml of LB was added to the transformation reaction. Cells were incubated at 37°C for 1 hour. Then, cells were harvested by centrifugation at 15,600 x g for 30 seconds, the LB was removed and cells were resuspended in 100 µl fresh LB. All 100 µl of the transformed bacteria was plated onto an agar plate containing the appropriate antibiotic and incubated at 37°C o/n.

2.8.2.3. Amplification and purification of plasmid DNA

Following o/n incubation, a single colony of the transformed bacteria was picked. The picked colony was grown o/n under shacking conditions at 37°C in 1.5 ml (for mini-prep) or 50 ml (for midi-prep) of LB medium supplemented with the appropriate antibiotic. The bacterial cells were harvested by centrifugation at 4000 rpm for 15 min. Plasmid purifications were performed using Qiafilter Plasmid Mini/Midi-prep kits. DNA was stored at –20°C.

2.8.2.4. DNA quantification

Plasmid DNA concentrations were determined by measuring the absorbance at 260 and 280 nm (A260 nm, A280nm) using the Nanodrop 8000 Spectrophotometer. The purity of the sample was determined by the value of A260nm: A280nm ratio. The sample was considered relatively pure if the ratio obtained was greater than or equal to 1.8

2.8.3. Cloning and mutagenesis

2.8.3.1. Polymerase Chain Reaction (PCR)

PCR reactions were performed using the Q5 Hot Start High Fidelity DNA polymerase. *Mlkl* gene was amplified from genomic DNA derived from *Mlkl* $^{K219R/K219R}$ and *Mlkl* $^{WT/WT}$ BMDMs. The primers utilized for *Mlkl* amplification and sequencing are described in Table 2.10. The PCR reaction performed is detailed in Table 2.18 and Table 2.19.

Reagent	Amount (µl)
Q5 Reaction buffer (5x)	10
dNTPs	1
Forward Primer (10 µM)	2.5
Reverse Primer (10 µM)	2.5
Q5 High GC Enhancer (5x)	10
DNA template	10 ng-1 µg
Q5 Hot Start High Fidelity DNA polymerase	1
UF H_2O	Up to 50

Table 2.18. PCR reaction mix for Q5 Hot Start High Fidelity DNA polymerase

Step	Cycles	Reaction: Time
Hot start	1 cycle	Hot start: 95 ºC for 5 min
Initiation	1 cycle	Denaturing: 95 ºC for 5 min
Amplification	30 cycles	Denaturing: 95ºC for 30 sec Annealing: 55ºC for 1 min Extension: 72ºC for 2 min/kb
Final extension	1 cycle	Extension: 72ºC for 10 min

Table 2.19. PCR reaction program

2.8.3.2. Site-Directed Mutagenesis

cDNA from MDFs was used to clone *Mlkl* in pBluescript vector (XhoI/ AgeI-HF). Subsequently site-directed mutagenesis was performed to create the mutant *Mlkl* constructs listed in Table 2.6. Site-directed mutagenesis was performed using PfuUltra II Fusion HotStart DNA Polymerase. The mutagenesis primers were designed so that the point mutation is flanked by approximately 17 bp on each side. The primers used for mutagenesis are listed in Table 2.8. The forward and reverse complement primers were mixed together (1:1 ratio) and diluted in UF water to a final concentration of 10 µM for each primer. For one reaction, the reagents were mixed as indicated in Table 2.20 and the mutagenesis was performed as described in Table 2.21.

Reagent	Amount (µl)
Pfu buffer (10X)	2.5
dNTPs (10 mM)	1
Primer Mix (10 µM)	2.5
DNA template (pBluescript-*Mlkl*)	5 -50 ng
PfuUltra II Fusion HotStart DNA Polymerase	1
UF H_2O	Up to 25

Table 2.20. PCR reaction mix for mutagenesis

Step	Cycles	Reaction: Time
Initiation	1 cycle	Denaturing: 95 ºC for 30 sec
Amplification	18 cycles	Denaturing: 95ºC for 30 sec Annealing: 55ºC for 1 min Extension: 68ºC for 2 min/kb
Final extension	1 cycle	Extension: 68ºC for 10 min

Table 2.21. PCR reaction program for mutagenesis

Upon completion of the PCR reaction, template DNA was digested with 1 µl DpnI enzyme for 1-2 h at 37ºC. 10 µl of the reaction was transformed into competent cells and the resulting colonies were screened for the presence of the

mutation by sequencing. The pBluescript-*Mlkl* plasmids containing the mutation of interest were sub-cloned to a pTRIPZ lentiviral vector (detailed below).

2.8.3.3. Restriction endonuclease digestion of DNA

Digestion of DNA was performed in CutSmart Buffer. To sub-clone pBluescript-*Mlkl* plasmids, digestion was performed using XhoI and AgeI-HF restriction enzymes by mixing the reagents as described in Table 2.22. The reaction was first incubated at RT for 30 min, following 1h incubation at 37ºC. Following the digestion of TRIPZ vector, alkaline phosphatase was used to remove the 5' phosphate and reduce the occurrence of vector self-ligation. 1 µl Phosphatase alkaline and 2 µl of buffer was added to the digestion reaction and the reaction was further incubated for 1 h at 37ºC.

Reagent	Amount (µl)
CutSmart Buffer	2
XhoI	0.25
AgeI-HF	0.25
UF H_2O	15.5
DNA (100-500ng)	2

Table 2.22. Digestion reaction for pBluescript-*Mlkl* with XhoI and AgeI-HF

2.8.3.4. Agarose Gel Electrophoresis

1 % agarose gels were prepared in TAE buffer and supplemented with Gel Red nucleic acid stain (1/10,000). DNA samples were mixed with 6x DNA loading dye, and loaded into the gels. Electrophoresis was performed at 10 V/cm. The DNA in the gels was visualized using a UVB Biodoc IT TM transilluminator and photographed using a Polaroid DS.34 instant film system. The DNA fragments in the gel were cut with a scalpel and purified using QIAquick Gel extraction kit according to manufacturer's instructions.

2.8.3.5. Ligations

10 µl ligation reactions were prepared by mixing 1 µl of T4 DNA ligase buffer (10x), 4 µl of digested vector, 4 µl digested insert and 1 µl of T4 DNA ligase. Samples were incubated 1 hr at RT or o/n at 4°C. The ligated constructs were transformed into TOP10 *E.coli* competent cells and resulting colonies were picked and grown for mini-prep as previously described.

2.8.3.6. Sequencing

Purified plasmid DNA or PCR products were sequenced by Eurofins Genomics. Sequencing files were visualized using DNA Dynamo Software.

2.9. Protein Techniques

2.9.1. Total protein extraction and quantification

Following treatment according to the experimental procedures, cells were washed with ice-cold PBS and lysed using DISC lysis buffer containing complete protease inhibitor cocktail and phosphatase inhibitors (Complete DISC Lysis Buffer). Cells were scraped using cell scrapers and lysates were cleared by centrifugation at 4°C and 14,000 rpm for 15 minutes.

Protein concentrations were determined using a Bio Rad protein Bradford assay in accordance with the manufacturer's instructions. This assay is based on the Lowry protocol (Lowry et al., 1951) and uses reagents A, S and B. Briefly, 2µl of each lysate was mixed with 18µl of UF water. 100µl of the mix of reagent S and A (reagents are mixed in 1/50 ratio of S/A) was added. Finally, 800µl of reagent B is added and solutions are incubated for 15 minutes at RT. Absorbance (OD) was measured, against a blank containing UF water as a sample at 750 nm on a NanoDrop 8000 Spectrophotometer and total protein concentration was determined. After protein concentration was determined, 6X loading die was added to 100 µg of protein diluted in a total volume of 100 µl. Samples were boiled at 100°C for 10 minutes and then stored at –20°C until immunoblotting or

subjected to downstream processing.

2.9.2. Cytosolic and membrane cell fractionation

Two methods for cellular fractionation were utilised, based on detergent Triton X-114 or on sucrose density gradient centrifugation.

2.9.2.1. Fractionation with Triton X-114

Cells of a 15-cm dish were washed with ice-cold PBS and scraped using 0.5 ml Triton X-114 lysis buffer containing complete protease inhibitor cocktail and phosphatase inhibitors. Cells were incubated on ice for 30 minutes. The cell lysate was centrifuged at 15,000 g for 10 min at 4°C. The supernatant was then harvested as the detergent soluble fraction. This fraction was warmed at 30°C for 3 min and subjected to centrifugation at 1500 g for 5 min at RT. The aqueous layer was collected and recentrifuged at 1500 g for 5 min at RT to remove the contamination from the detergent-soluble layer and kept as the cytoplasmic fraction (C). The detergent enriched layer was diluted with basal buffer (20 mM HEPES, pH 7.4, 150 mM NaCl) and recentrifuged at 1500 g for 5 min at RT. The washed detergent-enriched layer was diluted with the basal buffer to the same volume as the cytoplasmic fraction and saved as the membrane enriched fraction (M). Samples fractionated by this method were subjected to downstream processing including ubiquitin pull-down, SDS-PAGE and immunoblotting.

2.9.2.2. Fractionation by sucrose density gradient centrifugation

Cells seeded in 15-cm dishes were washed with ice-cold PBS and scraped using 0.5 ml/dish of fractionation lysis buffer containing protease and phosphatase inhibitors (supplemented fractionation buffer). Cytosolic and crude membrane fractions were separated by centrifugation at 11,000 g for 5 min at 4°C. The cytosolic fraction (top fraction) was further solubilized in permeabilization buffer and digitonin was added to achieve a final concentration of 1% wt/vol. The detergent fraction (bottom fraction) was further permeabilized by adding permeabilization buffer containing 1% wt/vol of digitonin and clarified

by centrifugation. Samples fractionated by this method were subjected to downstream processing by BN-PAGE and immunoblotting.

2.9.3. SDS-polyacrylamide gel electrophoresis (SDS-PAGE)

SDS-PAGE was carried out to detect the presence of proteins in a given sample. Proteins are separated according to their molecular weight. Small proteins migrate faster moving to the bottom of the polyacrylamide gel whereas large proteins migrate slowly remaining at the top. XCell SureLock Tanks were utilised (ThermoFisher). Samples were separated by SDS-PAGE using NuPAGE Novex 4-12% Bis-Tris 1.0 mm 20/26 well-precast midi protein gels in MOPS buffer. Following separation by SDS-PAGE proteins were transferred onto PVDF membranes using a T42 wet-transfer unit.

2.9.4. Blue Native-PAGE (BN-PAGE)

Cytosolic and membrane lysates separated by sucrose density gradient centrifugation were prepared for BN-PAGE by mixing as follows: 70 µl of cytosolic/membrane lysate, 25 µl 4X NativePAGE Buffer and 5 µl of NativePAGE G250 Sample Additive. Subsequently, both fractions were resolved on a 4–16% Bis Tris Native PAGE gel. Samples were run at 150V for 45 min with dark cathode buffer at 4°C. Following this time, the dark cathode buffer was replaced by light cathode buffer and samples were run for another 45-60 min. Proteins were transferred to PVDF membranes at 50V for 3h. The transfer buffer was supplemented by addition of 2 ml of 20% SDS in a 1L transfer tank. Following transfer, PVDF membranes were de-stained by washing 3 times with 40% methanol, 10% acetic acid for 5 min/wash or until the membrane was light blue. Prior to immunoblotting, proteins were denatured by soaking the PVDF membrane in 6 M guanidine hydrochloride, 10 mM Tris·HCl pH 7.5, and 5 mM β-ME for 2h at RT.

2.9.5. Immunoblotting

PVDF membranes were blocked in 5% BSA in TBS-T for 20 min. The membrane was then incubated o/n at 4°C with the primary antibody diluted in 5% BSA. Membranes were washed 3 times for 5 mins with TBS-T wash buffer. The secondary antibody was added to 5% milk in TBS-T and the membranes were incubated for 1h at RT, followed by 3 washes in TBS-T wash buffer for 15 min/wash. The membranes were then incubated with ECL for 1-3 min. Membranes were developed using Kodak X-ray films or ChemiDoc Touch Imaging System (Bio-rad). For detection of MLKL ubiquitylation SuperSignal West Femto Maximum Sensitivity Substrate was mixed with ClarityWestern ECL in a 1:3 ratio.

2.9.6. MLKL oligomerization assay

Cells of a 10-cm dish were washed with ice-cold PBS and lysed in complete DISC buffer. For non-reducing conditions, β-ME was removed from the 6X loading die and samples were not boiled before loading them into the gel to preserve disulphide bonds. SDS-PAGE and immunoblotting was performed as described in Section 2.9.3 and 2.9.5, respectively.

2.9.7. Purification of endogenous ubiquitin conjugates

Ub conjugates were purified from HT-29 and MDF cells through the use of a Ub affinity reagent (GST-TUBE) [249].GST-TUBE was designed by using four tandem UBA domains, on the basis of the theory that tetraubiquitin was required for efficient proteasomal degradation [249]. In particular, UBA domains from the protein ubiquilin-1 were utilised, and the UBA domains were separated by a flexible linker (poly-glycine residues) [249].

Cells were lysed in DISC lysis buffer supplemented with protease inhibitors, 1 mM DTT, PR619 (10 μM) and GST-TUBE (50 μg/ml; 50 μg TUBE/mg protein lysate). Cell lysates were rotated at 4°C for 1 h then clarified by centrifugation at 14,000 rpm for 15 min at 4°C. 20 μL GSH beads were added to each sample and immunoprecipitations were performed o/n. Beads were washed 4 times in washing buffer (PBS-Tx supplemented with 10 μM PR-619) and bound proteins

eluted by boiling in 60 µl 1x SDS loading dye. When USP21 DUB digestion was performed, each sample was split in two after the fourth wash. 2 µM of USP21 in 20µl of DUB digestion buffer was added to the dried beads and digestion was performed for 1h at 37°C. Samples were eluted by boiling in 40 µl 2x SDS loading dye. For the TUBE experiments were MLKL oligomerisation is shown, the TUBE pull-down was performed as described above but without the DTT supplementation in the lysis buffer. In this case, proteins were eluted in non-reducing loading dye.

For linkage-specific Ub pulldowns, cells were lysed and clarified as described in Section 2.9.1.

For K48-specific Ub pulldown, 20 µl Protein A/G beads were preincubated with 1.5 µl of α-K48-specific Ub antibody. As a control α-V5 tag antibody was utilized.

For K63-linked and M1-linked chains specific ubiquitin tools were utilized. To isolate K63-linked ubiquitin chains, the UIM domains of RAP80 were engineered in tandem (three UIMs) [250]. The UIM domains are separated by a 7 amino acid linker, which help to orient the UIM binding sites in phase for optimal contact across all three K63-linked Ub units [250]. To isolate M1-linked polyubiquitin chains, I employed a Met1-linkage specific Ub-binder (M1-SUB) based on NEMO's UBAN region [51, 251].

For the K63-linked Ub pulldown 20 µl streptavidin beads were preincubated with 4 µg K63 UIM recombinant protein or K63 UIM Mutant as a control. For the M1-linkage specific ubiquitin pulldown 20 µl of GSH beads were mixed with 28.5 µg of M1-SUB or GST Control. In all cases beads were preincubated for 2 h at 4°C. Following preincubation, equal amounts of clarified lysate were added to the beads and immunoprecipitation was performed o/n.

2.10. Mass Spectrometry

2.10.1. Identification of endogenously ubiquitylated Lys

2.10.1.1. Lysate preparation and protein precipitation

MDFs were treated with Tumor necrosis factor, smac mimetics and caspase inhibitor zVAD-fmk (TSZ) for 2 h or left untreated, washed with iced-cold PBS and frozen at -80°C. Cells were lysed in di-Gly lysis buffer (8 M urea, 50 mM Tris pH 8, 50 mM NaCl, 5.5 mM ChloroAA) supplemented with protease inhibitor cocktail and phosphatase inhibitor and the lysate was incubated 20 min on ice. Samples were sonicated and clarified by centrifugation at 14,000 rpm for 15 min at 4°C. Protein concentration was quantified using BCA assay and approximately 20 mg of protein per sample was used as total starting material. Protein was precipitated by adding chloroform and methanol to the lysates. Briefly, lysates were mixed with 4x volumes of 100% methanol and vortexed. Next, 1x volume of chloroform was added to the samples followed by 3x volumes of HPLC H_2O. Proteins were precipitated by centrifugation at 8500 rpm at RT for 15 min. The pellet was washed by adding 100% methanol and swirling the tube multiple times. A total of 3 washes with methanol was performed and samples were centrifuged at 8500 rpm for 3 min at RT between washes. During the last wash step, the pellet was vortexed for a couple of seconds in methanol to break it into small pieces. The methanol was carefully aspirated and the protein precipitate was processed as described below.

2.10.1.2. Reduction, alkylation and digestion

The protein precipitate was re-dissolved in 7 ml denaturation buffer (6M urea, 2M thiourea, 50 mM Tris, pH 8). Samples were reduced by adding DTT to a final concentration of 1 mM and incubated 1 h at RT with rotation. ChloroAA was added to a final concentration of 5 mM and samples were incubated for 1 h at RT in the dark with rotation. Proteins were subsequently digested by adding 50 μg of LysC for 4 h. Subsequently, 4 volumes (28 ml) of 25 mM TRIS, pH 8 was added to the samples and they were subsequently digested by addition of 60 μg of trypsin (Promega) and o/n incubation at RT with rotation. Digestion was stopped by adding trifluoroacetic acid (TFA) to a final concentration of 0.5% (1.75 ml of 10% TFA). Samples were incubated for 10 min at RT.

2.10.1.3. Peptide desalting and lyophilization

Following digestion, peptides were desalted using Sep-Pak Vac tC18 cartridges. Briefly, cartridges were activated with 9 ml of ACN. The column was then equilibrated with 10 ml of 0.1% TFA and peptides were loaded into the column. Peptides were washed and desalted using 12 ml of 0.1 % TFA and eluted with 5 ml of 50% ACN/0.1%TFA into a 12-ml Duran glass tube. The eluate was frozen in liquid nitrogen and the peptides were dried in a freeze dryer. After drying was finished, dried peptides were collected at the bottom of the tube by centrifugation at 4000 rpm 5 min at RT.

2.10.1.4. Di-Gly immunoprecipitation

The dried peptides were resuspended in 1.3 ml of 1x IAP buffer (50 mM MOPS pH 7.4, 10 mM Na_2HPO_4, 50 mM NaCl) by carefully pipetting up and down. The pH was adjusted to 7 by adding 30-90 µl 1M Tris pH 10 to facilitate peptide resuspension. The resuspended peptides were centrifuged at 13200 rpm for 8 min at 4°C to remove any insoluble material. The di-Gly remnant antibody beads were washed 3x with 750 µl of cold 1x IAP buffer by centrifugation at 2700g for 1.5 min at 4°C. 40 µl of antibody beads (50% slurry) was used for each immunoprecipitation and incubated with the resuspended peptides for 2.5h at 4°C with rotation. Following the immunoprecipitation, samples were centrifuged at 2700g for 1.5 min at 4°C and the supernatant was removed. The beads were washed twice with 750 µl cold MilliQ H_20. After the second wash, the beads were resuspended in 100 µl cold MilliQ H_20 and placed in a Pierce Spin column placed in a 1.5 ml tube. The columns were spin at 2700g, 1.5 min at 4°C to dry the beads and then they were transferred to a fresh 1.5 ml tube. Di-Gly peptides were eluted by addition of 80 µl of 0.15%TFA followed by centrifugation at 2700g for 1.5 min at 4°C. A second elution was performed by adding another 80 µl of 0.15%TFA to the beads in the column and spin at 2700g for 1.5 min at 4°C into the same tube as the first elution.

2.10.1.5. TMT labelling

The six samples from the di-Gly immunoprecipitation were labelled by TMT10plex Isobaric Mass Tag Labelling Reagents Set according to manufacturer's instructions. Briefly, TMT label reagents were equilibrated at RT for 30 min. For each 0.8 mg of reagent vial, 41 µl of anhydrous ACN was added to each tube and the reagent was allowed to dissolve for 5 minutes with occasional vortex. The tubes were centrifuged to gather the solution at the bottom of the tube. The entire tube (41 µl) was added to each sample and incubated for 1 h at 21°C in an Eppendorf ThermoMixer with mixing at 1200 rpm. To quench the reaction, 8 µl of 5% hydroxylamine was added to the sample and incubated for 15 minutes at 21°C in an Eppendorf ThermoMixer with mixing at 1200 rpm. The six samples were combined in a new centrifuge tube and the labelled peptide sample was dried in a speedvac.

2.10.1.6. LC MS/MS analysis for di-Gly immunoprecipitation

LC MS/MS and data analysis was performed by Dr. Lu Yu, who also provided the description for the method as described below. The dried peptide mixture was resuspended in 0.1% NH_4OH/100% H_2O, and fractionated on an XBridge BEH C18 column (2.1 mm i.d. x 150 mm, Waters) with an initial 5 min loading then linear gradient from 5% ACN/0.1% NH_4OH (pH 10) – 35% CH_3CN /0.1%NH_4OH in 30min, then to 80% CH_3CN /0.1% NH_4OH in 5 min and stayed for another 5 min. The flow rate was at 200 µl/min. Fractions were collected ay every 30sec to a 96 well-plate by column from retention time at 3 min to 45 min, and then pooled by rows to 8 concatenated fractions and dried in SpeedVac.

The peptides were reconstituted in 20 µl of 0.1% FA/H_2O and then injected for on-line LC-MS/MS analysis on the Orbitraip Fusion Lumos hybrid mass spectrometer coupled with an Ultimate 3000 RSLCnano UPLC system (both from Thermo Fisher). Samples were first loaded and desalted on a PepMap C18 nano trap (100 µm i.d. x 20 mm, 100 Å, 5µl) then peptides were separated on a PepMap C18 column (75 µm i.d. x 500 mm, 2 µm) over a linear gradient of 8–32% CH_3CN/0.1% FA in 90 min, cycle time at 120 min at a flow rate at 300 nl/min. The MS acquisition used MS3 level quantification with Synchronous

Precursor Selection (SPS) with the Top Speed 3s cycle time. Briefly, the Orbitrap full MS survey scan was m/z 375 – 1500 with the resolution 120,000 at m/z 200, with AGC set at 4e5 and 50 ms maximum injection time. Multiply charged ions (z = 2 – 5) with intensity threshold at 1e4 were fragmented in ion trap at 35% collision energy, with AGC at 1e4 and 50 ms maximum injection time, and isolation width at 0.7 Da in quadrupole. The top 5 MS2 fragment ions were SPS selected with the isolation width at 0.7 Da, and fragmented in HCD at 65% NCE, and detected in the Orbitrap to get the report ions' intensities at a better accuracy.

The raw files were processed with Proteome Discoverer 2.2 (Thermo Fisher) using both SequestHT and Mascot (V2.3) search engines to search against the reviewed Uniprot protein database of *Mus Musculus* (2018) plus the crap database. The precursor mass tolerance was set at 25 ppm and the fragment ion mass tolerance was set at 0.5 Da. Spectra were searched for fully tryptic peptides with maximum 2 miss-cleavages. Carbamidomethyl (C) and TMT6plex (Peptide N-terminus) were set as static modifications, and the dynamic modifications included Deamidation (N, Q), Oxidation (M), and TMT6plex (K, GlyGlyK). Peptides were validated by Percolator with q value set at 0.05 for the Decoy database search. The search result was filtered by the Consensus step where the protein FDR was set at 0.01 (strict) and 0.05 (relaxed). The TMT10plex reporter ion quantifier used 20 ppm integration tolerance on the most confident centroid peak at the MS3 level. Both unique and razor peptides were used for quantification. Peptides with average reported S/N>3 were used for protein quantification. Only master proteins were reported.

2.10.1.7. LC MS/MS Statistical analysis

To calculate the fold-change in di-Gly peptide abundance, the data was first transformed to log base 2. This transformation normalizes the data and allows for analysis using parametric statistical tests. To determine the statistical significance, the normalised abundance of di-Gly peptides were analysed via an unpaired, two-tailed student t-test using Perseus Software. Statistical significance is indicated via a volcano plot generated with Perseus Software

where the p-value and the difference in peptide abundance is represented. For this analysis, the three replicates were taken into consideration.

2.10.1. Endogenous hMLKL immunoprecipitation for LC MS/MS Analysis

2.10.1.1. Endogenous hMLKL immunoprecipitation

HT-29 cells were treated with TSZ for 8 h, washed with iced-cold PBS and frozen at -80°C. Cells were lysed in complete DISC lysis buffer and incubated 20 min on ice. Samples were sonicated and clarified by centrifugation at 14,000 rpm, 4°C for 15 min. Protein concentration was quantified and approximately 3.5 mg of protein was utilised per sample. Pierce Protein A/G Plus Agarose Beads were washed once with DISC lysis buffer and preincubated with the correspondent antibody for 2 h at 4°C. To endogenously immunoprecipitate hMLKL, anti-MLKL antibody (Clone 3H1, Millipore, purified rat) was utilized and as a control anti-HA (Roche, purified rat) antibody was used. 60 µl of beads and 10 µl of each antibody was utilized per immunoprecipitation. Following pre-incubation, the beads were washed once with lysis buffer and incubated with the lysate o/n at 4°C with rotation. Following immunoprecipitation, beads were washed 4x in IP washing buffer followed by two washes with AmBic Buffer. As a control for the immunoprecipitation, 10 µl of beads were removed from each sample and proteins were eluted by resuspending in 30 µl 2x SDS loading dye and boiling for 10 min. The remaining beads were resuspended in 500 µl of AmBic Buffer and protein digestion was performed by addition of 1 µg of trypsin (Promega) per sample. Samples were incubated 1h at 37°C with rotation and an additional µg of trypsin was added to each sample prior to further incubation for 3 h at 37°C with rotation. After digestion, peptides were collected by spinning down the samples. To further extract the peptides from the beads, 100 µl of 25% ACN/0.1% FA solution was added, mixed and pooled with the supernatant from above. The collected supernatant was acidified by adding FA to a final concentration of 1%. ACN was added to the final solution to over 50% of final concentration and the peptides were subjected to SpeedVac until completely dry.

2.10.1.1. LC MS/MS analysis for hMLKL immunoprecipitation

LC MS/MS and data analysis was performed by Dr. Lu Yu and Dr. Mercedes Pardo Calvo, who also provided the description for the method as described below. The dried peptides were reconstituted in 20 µl of 0.1% FA/H_2O and then injected for on-line LC-MS/MS analysis on the Orbitraip Fusion Lumos hybrid mass spectrometer coupled with an Ultimate 3000 RSLCnano UPLC system (both from Thermo Fisher). Samples were first loaded and desalted on a PepMap C18 nano trap (100 µm i.d. x 20 mm, 100 Å, 5µ), and then peptides were separated on a PepMap C18 column (75 µm i.d. x 500 mm, 2 µm) over a linear gradient of 8–32% CH_3CN/0.1% FA in 90 min (cycle time at 120 min) at 300 nl/min flow rate. The MS acquisition used standard data-dependant method with the Top Speed 3s cycle time. Briefly, the Orbitrap full MS survey scan was between m/z 375 – 1500 with the resolution 120,000 at m/z 200, with AGC set at 4e5 and 50 ms maximum injection time. Multiply charged ions (z = 2 – 5) above the intensity threshold at 1e4 were isolated at 1.6 Da in quadrupole and fragmented by HCD higher energy collision-induced dissociation) at 30% collision energy, then detected in ion trap with AGC at 1e4 and 50 ms maximum injection time. Raw mass spectrometry data files were analysed with Proteome Discoverer 1.4 (Thermo). Database searches were carried out using Mascot (version 2.4) against the Uniprot human reference database (January 2018, 21123 sequences) with the following parameters: Trypsin was set as digestion mode with a maximum of two missed cleavages allowed. Precursor mass tolerance was set to 10 ppm, and fragment mass tolerance set to 0.5 Da. Acetylation at the N terminus, oxidation of methionine, carbamidomethylation of cysteine, deamidation of asparagine and glutamine, and di-Gly modification of lysine were set as variable modifications. Peptide identifications were set at 1% FDR using Mascot Percolator. Protein identification required at least one peptide with a minimum score of 20.

2.11. Generation of *Mlkl* ^{K219R} knockin mouse

The generation of the *Mlkl*^{K219R} animals was conducted in the Walter and Eliza Hall Institute of Medical Research (WEHI). Cas9 mRNA together with the ssDNA

repair oligo and the sgRNA targeting the region surrounding K219 of the murine *Mlkl* gene was microinjected into the pro-nucleus of fertilized oocytes obtained from C57BL/6 mice. The injected embryos were transferred to foster mothers and allowed to develop to term. Mutations in the genome of progeny were determined by analysis of genomic DNA and sequencing.

2.12. Isolation of primary cells

2.12.1. Isolation of Bone Marrow Derived Macrophages (BMDMs)

The bone marrow from tibias and femurs of *Mlkl* $^{K219R/K219R}$ and *Mlkl* $^{WT/WT}$ as well as from *Trim25* $^{WT/WT}$ and *Trim25* $^{-/-}$ mice were extracted by placing a needle into the bone and flushing some media with a syringe. After spinning the cells at 1200 rpm for 5 min, cells were seeded in uncoated 14-cm dishes in DMEM supplemented with cytokine recombinant murine M-CSF (10 ng/ml). After 3 days, fresh M-CSF was added to the media (10 ng/ml). Following 6 days of incubation, cells are differentiated into macrophages and can be kept for a week. Cells were washed to remove unwanted cells and BMDMs were split for experiments.

2.12.2. Isolation of Mouse Dermal Fibroblast (MDFs)

Primary MDF were isolated from the tail of littermate adult mice (6-8-week-old) harbouring *Mlkl* $^{K219R/K219R}$ and *Mlkl* $^{WT/WT}$ genotypes. To this end, the entire tail of the mouse was cut and placed in a dish containing ethanol for 1 minute. A longitudinal incision of 5 mm was made at the top part of the tail and the skin was peeled off using thin tweezers. The tip of the tail was discarded (pink part) and the skin was placed in a 10-cm dish containing 10 ml DMEM (10% FBS + Pen/Strep). The skin of the tail was then chopped in small pieces (2 mm) using a scalpel and the pieces were collected in a 15 ml falcon tube. The tube was spin at 1200 rpm for 3 min at 4°C. The media was removed and 10 ml of PBS was added. The tube was gently rocked for 5 times and then centrifuged at 1200 rpm for 3 min at 4°C. The PBS was discarded and 3 ml of ice-cold trypsin + EDTA (Sigma) was added and incubated for 45 min at 37°C. Following incubation, 6 ml

of media was added and the tube was shaken vigorously (30x). The resuspended skin was filtered through a 100 μm strainer in a 50 ml falcon tube. The strained media containing the MDFs was placed in a 10-cm dish and incubated at 37°C, 5% CO_2. A couple of days later, MDFs were immortalised as described in Section 2.7.2.4.

2.13. Confocal Microscopy

2.13.1. Immunofluorescence staining for P-MLKL

HT-29 cells (parental and *Mlkl*$^{-/-}$) were plated on 13 mm glass coverslip placed in a 24-well plate (7 x 10^5 cells/well) and treated as indicated. Cells were then fixed in 4% PFA for 10 min and permeabilised with 1x PBS, 0.5% Triton X-100. Following 10 min permeabilization, cells were blocked for 1 hr in PBS 5% BSA. The indicated primary antibodies were diluted in 1x PBS, 1% BSA and incubated in a humid chamber o/n at RT. Primary antibodies were then washed 3x with 1x PBS, 0.1% Triton X-100 for 10 min. Secondary Alexa Fluor conjugated antibodies were diluted in 1x PBS, 1% BSA, and incubated for 2 hr at RT. Wheat Germ Agglutinin, Alexa Fluor 633 Conjugated antibody was added together with the secondary antibodies. Following incubation, the antibodies were washed three times with 1x PBS, 0.1% Triton X-100 for 10 min. During the second wash nuclei were stained by adding DAPI (1:1000, Invitrogen). Each slide was then washed with UF water and mounted onto glass slides with ProLong Gold Antifade Mountant. Stained slides were visualized using the LSM710 Zeiss microscope, objective 40x or 63x Zeiss.

2.13.2. Proximity ligation assay (PLA)

PLA was performed according to the manufacturer's protocol using the Duolink Detection Kit. Cells were examined with a confocal microscope (objective x 40, Zeiss LSM 710).

2.14. Structural predictions of mutations

To predict the effect of mutating K219, Pymol Software *(www.pymol.org)* was utilised on the resolved structure of mMLKL (PBD: 4BTF) [178].

2.15. Statistical analysis

Graphs and statistical analysis were performed using GraphPad Prism V7.0. All statistical analysis shown in this thesis for cell death data were calculated by two-way ANOVA with Bonferroni correction. Data is representative of two or more biological replicates. Three technical repeats were performed in each experiment. Error bars indicate standard deviation (SD).

3. Ubiquitin-mediated modulation of MLKL

3.1. Endogenous MLKL is ubiquitylated during necroptosis

3.1.1. Ubiquitylation of MLKL correlates with TNF-induced necroptotic cell death progression

Ub-signalling plays a crucial regulatory role downstream of TNFR1 activation. RIPK1 and RIPK3 have been shown to be ubiquitylated in Complex-II, modulating necroptosis [143]. Since MLKL is the last effector in the necroptotic pathway, I asked whether it was also modulated in a Ub dependent manner. To investigate this, I first determined the kinetics of cell death in Mouse Dermal Fibroblast (MDFs) and HT-29 human colorectal cancer cells following stimulation with TNF (T), Smac Mimetic 164 compound (S) and z-VAD-fmk (Z), (TSZ), to engage TNF-induced necroptosis. A time course experiment revealed that TSZ killed HT-29 cells with a slower kinetics than MDFs, with cell death starting at 4 and 1.5h, respectively **(Figures 3.1A and B)**. Importantly, in both cases the death was inhibited by treatment with RIPK1 kinase inhibitor GSK'963 (RIPK1i), confirming the engagement of the necroptotic pathway **(Figures 3.1A and B)**. To test whether endogenous MLKL is ubiquitylated at any point during TNF-induced necroptosis, I isolated polyubiquitylated proteins using Tandem Ub Binding Entities (TUBEs) [249] after stimulating the cells with TSZ for the indicated time points. While MLKL was non-ubiquitylated under base-line conditions in human and mouse cells, high molecular weight species of MLKL, corresponding to ubiquitylated MLKL, were observed following treatment with TSZ **(Figure 3.1C and D)**. This smearing pattern was due to ubiquitylation of MLKL as it was lost following treatment with the DUB USP21 **(Figure 3.1C)**. Interestingly, in both cell lines the appearance of ubiquitylated MLKL occurred at the time point at which cells were starting to undergo cell death (4h timepoint in HT-29 cells and 1.5h timepoint in MDFs cells). MLKL ubiquitylation became more prominent at the latest times measured. Consistent with the notion that RIPK3-mediated phosphorylation of MLKL is a hallmark for necroptotic cell death, I observed that phosphorylation and ubiquitylation occurred with the same kinetics **(Figure 3.1C and D)**. Importantly, both modifications occurred within the

same pool of MLKL molecules, as demonstrated by immunoblotting with an anti-P-MLKL antibody of TUBE purified samples **(Figure 3.1D).** Therefore, these data suggest that the active form of MLKL is modulated by Ub.

To test whether ubiquitylation of MLKL correlates with necroptotic cell death progression, I stimulated mouse fibrosarcoma L929 cells with SZ in the absence of TNF. These cells undergo necroptosis upon stimulation with SZ or Z alone due to autocrine production of TNF [252], albeit with slower kinetics when compared to TNF treatment **(Figure 3.1E).** Both, SZ and TSZ caused the appearance of ubiquitylated MLKL, although SZ again had a slower kinetics when compared to TSZ **(Figures 3.1F and G).** In both cases, the Ub smearing pattern of MLKL occurred at the same time as MLKL phosphorylation and cell death **(Figure 3.1E-G).** These data may indicate a link between MLKL phosphorylation, ubiquitylation and cell death progression.

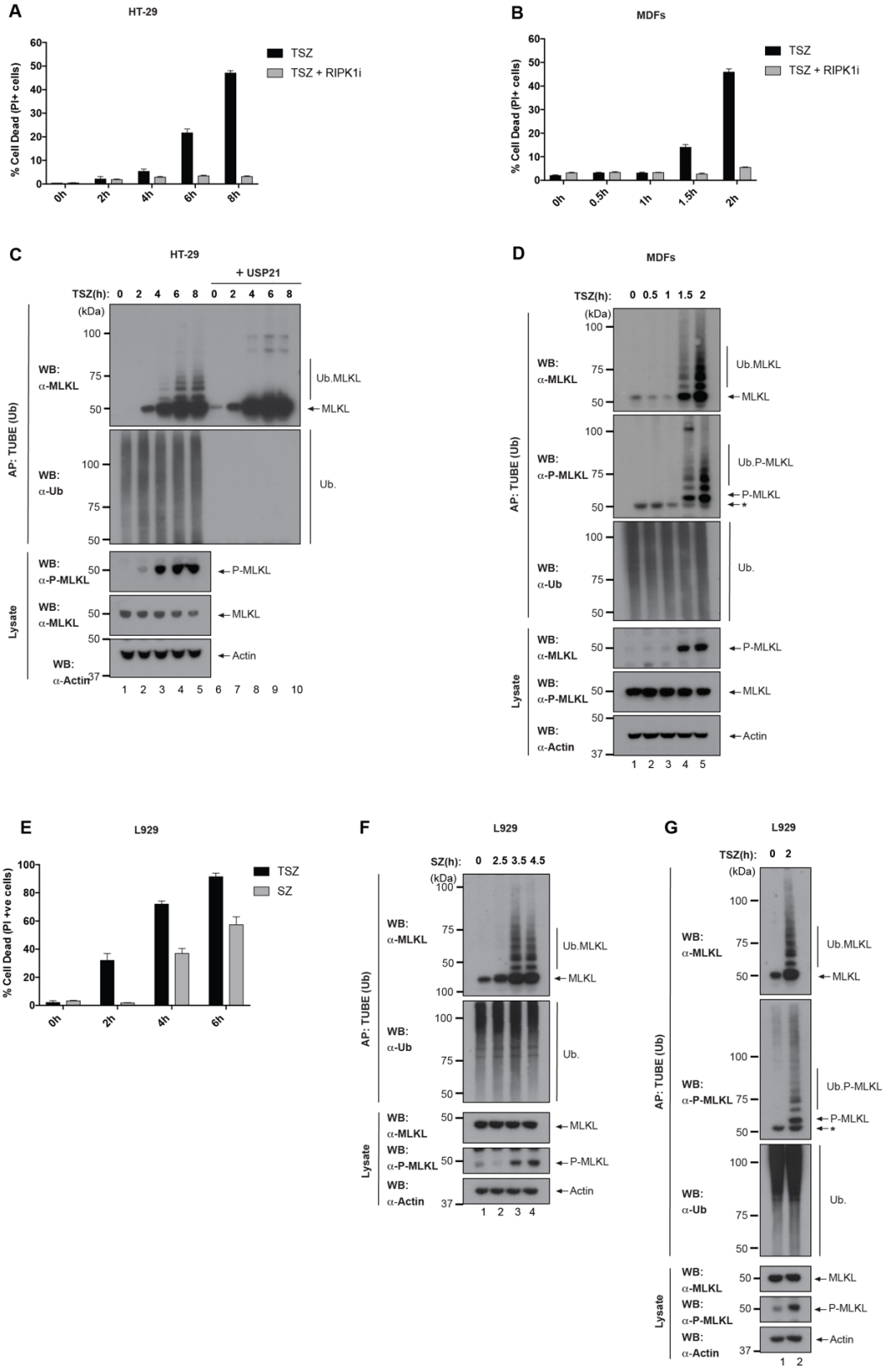

Figure 3.1. Ubiquitylation of MLKL correlates with necroptotic cell death progression.

(A, B, E) Kinetics of cell death in HT-29, MDFs and L929 cells upon TNF-induced necroptosis. (A, B) Quantification of PI+ HT-29 cells and MDFs upon treatment with TNF (T,10 ng/ml), SM-164 (S,100 nM) and z-VAD-fmk (Z,20μM) (TSZ) for the indicated times in the presence or absence of RIPK1i (GSK'963, 100 nM). (E) Quantification of PI+ L929 cells upon treatment with SZ in presence or absence of TNF. **(C, D, F, G)** MLKL is ubiquitylated upon TNF-induced necroptosis. (C) HT-29 cells were treated with TSZ for the indicated times and the ubiquitylated proteins were isolated by TUBE Affinity Purification (AP). Prior to elution from the beads, the samples were split in two and either incubated with 2 μM of USP21 for 1 h or left untreated. The presence of MLKL ubiquitylation was determined by immunoblot analysis of the eluate using α-MLKL antibody. (D) TUBE affinity purification of the lysates from MDFs cells treated for the indicated time-points with TSZ or left untreated. The presence of MLKL ubiquitylation was determined by immunoblot analysis of the eluate using a α-MLKL antibody. Immunoblotting with an anti-P-MLKL antibody shows that P-MLKL is subject to ubiquitylation. (F, G) TUBE pulldown in L929 cells upon treatment with SZ (F) or TSZ (G).

3.1.2. MLKL is ubiquitylated upon TRAIL-Induced necroptosis

In addition to TNF, necroptosis can be triggered following stimulation of other death receptors by cytokines such as TRAIL [201] (described in Section 1.6.1). I next investigated whether MLKL is also ubiquitylated upon TRAIL-induced necroptosis. Cell death induced by TRAIL/S/Z in HT-29 cells can be rescued by cotreatment with hMLKL inhibitor necrosulfanamide (NSA), demonstrating that the necroptotic pathway is engaged by this stimulus **(Figure 3.2A).** NSA blocks necroptosis downstream of MLKL phosphorylation by conjugating to Cys86 and blocking hMLKL aggregation into high order polymers [191]. TRAIL-induced necroptosis also resulted in MLKL ubiquitylation, indicating that MLKL ubiquitylation is not confined to TNF-induced necroptosis, but is a more general phenomenon of MLKL activation and necroptosis **(Figure 3.2B).** Similar to the TNF-setting, the appearance of the Ub smear was concomitant to the detection of P-MLKL.

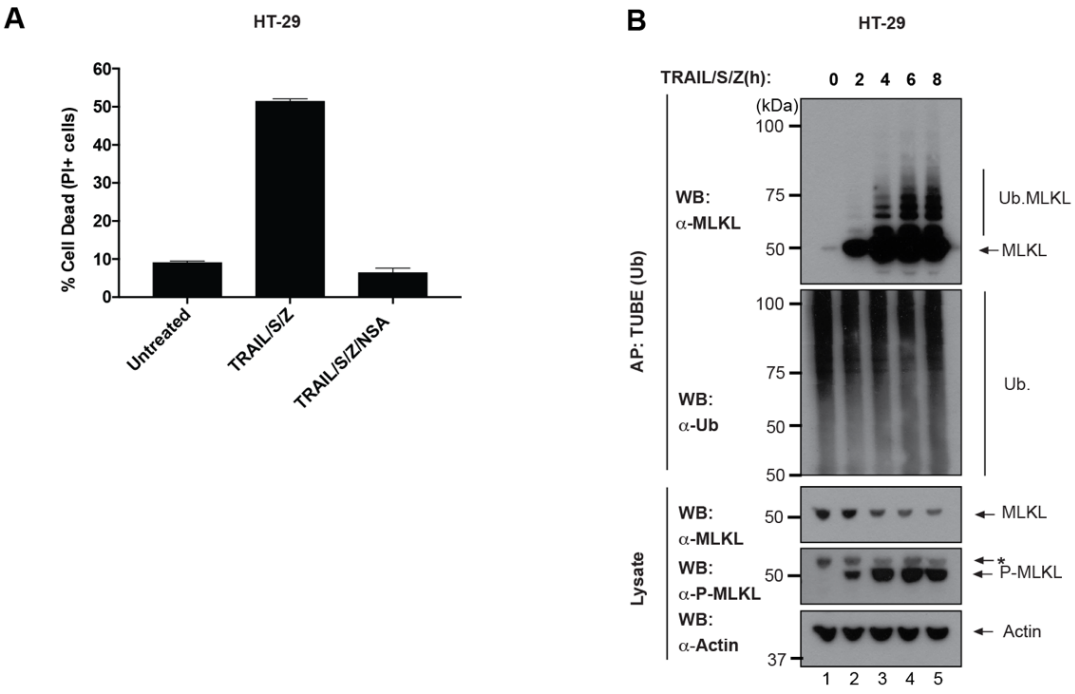

Figure 3.2. MLKL is ubiquitylated upon TRAIL-Induced necroptosis.

(A) TRAIL-induced necroptosis can be rescued by necrosulfanamide (NSA), an inhibitor of hMLKL. Quantification of PI+ HT-29 cells upon treatment with TRAIL (50 ng/ml), SM-164

(100 nM) and zVAD-fmk (20 μM) (TRAIL/S/Z) for 8 h, in the presence or absence of NSA. **(B)** MLKL is ubiquitylated upon TRAIL-induced necroptosis. TUBE pull-down of lysates from HT-29 cells, upon treatment as in A for the indicated timepoints followed by immunoblot analysis of the elute using a α-MLKL antibody.

3.1.3. MLKL ubiquitylation is specific to the necroptotic pathway

To evaluate whether MLKL ubiquitylation occurs during other cell death modalities, such as apoptosis, I treated MDFs with TS (in de absence of Z), which predominantly drives caspase-8-dependent apoptosis. Of note, although MDFs can undergo both cell death modalities, TS-induced cell death generally occurs by apoptosis, which blocks necroptosis **(Figure 3.3A)**. Under these conditions, there were no detectable levels of MLKL phosphorylation or ubiquitylation, demonstrating the specificity of these modifications to the necroptotic pathway **(Figure 3.3B).**

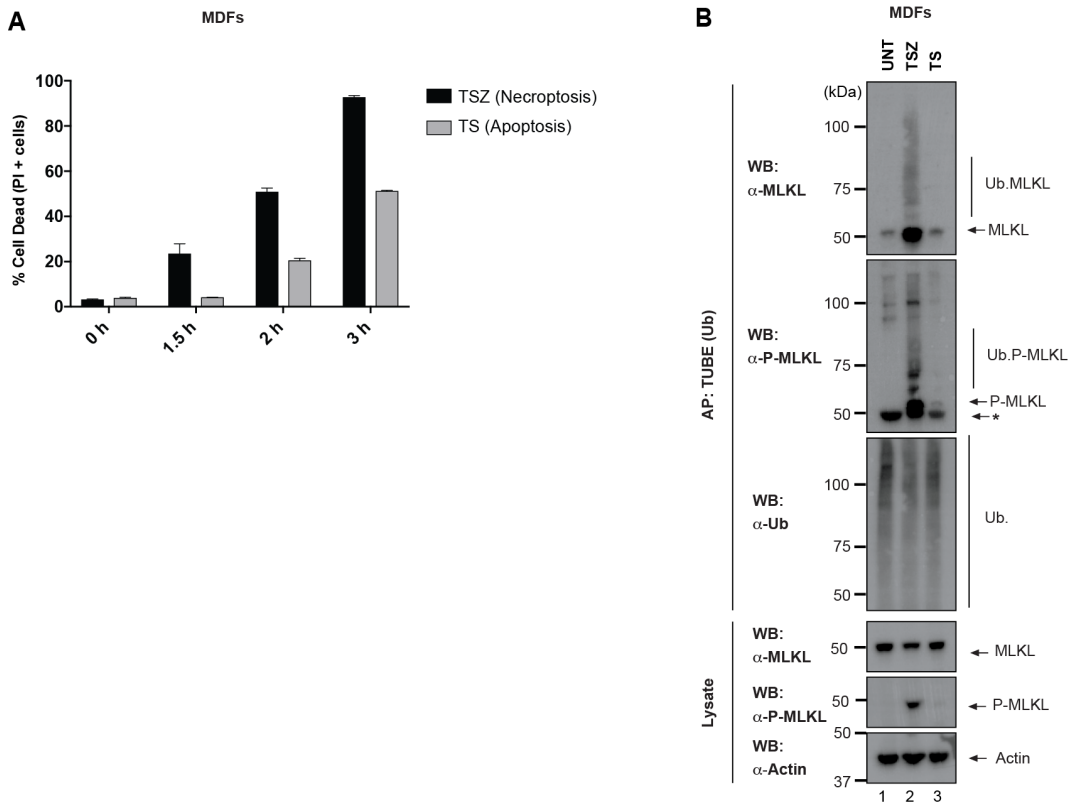

Figure 3.3. MLKL ubiquitylation is specific to the necroptotic pathway.

(A) Comparison of kinetics of cell death in MDFs upon TSZ-induced necroptosis and TS-induced apoptosis. Quantification of PI+ MDF cells upon treatment with TSZ and TS. **(B)** TUBE pull-down of the lysates from MDFs treated with TS for 3 h to induce apoptosis or with TSZ for 2 h to induce necroptosis.

3.2. MLKL is ubiquitylated following phosphorylation by RIPK3

My data indicate that phosphorylation and ubiquitylation of MLKL occur simultaneously during necroptosis. I next determined the epistatic position of the ubiquitylation event. To this end, I generated *Ripk3*$^{-/-}$ MDFs via the CRISPR-Cas9 technology. As expected, *Ripk3*$^{-/-}$ MDFs were unable to undergo necroptosis **(Figure 3.4A)**. Interestingly, MLKL ubiquitylation was abrogated in the absence of RIPK3, demonstrating that MLKL ubiquitylation is dependent on RIPK3 **(Figure 3.4B).** Structural studies support the idea that MLKL is kept in an inactive conformation and undergoes a conformational change following RIPK3-mediated phosphorylation [178]. To further investigate the role of MLKL phosphorylation, I reconstituted *Mlkl*$^{-/-}$ MDFs with a phosphomutant form of MLKL (*Mlkl* ^{S345A}). As previously reported this phospho-mutant form MLKL can no longer be phosphorylated by RIPK3, rendering these cells resistant to necroptosis **(Figure 3.4C)**[184]. Importantly, in these cells MLKL was also no longer ubiquitylated **(Figure 3.4D)**, suggesting that MLKL is ubiquitylated downstream of its phosphorylation by RIPK3. In agreement with this, inactivating the kinase activity of RIPK3 with the RIPK3 kinase inhibitor GSK'843 (RIPK3i) prevented MLKL ubiquitylation **(Figure 3.4E)**. Likewise, genetic depletion of *Ripk1* or pharmacological inhibition of RIPK1 (RIPK1i) also blocked MLKL ubiquitylation **(Figures 3.4E and F)**. Because the phospho-mimetic mutation MLKL^{S345D} is sufficient to induce cell death upon expression in the absence of exogenous stimuli [178], I tested whether MLKL^{S345D} is ubiquitylated. Surprisingly, I found that MLKL^{S345D} is ubiquitylated in the absence of any stimuli, demonstrating that the upstream signalling requirement for MLKL's ubiquitylation can be bypassed by mimicking RIPK3-mediated phosphorylation **(Figure 3.4G)**. These results strongly suggest that ubiquitylation of MLKL occurs downstream of its phosphorylation by RIPK3.

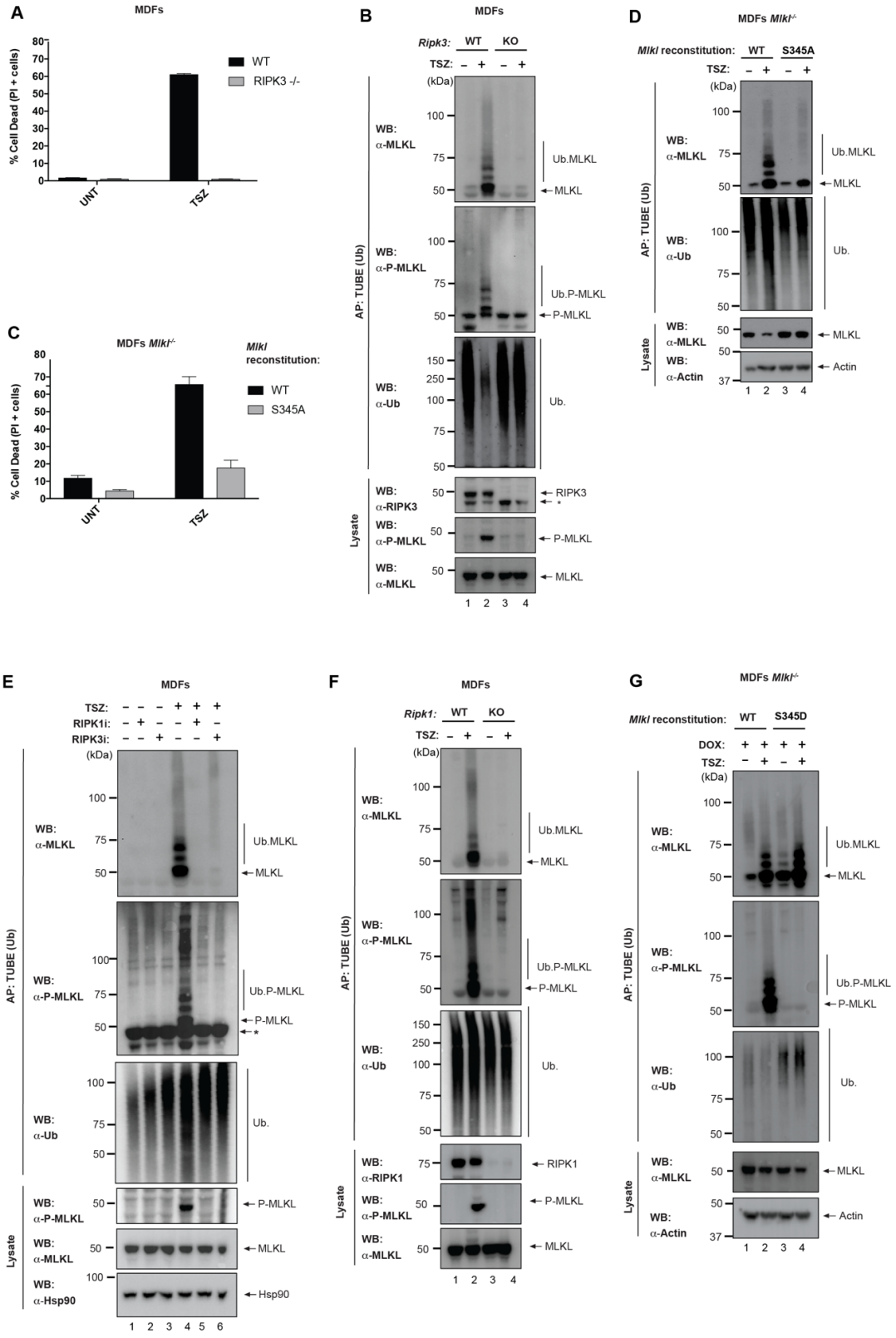

Figure 3.4. MLKL is ubiquitylated following phosphorylation by RIPK3

(A) *Ripk3*$^{-/-}$ cells are resistant to necroptosis. Quantification of PI+ *Ripk3*$^{-/-}$ and WT MDFs cells upon treatment with TNF (10 ng/ml), SM-164 (100 nM) and zVAD-fmk (20 μM) (TSZ) for 2.5 h. **(B)** Lack of *Ripk3* abrogates MLKL ubiquitylation. TUBE affinity purification of the lysates from WT and *Ripk3*$^{-/-}$ MDFs cells treated for 2 h with TSZ or left untreated. **(C)** *Mlkl*$^{-/-}$ MDFs reconstituted with phosphomutant *Mlkl* (S345A) are resistant to necroptosis. Quantification of PI+ *Mlkl*$^{-/-}$ MDFs cells reconstituted with *Mlkl* WT or *Mlkl* S345A following doxycycline treatment (0.5 μg/ml for 3 h) to induce MLKL expression and subsequent treatment TSZ for 2 h. **(D, E)** Lack of RIPK3-mediated phosphorylation compromises MLKL ubiquitylation. (D) TUBE affinity purification of the lysates from *Mlkl* $^{-/-}$ MDFs cells reconstituted with *Mlkl* WT or *Mlkl* S345A following treatment as in C. (E) TUBE pull-down of the lysates from MDFs treated for 2 h with TSZ in the presence or absence of RIPK1i (GSK'963, 100 nM) or RIPK3i (GSK'843,2 μM). **(F)** Lack of *Ripk1* abrogates MLKL ubiquitylation. TUBE pull-down of lysates from WT and *Ripk1*$^{-/-}$ MDFs treated with TSZ (as in A). **(G)** MLKL is ubiquitylated upon MLKL S345D-driven cell death in the absence of necroptotic stimulation. TUBE affinity purification of the lysates from *Mlkl*$^{-/-}$ MDFs reconstituted with *Mlkl*^{WT} or *Mlkl*^{S345D}. Cells were treated with doxycycline alone or followed by treatment with TSZ.

3.3. Oligomerized forms of MLKL are ubiquitylated

Given that MLKL oligomerisation is a crucial event in necroptosis [182], I investigated whether oligomerised MLKL is also ubiquitylated. Previous reports showed that MLKL oligomers are stabilized by intermolecular disulphide bonds that are formed between cysteine residues of different MLKL molecules [188, 191, 193].Oligomerized MLKL can be detected by western blotting under non-reducing conditions [188, 191, 253]. Consistent with the aforementioned reports, I observed that TSZ treatment triggers MLKL oligomerisation **(Figure 3.5A)**. I also found that the oligomeric forms of MLKL are ubiquitylated **(Figure 3.5B)**. Accordingly, incubation with USP21 abrogated the Ub smearing pattern, leading to the appearance of monomeric and oligomeric forms of MLKL **(Figure 3.5C)**. Together, these data indicate that oligomeric, active MLKL is ubiquitylated.

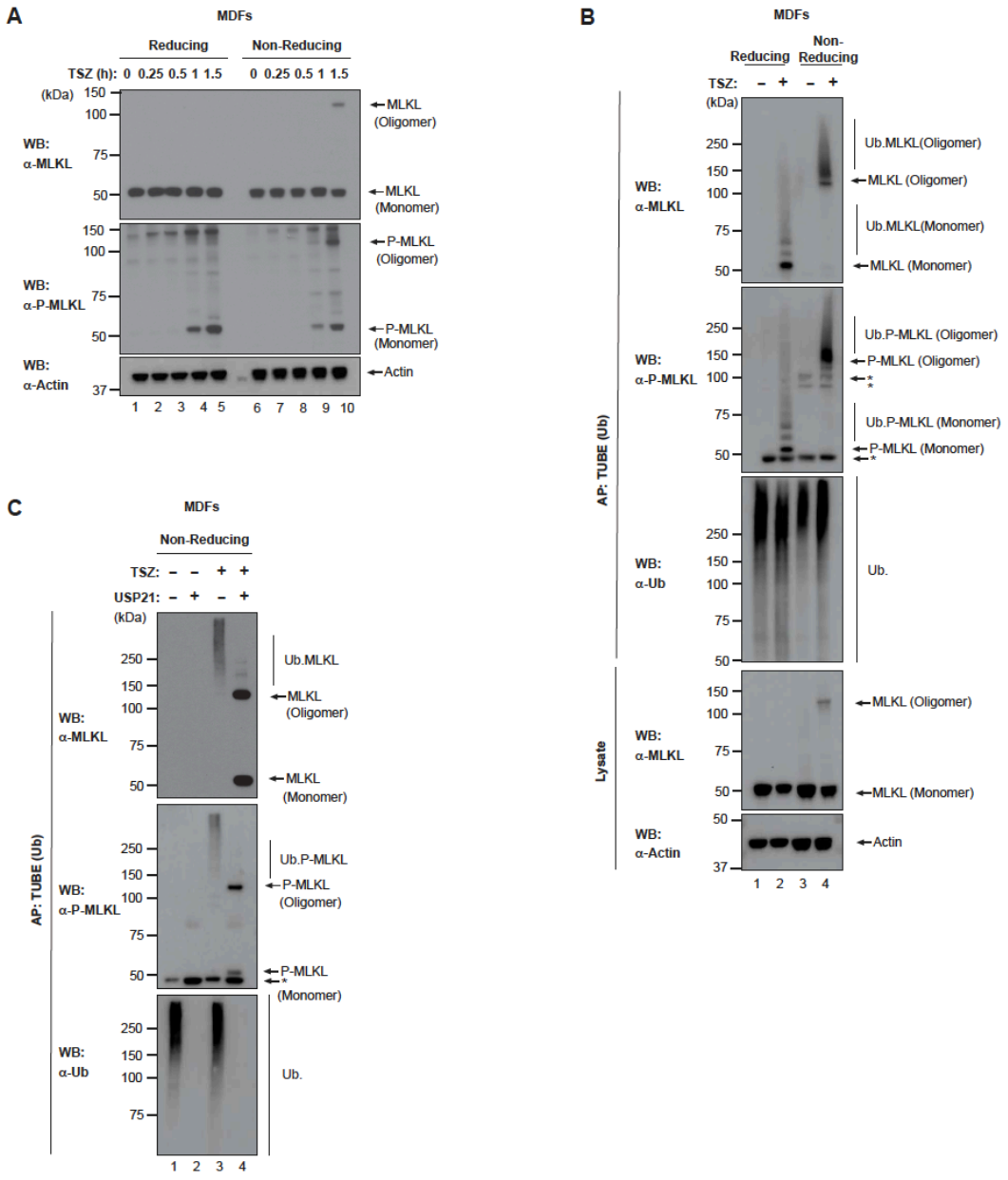

Figure 3.5. Oligomerized forms of MLKL are ubiquitylated

(A) MLKL forms oligomers upon necroptotic stimulation. MDFs were treated with TSZ for the indicated time points. The samples were either mixed with sample buffer containing β-ME (reducing condition) or under non-reducing condition. Oligomerization of MLKL was subsequently visualised by SDS-PAGE followed by immunoblot. **(B, C)** Oligomeric forms of MLKL are ubiquitylated. (B) TUBE AP of the lysates from MDFs treated with TSZ. Following AP, samples were eluted under reducing or non-reducing conditions. (C)TUBE affinity purification of the lysates from MDFs treated with TSZ. Before elution, samples were treated with the USP21 or left untreated. Lysates were eluted in non-reducing conditions to visualize MLKL oligomerization.

3.4. The 4HBD is required for MLKL ubiquitylation

The N-terminal 4HB is crucial for MLKL-mediated cell death [180]. Therefore, I next tested the role of the 4HB for MLKL ubiquitylation. To this end, I generated MDFs that express MLKL that lacks the 4HBD, and evaluated its ubiquitylation status. While *Mlkl*$^{-/-}$ MDFs reconstituted with *Mlkl*$^{\Delta 4HBD}$ (lacking Aa124-Aa464) failed to undergo TNF-induced necroptosis, cells reconstituted with full-length wild-type *Mlkl* (*Mlkl* ^{WT}) readily died by necroptosis, validating such cells **(Figure 3.6A)**. Surprisingly, lack of the 4HB resulted in complete loss of MLKL ubiquitylation. In contrast, phosphorylation of MLKL was unaffected **(Figure 3.6B)**. This result demonstrates that phosphorylation of MLKL occurs independently of its ubiquitylation. Given that the 4HB is required for MLKL ubiquitylation, this might indicate that ubiquitylation occurs within the 4HB. Alternatively, it might be an important domain to recruit the E3 ligase. Of note, I also observed that *Mlkl*$^{\Delta 4HBD}$ readily oligomerised, even in absence of any necroptotic stimulus **(Figure 3.6C,** non-reducing**)**. This demonstrates that 4HBD plays an important role in suppressing the oligomerisation of MLKL under base-line condition. Furthermore, because MLK$^{\Delta 4HBD}$ is not ubiquitylated but still oligomerizes, this indicates that ubiquitylation of MLKL does not contribute to its oligomerisation.

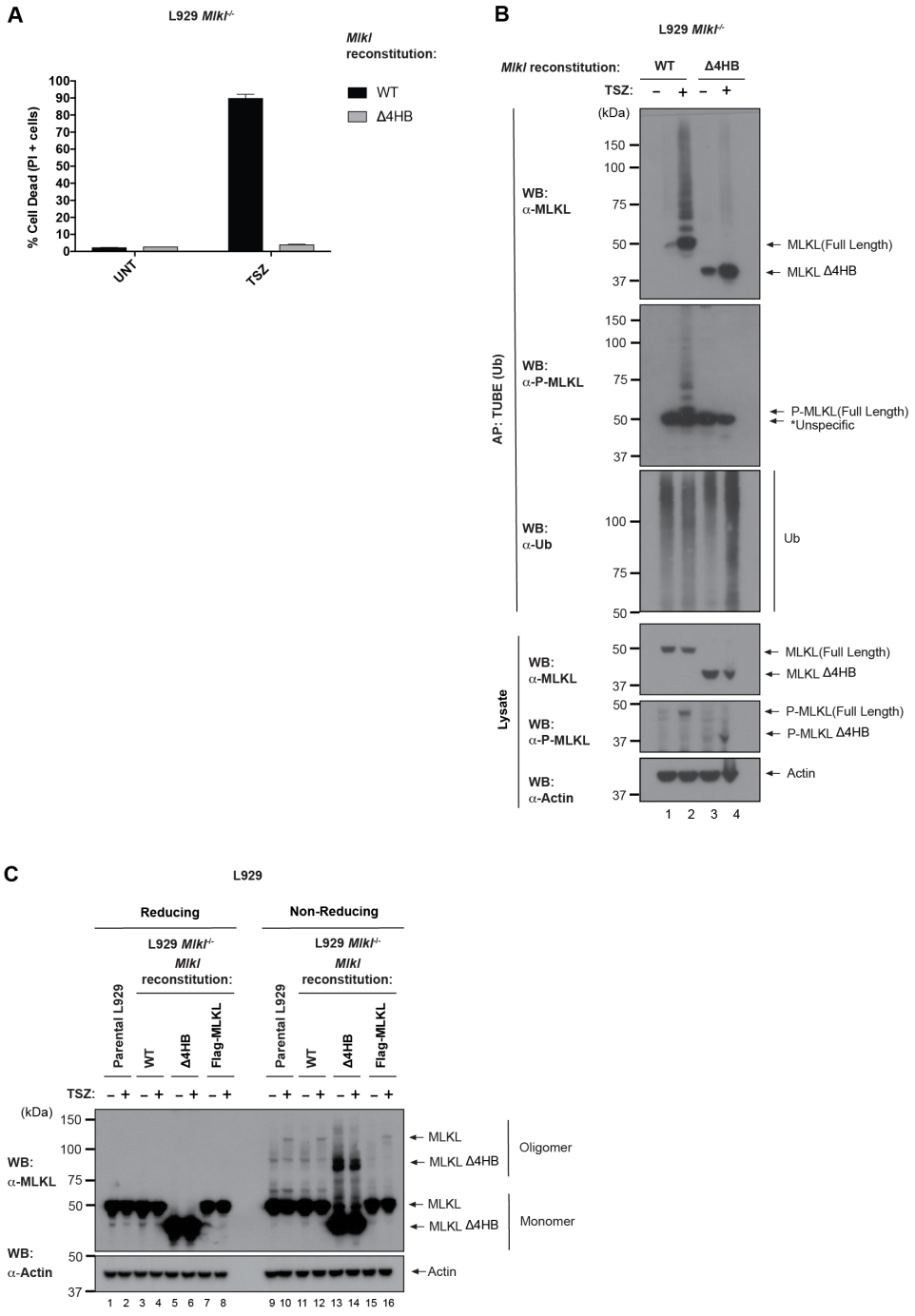

Figure 3.6. The 4HBD of MLKL is required for its ubiquitylation.

(A) The 4HBD is required to induce necroptosis. Quantification of PI+ *Mlkl*$^{-/-}$ MDFs reconstituted with full-length MLKL (WT) or a deletion construct lacking the 4HBD (Δ4HBD). The respective MLKL proteins were induced with the help of doxycycline (0.5 µg/ml for 3 h) and cells were treated with TSZ. **(B)** The 4HBD is required for MLKL ubiquitylation. TUBE affinity purification of the lysates from the indicated MDFs. The respective MLKL proteins

were induced with the help of doxycycline (as in A). Cells were treated with TSZ for 2 h. **(C)** The 4HBD represses MLKL oligomerization under steady state conditions. *Mlkl*$^{-/-}$ L929 cells were reconstituted with full-length MLKL^{WT}, MLKL$^{\Delta 4HBD}$ or N-terminally FLAG-tagged MLKL (MLKL$^{N\text{-}FLAG}$). Following treatment with TSZ (as in C) the samples were run under (1) reducing or (2) non-reducing conditions. MLKL oligomerisation was visualised by western blotting with the indicated antibodies.

3.5. MLKL is ubiquitylated in the cytoplasm before its translocation to the plasma membrane

Following oligomerisation, MLKL translocates to the plasma membrane to induce cell death [170, 189, 193]. To address whether MLKL ubiquitylation occurs before or after plasma membrane localisation, I applied *in situ* proximity ligation assay (PLA). I utilised *Mlkl*$^{-/-}$ MDFs reconstituted with an N-terminal FLAG-tagged *Mlkl* (MLKL$^{N\text{-}FLAG}$). Of note, MLKL$^{N\text{-}FLAG}$ fails to induce cell death because MLKL$^{N\text{-}FLAG}$ fails to assemble into higher order amyloid-like polymers at the plasma membrane [191], a requirement for cell death to ensue. Using primary antibodies against MLKL and Ub, I observed prominent PLA speckles following treatment with TSZ. In contrast, no such speckles were detected under untreated conditions. This result is in line with the data obtained from the TUBE affinity purification. Interestingly, these PLA speckles localised to the cytosol **(Figure 3.7A**), suggesting that MLKL is ubiquitylated in the cytosol prior to its translocation to the plasma membrane. In addition, the fact that MLKL$^{N\text{-}FLAG}$ is ubiquitylated indicates that ubiquitylation occurs prior to the assembly of higher order polymers.

Next I conducted a subcellular fractionation approach to separate the cytosolic content (C) from the membrane-containing fraction (M), as previously conducted for MLKL [177]. In concordance with published literature, MLKL and P-MLKL were detected in the membrane-enriched fraction following exposure to necroptotic stimuli **(Figure 3.7B,** lysate**)**. By performing a Ub pulldown after cellular fractionation, I found that ubiquitylated MLKL was detected in both the cytosolic and membrane-enriched fractions following 2 h treatment with TSZ **(Figure 3.7B,** TUBE AP**)**. Of note, increasing the duration of the treatment to 2.5 h resulted in the accumulation of ubiquitylated MLKL in the membrane-enriched fraction **(Figure 3.7B,** TUBE AP**)**. Together, these results support the notion that MLKL is ubiquitylated in the cytosolic compartment, before its translocation to the plasma membrane.

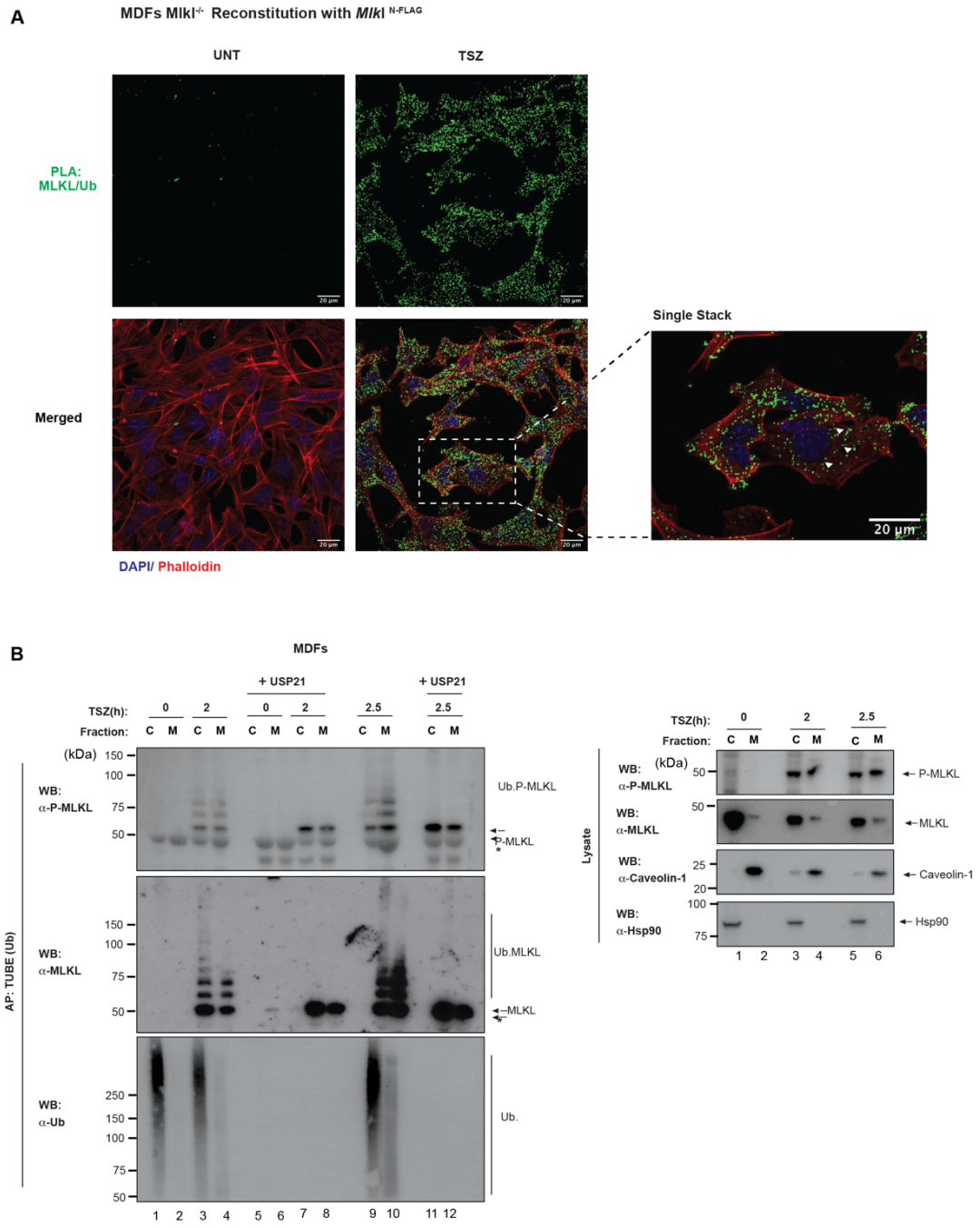

Figure 3.7. MLKL is ubiquitylated in the cytoplasm before its translocation to the plasma membrane.

(A) MLKL ubiquitylation occurs in the cytoplasm. Proximity Ligation Assay (PLA) with anti-MLKL and anti-Ub antibodies using *Mlkl*$^{-/-}$ MDFs reconstituted with MLKL$^{N\text{-}FLAG}$. Cells were pre-treated with doxycycline followed by treatment with TSZ for 2 h, fixed, permeabilized, blocked with 5 % BSA and incubated with anti-MLKL and anti-Ub antibodies overnight at 4 C. DNA was stained with DAPI and actin filaments with phalloidin. The green speckles (PLA: MLKL/Ub) depict the proximal localization of MLKL and Ub. Magnification is showing a single

stack to visualize the localization of the speckles in the cytoplasm. This PLA experiment was performed in collaboration with Gianmaria Liccardi of the Meier Lab. **(B)** Ubiquitylated MLKL translocates to the plasma membrane fraction as necroptosis progresses. MDFs were treated with TSZ for 2 and 2.5 h, and subjected to cellular fractionation as described in materials and methods (Section 2.9.2.1). The corresponding cytoplasmic (C) and membrane (M) fractions were subjected to a TUBE pull-down. Prior to elution from the beads, samples were split and left untreated or digested with USP21.

3.6. MLKL is ubiquitylated with K63-linked polyUb chains

I next determined the Ub linkage types that are conjugated to MLKL. To this end I utilized high-affinity polyUb-binding proteins to purify specific Ub linkage types. For K63-linked chains I used an engineered form of a K63-specific tandem UIMs [250] fused to Glutatione-S-transferase (GST) (K63-UIM). To isolate M1-linked polyUb chains I used the UBAN domain of human NEMO (residues 257-346) fused to GST (M1-SUB) [254], and for K48-linked polyUb chains I used an anti-K48-linkage specific antibody. As controls, I either used an UIM with a mutation that abrogates Ub-binding (UIM mutant, for K63- chains), a GST control (for M1-chains) or an IgG control (for K48 chains). As shown in **Figure 3.8A**, TNF-induced necroptosis triggered prominent K63-linked ubiquitylation of MLKL in MDFs. In contrast, M1- or K48-linked MLKL ubiquitylation were not detected under this condition **(Figures 3.8A)**. Likewise, the presence of K63-linked Ub chains were also identified in human HT-29 cells **(Figures 3.8B).**

To further characterize the Ub linkage types that are conjugated to MLKL, I conducted several attempts using the Ub Chain Restriction Analysis (UbiCrest) [255]. To this end, the digestion with several enzymes was carried out following a TUBE pulldown. Unfortunately, these results were inconclusive due the fact that the TUBE reagent shielded the Ub chains, preventing them from being deubiquitylated by the DUBs.

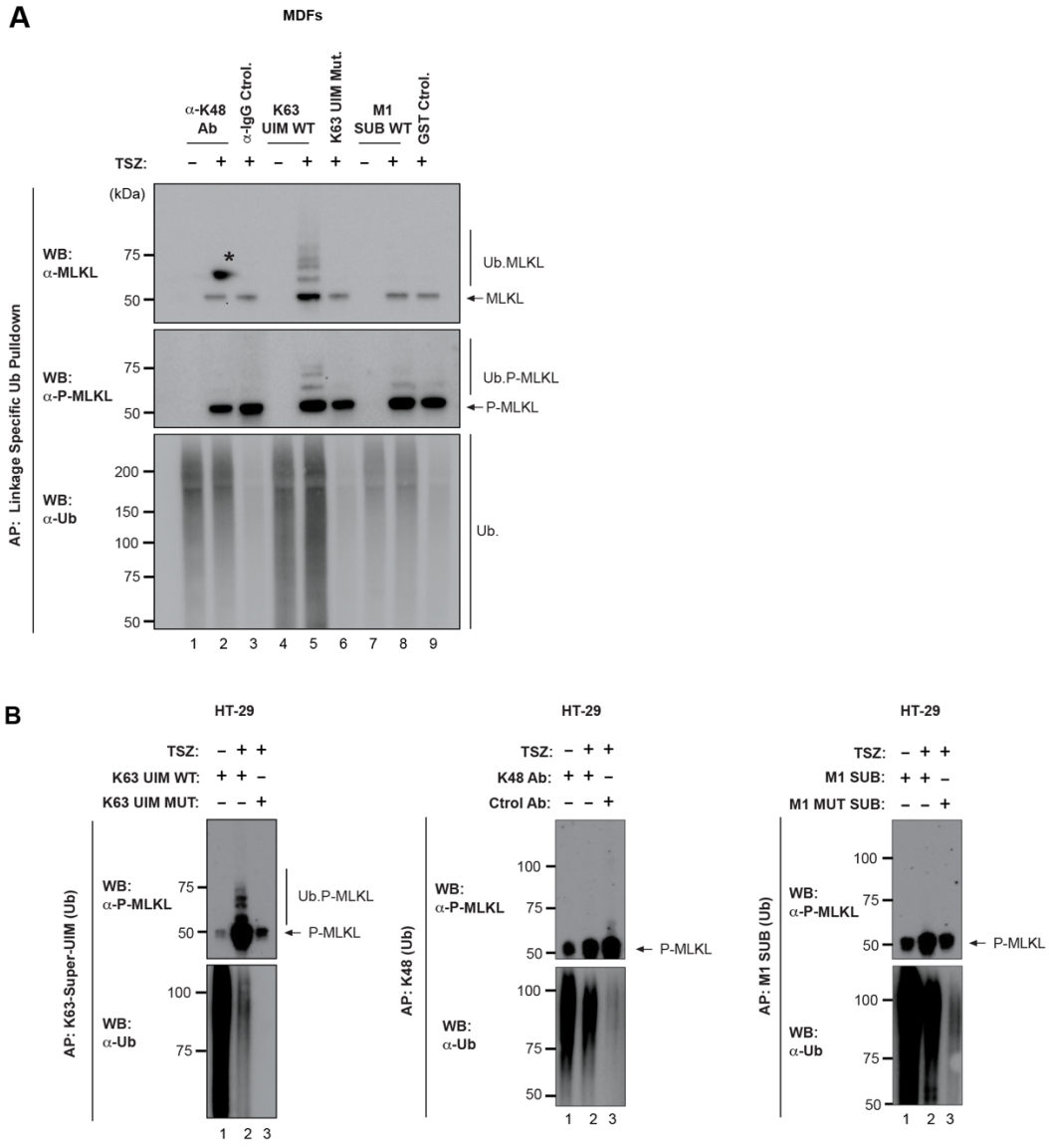

Figure 3.8. MLKL is ubiquitylated with K63-linked polyUb chains.

(A, B) MLKL is ubiquitylated with K63-linked polyUb chains in MDFs and HT-29 cells. In contrast, neither M1- or K48-linked polyUb chains were detected under these conditions. Affinity purification of the lysates from MDFs (A) or HT-29 (B) treated with TSZ for 2 h or 6 h, respectively. To identify K48-linked polyUb chains, lysates were subjected to a pulldown with α-K48 Ub-chain specific antibodies. K63-linked and M1-linked polyUb chains were purified with K63-Super-UIM and M1-SUB, respectively. Precipitates were examined by western blotting using the indicated antibodies. The MDF experiment was performed in collaboration with Sidonie Wicky John of the Meier Lab. Data shown is representative of n≥2 biological replicates.

3.7. Mass spectrometry-based identification of Ub acceptor sites of mMLKL

To identify the function of MLKL ubiquitylation, I next identified K residues of MLKL that are conjugated to Ub following TNF-induced necroptosis. To this end, I used a quantitative mass spectrometry-based approach. Briefly, MDFs were treated with TSZ, or left untreated. Cells were lysed and proteins digested with trypsin. Ubiquitylated peptides bearing the di-glycine (di-Gly, K-GG) remnant were enriched by immunoprecipitation with an anti-K-ε-GG antibody. I prepared a total of three biological replicates. The 6 samples were labelled with Tandem Mass Tags (TMT). Samples were mixed and analysing by Liquid Chromatography-Tandem Mass Spectroscopy (LC-MS/MS). Quantification was performed to determine the relative abundance of site-specific ubiquitylation events in each condition **(Figure 3.9A).**

I used the Volcano plot analysis tool to visualise the abundance of identified K-GG peptides of the three replicates **(Figure 3.9B).** Comparing TSZ-treated cells to untreated controls, I observed 96 unique di-Gly peptides with significantly different relative abundance. Of note, I discovered increased abundance in site-specific ubiquitylation for several proteins of the TNFR1 signalling pathway, including RIPK1, RIPK3, Casp8, and MLKL upon treatment with TSZ **(Figures 3.9B)** peptides above the curve on the right**).**

Examination of the K-GG peptides for MLKL revealed enrichment of four ubiquitylated K: K51, K77, K172 and K219. The identified K residues of MLKL were located in the three regions of MLKL: (1) the 4HBD (K51 and K77), (2) the brace helix (K172) and (3) the pseudokinase domain (K219). Importantly, the four sites were specifically enriched upon treatment with TSZ in all three biological replicates **(Figures 3.9C,** right graph**).**

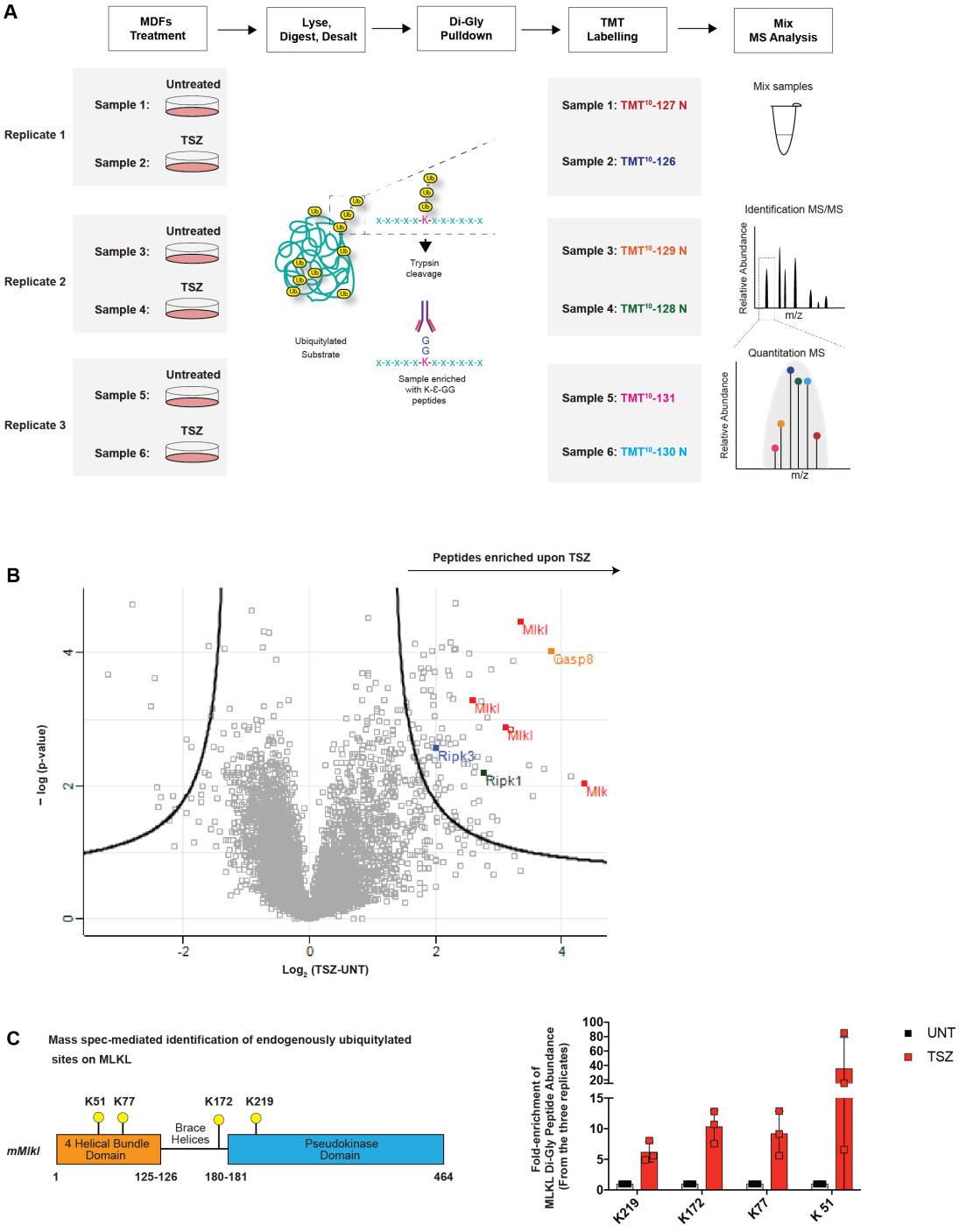

Figure 3.9. Endogenous MLKL is ubiquitylated at K51, K77, K172 and K219.

(A) Scheme of the experimental design to identify ubiquitylated sites during necroptosis. MDFs were treated with TSZ for 2 h, or left untreated. After trypsin digestion, Ub remnants were enriched using an anti-K-ε-GG antibody. Six samples, corresponding to three biological replicates, were labelled with one of the TMT 10-plex tags. Subsequently, samples were mixed, subjected to identification by LC-MS/MS and quantified using peak area under curve.

(B) Identification of four ubiquitylated K in mMLKL upon TSZ-induced necroptosis. Volcano plot of global peptide abundance showing -Log p-values versus log2 ratio changes between TSZ (2 h) and untreated control. The three biological replicates are taken into consideration. Each peptide is represented with a dot and those peptides corresponding to MLKL, RIPK1, RIPK3 and Caspase-8 are indicated in the graph. **(C)** Schematic representation showing the domain localization of the identified ubiquitylated K residues on MLKL (left) and the fold-enrichment upon TSZ for each di-Gly peptide abundance (right). Error bars indicate SD. Dr. Lu Yu performed the LC-MS/MS experiment, including the identification of the di-Gly peptides and the quantification of peptide abundance.

3.8. Role of MLKL ubiquitylation

3.8.1. MLKL ubiquitylation at K219 enhances cell death

The mass spec data indicate that MLKL is ubiquitylated in the 4HBD (K51 and K77), in the second brace helix (K172) and within the pseudokinase domain (K219). Excitingly, K219 is involved in MLKL activation [178]. K219 forms a hydrogen bond with Q343, which is located in the activation loop helix **(Figure 3.10A)** [178]. Interference with this hydrogen bond, for example by mutating K219 to methionine (K219M), results in a constitutively active form of MLKL, even in the absence of necroptotic stimuli and independently of RIPK3 activity [178]. Consequently, it was postulated that disruption of this hydrogen bond of the pseudoactive site of mMLKL causes a conformational change that leads to mMLKL activation. Accordingly, phosphorylation at S345 by RIPK3 occurs in close proximity to Q343. This in turn can destabilise the hydrogen bond, causing a rearrangements of the pseudoactive site, which leads to MLKL activation. Since MLKL is ubiquitylated at K219, and this residue is critical for MLKL activation, I hypothesized that this modification might influence mMLKL activation.

Next, I used PyMOL software to predict whether mutating K219 to R would influence the hydrogen bond with Q343. If that was not the case then this mutant would enable me to test the role of MLKL ubiquitylation without interfering with MLKL's inactive state. As expected, mutating K219 to M (K219M) seemed to abrogate the formation of the hydrogen bond between M219 and Q343, presumably due to a shorter side chain. In contrast, mutation to arginine (K219R), which has a chemical structure more similar to a K, was predicted to maintain the hydrogen bond interaction as seen under wild-type settings **(Figure 3.10B)**. To functionally test this prediction, I mutated K219 residue to M (*Mlkl*^{K219M}) and R (*Mlkl*^{K219R}) and analysed the ability of these mutants to induce cell death upon expression in *Mlkl*$^{-/-}$ MDFs. As previously reported [178], mere expression of MLK^{K219M} was sufficient to induce spontaneous necroptotic cell death. In contrast, induced expression of MLKL^{K219R} did not cause cell death despite being expressed to similar levels as MLKL^{K219M} **(Figures 3.10C and D)**.

This result suggests that MLKL^{K219R} behaves as MLKL^{WT} and thus is likely that a hydrogen bond is established between R219 and Q343. Therefore, I decided to use the MLKL^{K219R} mutant to study the role of MLKL ubiquitylation at K219 during necroptosis.

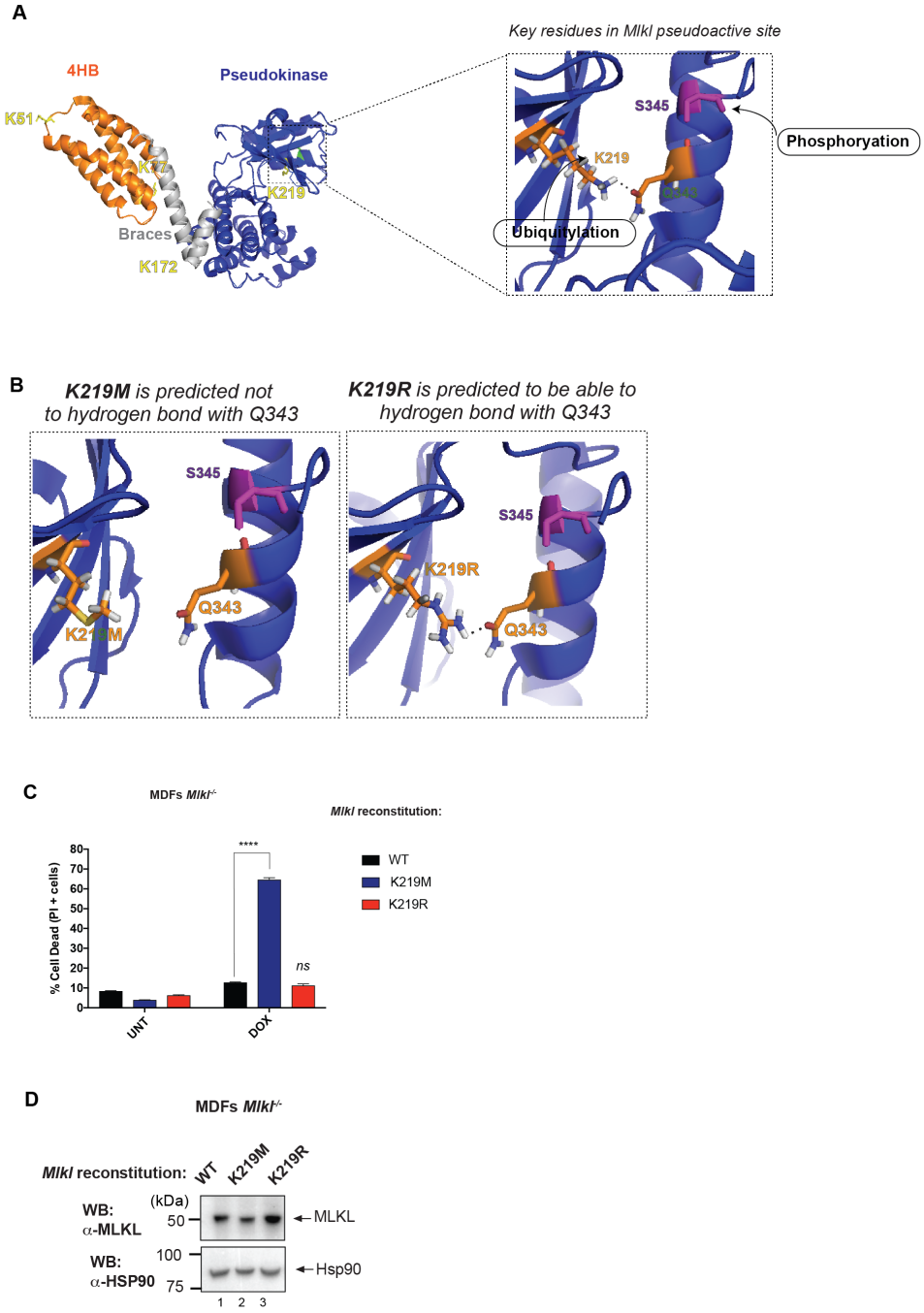

Figure 3.10. MLKL^{K219R} behaves as MLKL^{WT} in its ability to regulate cell death under steady state conditions.

(A) Crystal structure of mMLKL (PBD: 4BTF [178]) comprising the 4HBD (orange), the brace helices (grey) and the pseudokinase domain (blue). The identified ubiquitylated K are shown in yellow. Magnification of the pseudoactive site of MLKL showing the hydrogen bond interaction between K219 and Q343, which is important in keeping MLKL in an inactive conformation. Residue S345 which is phosphorylated by RIPK3 is shown in magenta. **(B)** Predicted effect on the hydrogen bond formation after mutation of K219 to M (K219M, left panel) and to R (K219R, right panel). Predictions were made with Pymol Software. The side chains of K219, R219, M219 and Q343 residues are represented as sticks and coloured by atom type (carbon atoms in orange, nitrogen atoms in blue, oxygen atoms in red and hydrogen atoms in grey). **(C, D)** $MLKL^{K219M}$ is constitutively active whereas $Mlkl^{K219R}$ behaves has $MLKL^{WT}$ under steady-state conditions (absent of necroptotic stimuli). (C) $Mlkl^{-/-}$ MDFs were reconstituted with $Mlkl^{K219M}$ and $Mlkl^{K219R}$ mutants. Expression of the constructs was induced with doxycycline (0.5 µg/ml for 5 h) and cell death was measured by FACS analysis, scoring PI+ cells. Graphs show mean ± SD, n=2 independent biological repeats. Data was analysed by two-way ANOVA ***p <0.001, non-statistically significant (*ns*). (D) $MLKL^{K219M}$ and $MLKL^{K219R}$ mutants are expressed to similar extent. $Mlkl^{-/-}$ MDFs reconstituted and treated as in C were immunoblotted with the indicated antibodies.

I next evaluated the ability of $MLKL^{K219R}$ to drive TNF-induced necroptosis. While $MLKL^{K219R}$ was expressed to similar levels as $MLKL^{WT}$, $MLKL^{K219R}$ was significantly less potent in driving necroptosis than $MLKL^{WT}$, suggesting a pro-death role for ubiquitylation at K219 **(Figures 3.11A and B).**

The mass spec data indicate that MLKL is also ubiquitylated in the 4HBD (K51 and K77) and in the second brace helix (K172). To examine whether ubiquitylation of K51, K77 and K172 influenced the cytotoxic potential of MLKL, I reconstituted $Mlkl^{-/-}$ MDFs with either single K mutants or a combination of multiple Ks. I found that mutating K51 and K77, which are located in the 4HBD ($MLKL^{K51R, K77R}$), had no effect in MLKL's killing potential, neither alone nor in combination, despite similar levels of MLKL expression as $MLKL^{WT}$ **(Figures 3.11A and B)**. Addition of the K219R mutation ($MLKL^{K51R, K77R, K219R}$), reduced the ability of MLKL to kill in comparison to $MLKL^{WT}$. The protection of $MLKL^{K51R, K77R, K219R}$ mutant was the same as $MLKL^{K219R}$. In comparison to the K mutations in the 4HB, mutating K172 of the brace ($MLKL^{K172R}$) showed a modest protection. This may indicate that ubiquitylation of the brace may contribute to

suppressing MLKL's cytotoxic potential **(Figures 3.11A and B).** Nevertheless, my data indicate that ubiquitylation on K219 is the main residue that influences necroptosis.

Following phosphorylation, MLKL is known to translocate to the plasma membrane where it forms higher order polymers [180], ultimately leading to cell death. To examine whether $MLKL^{K219R}$ has lower propensity to form polymers at the plasma membrane, I performed Blue Native PAGE (BN-PAGE) on the cytosolic and membrane fractions following TSZ-induced necroptosis. Consistent with previous reports [180, 181], $MLKL^{WT}$ formed polymers (~400 KDa) in the membrane fraction. In contrast, $MLKL^{K219R}$ had reduced ability to form such polymers, even though MLKL was phosphorylated in the membrane fraction **(Figure 3.11C).** Together, these data suggest that ubiquitylation of K219 enhances the killing potential of MLKL by allowing the formation of higher order oligomers at the plasma membrane.

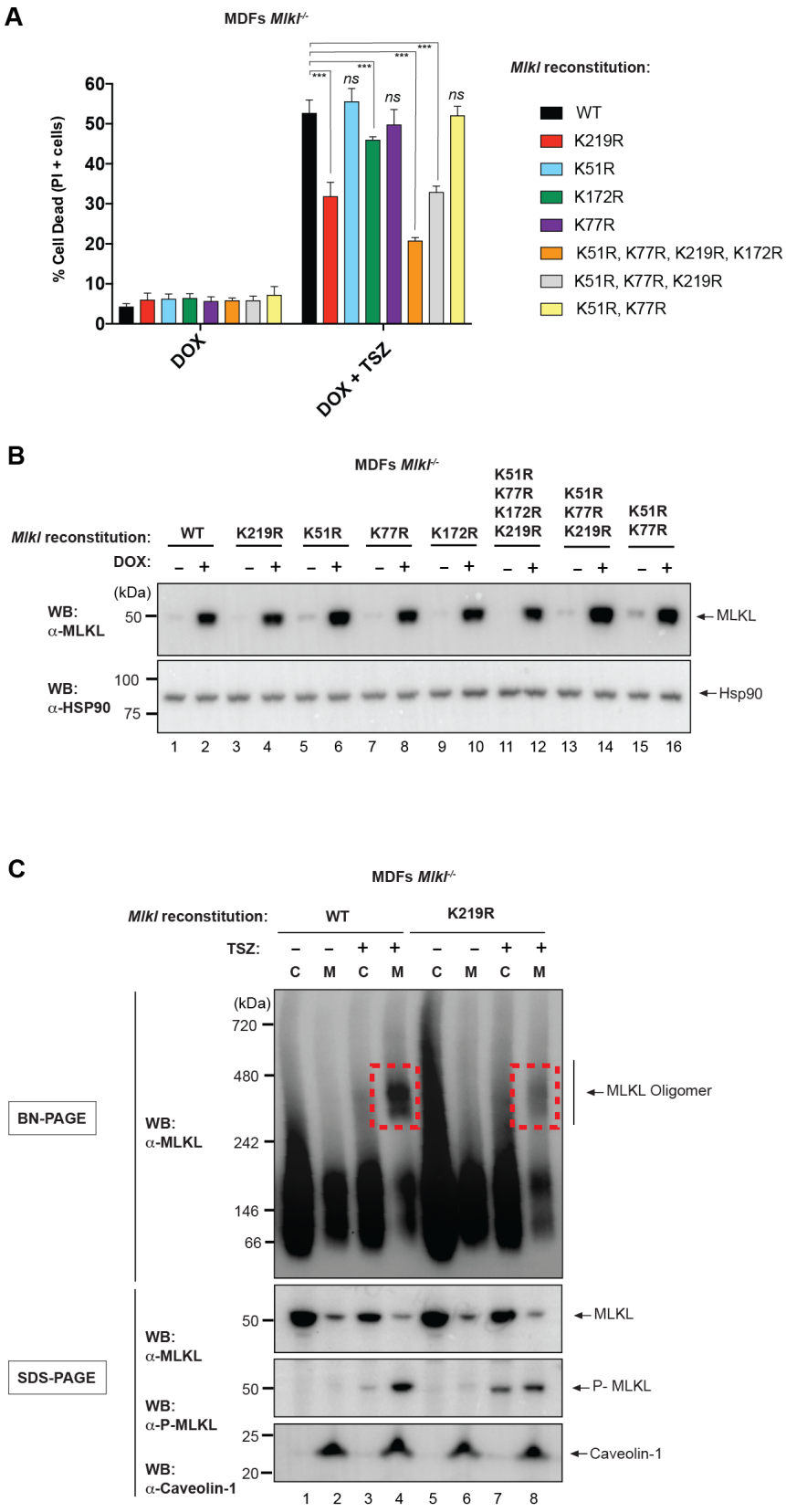

Figure 3.11. Ubiquitylation at K219 enhances the killing potential of MLKL.

(A, B) MLKL^{K219R} protects from TNF-induced necroptosis. (A) *Mlkl*$^{-/-}$ MDFs were reconstituted with the indicated MLKL mutants. The indicated Ub acceptor K were mutated on their own or in combination (K>R). After doxycycline-induced expression of MLKL, cells were stimulated with TSZ for 2 h and cell death was measured by FACS using PI+ staining. Data are presented as means ± SD collated from three experiments and analysed in GraphPad Prism 7 with statistical test by two-way ANOVA. ***p <0.001, non-statistically significant (ns). (B) Immunoblot with the indicated antibodies. **(C)** MLKL^{K219R} has reduced ability to form higher order polymers at the plasma membrane. BN-PAGE analysis shows that MLKL^{WT} translocates from the cytosolic fraction (C) to the membrane (M) fraction where it forms higher order oligomers following TSZ treatment. In contrast, MLKL^{K219R} had a lower propensity to form polymers at the plasma. Nevertheless, WT and the K219R mutant form of MLKL were phosphorylated to similar extent by RIPK3. Data are representative of n=2 independent biological repeats.

My data indicate that following RIPK3-mediated phosphorylation, MLKL is ubiquitylated at K219, which enhances polymer formation and cell death. Next, I determined the role of K219 in a constitutively active phospho-mimetic mutant form of MLKL. Mutating K219 to R suppressed the killing potential of MLKL^{S345D}. This supports the hypothesis that both, phosphorylation and ubiquitylation contribute to the killing potential of MLKL **(Figure 3.12A and B).**

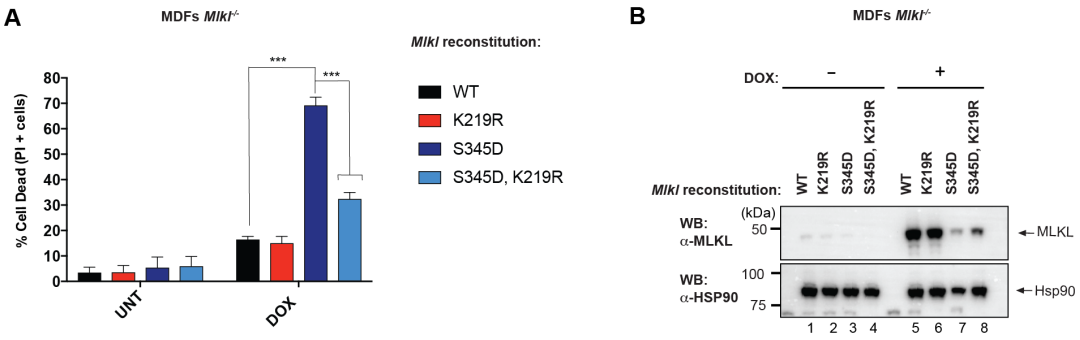

Figure 3.12. MLKL S345D-driven cell death is compromised by K219R mutation.

(A, B) K219R mutation diminishes S345D-driven cell death. (A) Quantification of PI+ *Mlkl*$^{-/-}$ MDFs, reconstituted with the indicated MLKL mutants upon doxycycline treatment (0.5 µg/ml for 5 h). Data are presented as means ± SD collated from two experiments and analysed in GraphPad Prism 7 with statistical test by two-way ANOVA. ***p <0.001. (B) Western blot analysis of total lysates from *Mlkl* $^{-/-}$ MDFs reconstituted with the indicated MLKL mutants upon treatment as in B.

3.8.2. ATP binding is not required for MLKL's killing activity

K219 of MLKL corresponds to the *β3* K residue that is important for the catalytic activity of protein kinases [256] (K in the 'VAIK' consensus motif). Although MLKL is a pseudokinase and lacks catalytic activity, it has retained a K at this position. What is more, K219 appears to be evolutionary conserved among MLKL orthologs (**Figure 3.13A)**. The remaining two conserved catalytic residues crucial for phosphoryl-transfer activity are absent in MLKL.

Although MLKL is catalytically inactive, it still can bind ATP in the conventional ATP-binding cleft between the pseudokinase domain N- and C-lobes. K219 thereby plays an essential role for ATP binding [178]. The fact that K219M mutant cannot bind ATP [178] but is constitutively active, suggests that ATP does not play a role in MLKL activation. Nevertheless, the K219M mutation is directly affecting the hydrogen bond formation with Q343, and, therefore, the role of ATP-binding would be best addressed by using a mutant that does not affect the hydrogen bond. Therefore, I decided to mutate T217 to F (T217F) or tryptophan (T217W). Such changes introduce bulky residues into the ATP-binding pocket, which are predicted to affect ATP-binding. T217 was chosen based on analogous residues in KSR1 and PKA, which when mutated disrupt ATP binding **(Figure 3.13B-D)** [257].

Intriguingly, I found that $MLKL^{T217F}$ and $MLKL^{T217W}$ were capable of inducing cell death to the same extent as $MLKL^{WT}$ **(Figure 3.13E).** Additionally, lack of ATP binding did not have any effect on RIPK3-mediated phosphorylation of MLKL **(Figure 3.13F).** This indicates that ATP-binding is dispensable for mMLKL killing function. Altogether, this result rules out the possibility that the phenotype observed in K219R is due to a lack in ATP binding. Experiments to address the binding of ATP by the $MLKL^{K217F}$ and $MLKL^{K217W}$ mutants are currently ongoing. This work is conducted in collaboration with Prof. James Murphy.

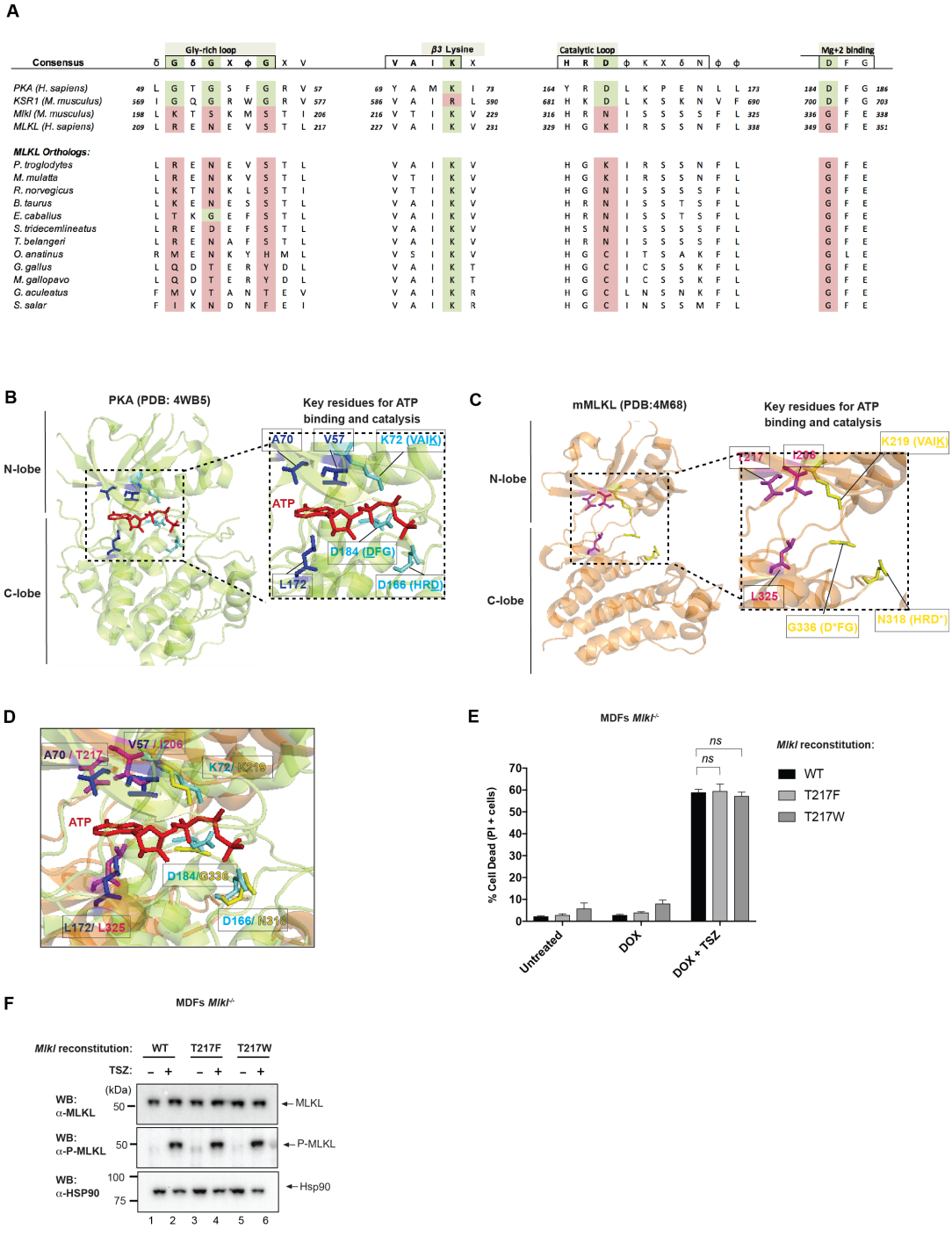

Figure 3.13. ATP binding does not play a role in mouse MLKL activation.

(A) Sequence alignment of Protein Kinase A (PKA), the pseudokinase Kinase Suppressor of Ras 1 (KSR1) and MLKL orthologs. Consensus sequence of the catalytic motifs are depicted as described previously [256, 258] (φ, large hydrophobic; δ, hydrophilic; X any amino acid). The Glycine (Gly)-rich loop or G-loop as well as the VAIK, HRD and DFG motifs are boxed. The key residues required for catalytic activity are shaded in green if conserved, or in red if they differ from the consensus. **(B)** 3D structure of human PKA (PDB: 4WB5) (catalytic alpha subunit) [259] used as a model serine /threonine protein kinase. Magnification of the active site of PKA highlighting key amino acids around the ATP-binding site. Amino acids are shown in stick representation with a colouring scheme. In light blue are represented those amino acids that belong to any of the three conserved motifs: (1) the *β3* K or K in the 'VAIK' motif), (2) the catalytic aspartate (D in 'HRD'; motif) and the cation-binding asparte (D in 'DFG' motif). In dark blue are represented three key conserved residues, which are involved in the assembly of the catalytic spine (C-spine), an hydrophobic spine that defines active protein kinase conformation [163].Two of these residues belong to the *β2 and β3* strands within the N-lobe (V57 and A70, respectively), whereas the third residue is located in the *β7* strand of the C-lobe (L172). ATP is displayed in red. **(C)** 3D structure of mouse MLKL (PDB: 4M68). Magnification of the pseudoactive site of MLKL highlighting the correspondent residues described in B. Residues from the conserved motifs are shown in yellow and residues involved in C-spine assembly are shown in pink. **(D)** The pseudoactive site of MLKL (as in C) was aligned with key residues from the active site of PKA (as in B). PKA is shown in green and MLKL is shown in orange. The structures and 3D alignment were generated using PyMol Software. **(E, F)** Predicted ATP binding deficient MLKL can still engage necroptosis. (E) *Mlkl*$^{-/-}$ MDFs cells were reconstituted with the indicated MLKL ATP-binding mutants. Expression of the constructs was induced with doxycycline (0.5 μg/ml for 3 h) followed by treatment with TSZ. Cell death was measured by quantification of PI+ cells. Data are presented as means ± SD collated from three biological repeats and analysed in GraphPad Prism 7 with statistical test by two-way ANOVA. (F) Cells were treated as in (E) and lysates were subject to immunoblot analysis with the indicated antibodies.

3.8.3. Phosphorylation of MLKL is indispensable for activation

Since K219 plays important role in MLKL activation, I addressed whether ubiquitylation of this residue may trigger MLKL activation, independently of its phosphorylation by RIPK3. Nonetheless, my previous observations **(Figure 3.4)** suggested that ubiquitylation of MLKL required RIPK3-mediated phosphorylation. This led me to hypothesize that an initial pool of P-MLKL may nucleate the recruitment of additional, unphosphorylated MLKL molecules, which could then be activated via Ub-mediated disruption of the hydrogen bond. According to this scenario, ubiquitylation of MLKL may amplify the death signal by directly inducing MLKL activation of unphosphorylated MLKL **(Figure 3.14A)**.

To test this hypothesis, I introduced a phosphomutant, FLAG-tagged form of MLKL (*S345A, T349A-Mlkl*) into cells that harbour endogenous WT MLKL. I reasoned that endogenous MLKL would act as a 'seed' to bind and recruit MLKL$^{S345A,\ T349\text{-}FLAG}$. I then could test whether phosphorylation of endogenous MLKL (non-tagged) would allow the ubiquitylation of the phosphomutant form of MLKL. As a control, I introduced a FLAG-tagged WT form of *Mlkl* into WT MDFs. The tester-transgenes were C-terminally FLAG tagged to be able to distinguish them from endogenous MLKL. As an additional control, the aforementioned constructs were also reconstituted into *Mlkl*$^{-/-}$ MDFs. Treatment of WT MDFs with TSZ revealed that the presence of *Mlkl*$^{WT\text{-}FLAG}$ caused enhanced cell death **(Figure 3.14B)**. In contrast, expression of the phosphomutant MLKL$^{S345A,T349\text{-}FLAG}$ did not show any additive effect in cell death **(Figure 3.14B).** Both *Mlkl*$^{WT\text{-}FLAG}$ and MLKL$^{S345A,T349\text{-}FLAG}$ were expressed to similar extent **(Figure 3.14C).** Together, this experiment discards the 'seeding' hypothesis and suggests that MLKL must be phosphorylated by RIPK3 to become active.

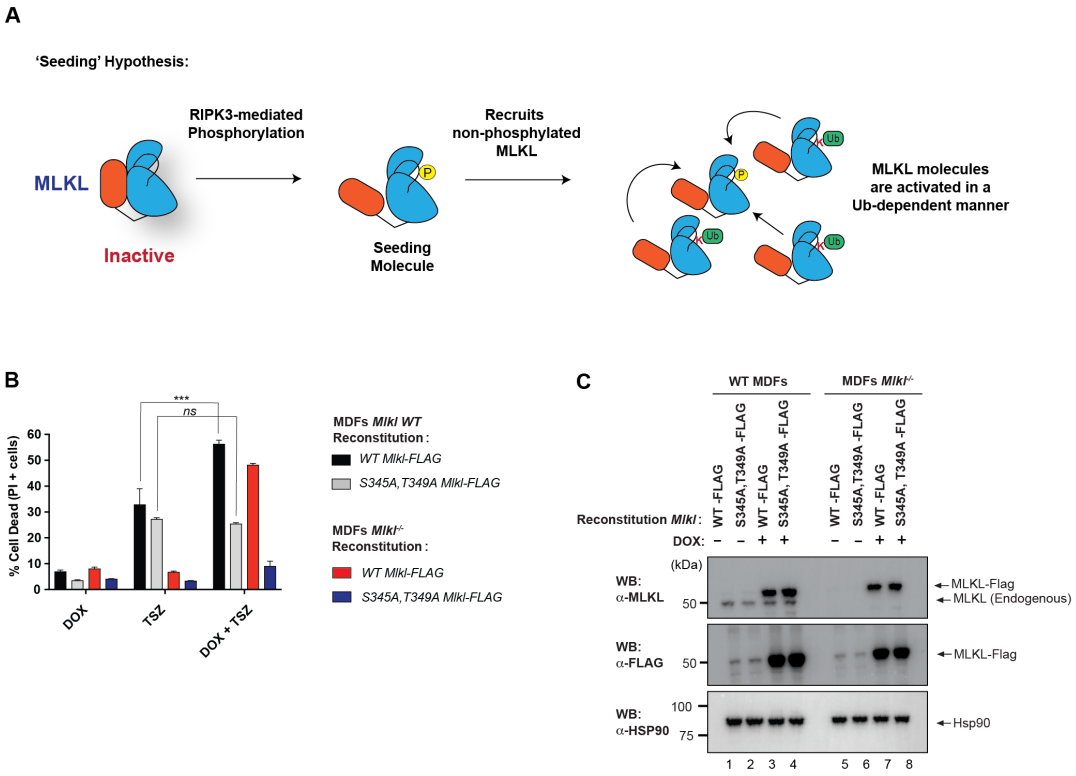

Figure 3.14. MLKL must be phosphorylated to become active.

(A) Schematic representation depicting the 'seeding hypothesis' where some MLKL molecules are phosphorylated by RIPK3 and serve as a 'seed' for further recruitment of unphosphorylated MLKL, which could be activated via Ub-mediated disruption of the K219-Q343 hydrogen bond. **(B)** Expression of S345A, T349A *Mlkl* mutant in a WT background does not enhance cell death. This is in contrast to expression of a WT transgene. WT MDFs or *Mlkl* $^{-/-}$ MDFs cells reconstituted with *Mlkl* $^{WT\text{-}FLAG}$ or *Mlkl*$^{S345A,T349A\text{-}FLAG}$ (phosphomutant). Cells were treated with doxycycline o/n and exposed to TSZ. Data are presented as means ± SD collated from two experiments and analysed in GraphPad Prism 7 with statistical test by two-way ANOVA. ***p <0.001. **(C)** Cells were treated as in (B) and subjected to immunoblot analysis with the indicated antibodies.

3.9. Characterization of *Mlkl* ^{K219R} knockin mouse

3.9.1. Generation and breeding strategy

To further characterize K219R mutation at endogenous level, we generated a *Mlkl*^{K219R} knockin mouse strain using CRISPR-Cas9 technology. Briefly, the sgRNA, Cas9 and donor template harbouring the K219R mutation was injected into a zygote, which was then implanted into a pseudopregnant mouse. The heterozygote mice that were born (F0 generation) were crossed to C57BL/6J mice, and the F1 generation was obtained. The F1 knockin mouse was generated at the Walter and Eliza Hall Institute of Medical Research (WEHI) **(Figure 3.15A).**

To reduce the potential risk of off-target effects, I back-crossed heterozygous animals from the F1 generation to C57BL/6J mice. I obtained several F2 heterozygous mice, which were then crossed *inter-se* to obtain homozygous knockin mice. *Mlkl* $^{K219R/K219R}$ animals were born at predicted Mendelian ratios **(Figure 3.15B),** and were indistinguishable from their *Mlkl*$^{WT/WT}$ littermates.

To verify the genotype, I obtained genomic DNA from the animals and used it to amplify and sequence the *Mlkl* gene. *Mlkl*$^{WT/WT}$ mice present a K (codon AAA) at amino acid position 219, whereas *Mlkl*$^{K219R/K219R}$ animals harbour an R at position 219 (codon CGG) **(Figure 3.15C)**.

B

Total n=mice: 69

Mlkl Genotype	Expected n=(%)	Observed n=(%)
WT/WT	17.25 (25)	14 (20.3)
K219R/K219R	17.25 (25)	19 (27.5)
WT/ K219R	34.5 (50)	36 (52.2)

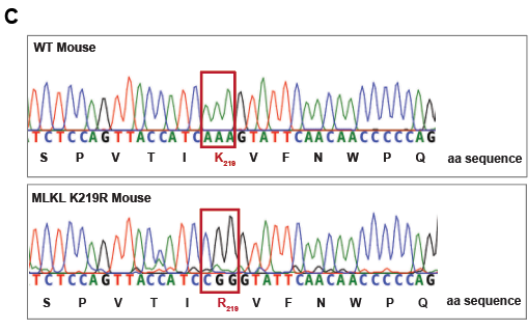

Figure 3.15. Generation and breeding strategy of *Mlkl*^{K219R} knockin animals.

(A) Strategy for the generation of *Mlkl*^{K219R} knockin mice using CRISPR-Cas9 technology. The generation of such animals was carried out at the WEHI. A donor sequence containing the point mutation was injected in a fertilized egg together with sgRNA-*Mlkl* and Cas9. The zygote was then implanted in a pseudopregnant female from which heterozygous mice harbouring the K219R mutation were born (F0). These mice were then back-crossed to C57BL/6J mice, and a cohort of F1 heterozygous animals was obtained. Once we obtained the F1 knockin mouse strain, I performed the second round of back-crossing. To this end I crossed the mutant strain to C57BL/6J to obtain F2 heterozygous animals. F2 offsprings were crossed among themselves to obtain homozygous mice, which were used for further experiments. **(B)** Expected and observed Mendelian inheritance after breeding *Mlkl*$^{WT/K219R}$ X *Mlkl*$^{WT/K219R}$ animals. New-born animals were genotyped and the observed and expected genotypes were annotated, confirming that the *Mlkl*$^{K219R/K219R}$ mice were born at expected Mendelian inheritance. Data were analysed in GraphPad Prism 7 with statistical test by chi-square goodness-of-fit test. **(C)** Sequence of the *Mlkl* gene in *Mlkl*$^{WT/WT}$ and *Mlkl*$^{K219R/K219R}$ mice. The AAA to CGG mutation was introduced to mutate the amino acid at position 219 from K to R.

3.9.2. Characterization of primary BMDMs and MDFs from Mlkl K219R knockin animals

To evaluate the effect of the knockin mutation, I isolated BMDMs from two pairs of *Mlkl*$^{WT/WT}$ and *Mlkl*$^{K219R/K219R}$ animals. For the isolation of BMDMs, the femurs and tibias from these animals were obtained and the bone marrow was extracted. Cells were seeded in medium containing recombinant murine M-CSF, to induce the differentiation of macrophages. The following week, BMDMs were stimulated to undergo necroptosis with TSZ. In agreement with the previously observed phenotype, primary BMDMs from *Mlkl*$^{K219R/K219R}$ animals were less sensitive to the necroptotic stimuli than *Mlkl*$^{WT/WT}$ BMDMs **(Figure 3.16A)**. Of note, *Mlkl*$^{WT/WT}$ and *Mlkl*$^{K219R/K219R}$ BMDMs presented similar protein levels of necroptotic effectors **(Figure 3.16B)**.

To further validate the phenotype in another cell type, I isolated MDFs from the tail of another two pair of *Mlkl*$^{WT/WT}$ and *Mlkl*$^{K219R/K219R}$ mice. To generate a stable line, I immortalized MDFs via retroviral infection with Simian Vacuolating Virus 40 (SV40) Large T Antigen ∆89-97-missing Bub1. Similar to BMDMs, *Mlkl*$^{K219R/K219R}$ MDFs were protected against necroptotic stimuli (2.5 h of treatment) in comparison to *Mlkl*$^{WT/WT}$ cells. *Mlkl*$^{K219R/K219R}$ MDFs were as resistant as cells treated with RIPK1i or RIPK3i **(Figure 3.16C)**. Of note, the protective effect of the K219R mutation was transient as it was partially lost at later timepoints (o/n treatment) **(Figure 3.16D)**. This suggests that this ubiquitylation event enhances MLKL-mediated cell death, but is not indispensable for cell death execution. Of note, P-MLKL was detected in the lysates of *Mlkl*$^{K219R/K219R}$ MDFs at a time point when no cell death was apparent (2.5 h), reinforcing the hypothesis that ubiquitylation at K219 contributes to the killing potential of phosphorylated MLKL **(Figure 3.16E)**.

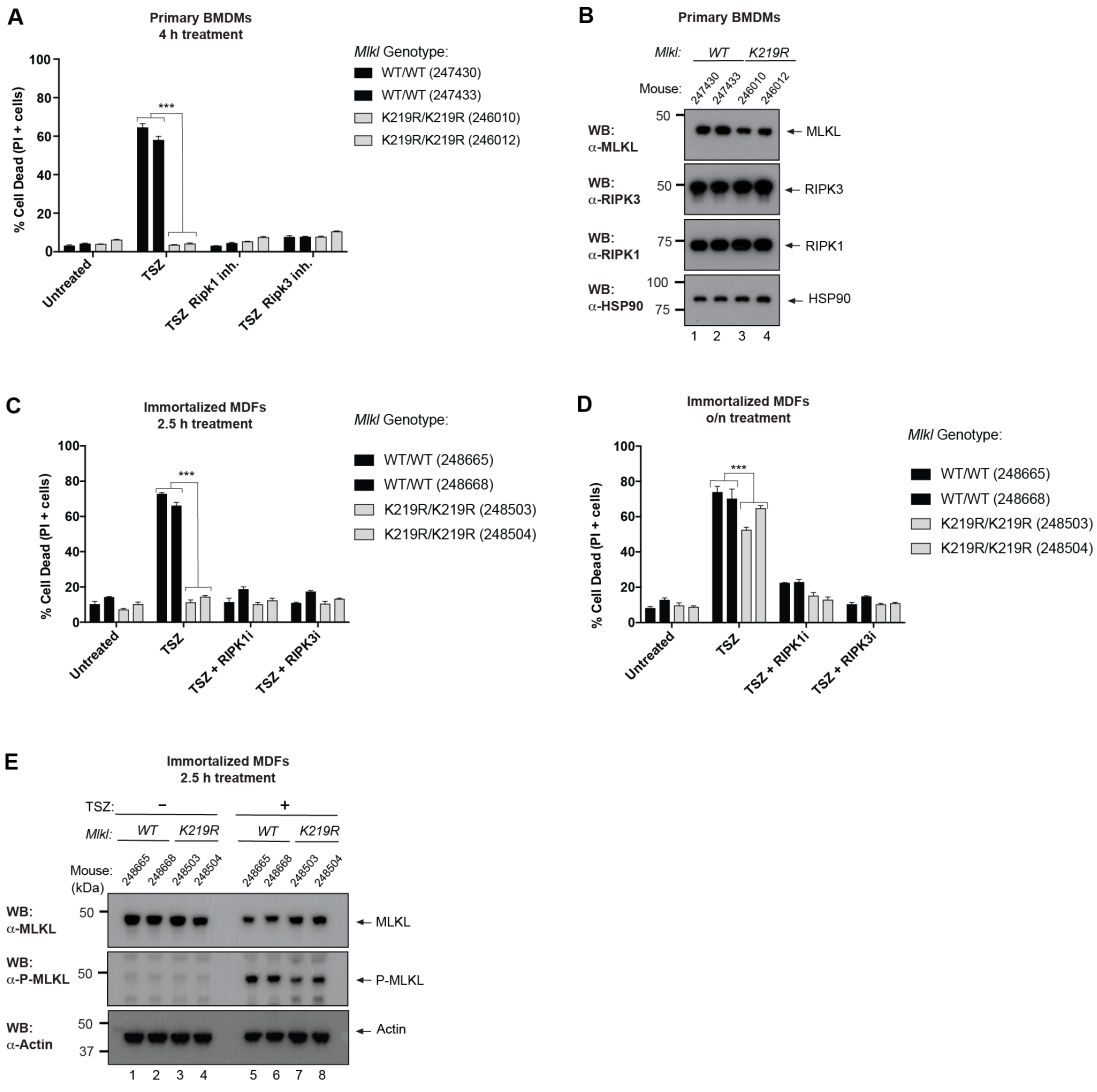

Figure 3.16. Characterization of primary BMDMs and MDFs from *Mlkl*^{K219R} knockin animals.

(A) Primary BMDMs from *Mlkl*$^{K219R/K219R}$ mice are protected from necroptotic stimuli in comparison to in *Mlkl*$^{WT/WT}$ BMDMs. Primary BMDMs were isolated from two pairs of *Mlkl*$^{WT/WT}$ and *Mlkl*$^{K219R/K219R}$ animals and differentiated *in vitro*. Cells were stimulated with TSZ for 4 h in presence or absence of RIPK1i and RIPK3i. Cell death was measured by quantification of PI^{+} cells. (B) Primary BMDMs were analysed by immunoblotting with the indicated antibodies. (C) MDFs from two pairs of *Mlkl*$^{WT/WT}$ and *Mlkl*$^{K219R/K219R}$ littermates were isolated and immortalized. Their sensitivity to TSZ-induced necroptosis was measured by quantification of PI^{+} cells 2.5 h following treatment. Data from A, C and D are presented as means ± SD and analysed in GraphPad Prism 7 with statistical test by two-way ANOVA. ***p <0.001. For the statistical analyses the data corresponding to the same genotype were

pooled together. (D) MDFs were treated as in (C) and cell death was measured after o/n treatment. (E) MDFs were treated as in (C) and the lysates were subject to immunoblot analysis with the indicated antibodies.

4. MLKL interactome and localization during necroptosis

4.1. The E3 ligase TRIM25 does not play a role in necroptosis

Before I joined the lab, Tencho Tenev from the Meier lab, performed a MS experiment aiming to identify novel regulators of MLKL. To this end, he fused two HA-tags to hMLKL and overexpressed it in 293T cells. Subsequently, MLKL was purified by HA-immunoprecipitation and the presence of co-purified proteins was determined by MS. Among others, the E3 ligase TRIpartite Motif 25 (TRIM25) copurified with MLKL (T. Tenev and P. Meier, unpublished data). TRIM25 belongs to the Tripartite Motif (TRIM) family of proteins which is comprised by over 70 members in humans [260]. TRIM family of proteins are RING-type E3 ligases which play key regulatory roles in innate immune signalling pathways [261-263]. They are characterised by a conserved tripartite motif in their N-terminal region, comprised by a RING domain, followed by one or two B-box domains and a coiled-coil domain, that mediates oligomerization. Self-association is crucial for catalytic activity of TRIMs [264]. In particular, TRIM25-mediated K63-linked polyubiquitylation of the RIG-I promoting its oligomerization and inducing its interaction with the downstream effector MAVS (mitochondrial antiviral signalling) [265, 266]. As a result, this leads to the production of TI-IFN, allowing an efficient host immune response [267].

Preliminary experiments using immortalised *Trim25*$^{-/-}$ MEFs indicated that TRIM25 negatively modulates necroptosis (G. Liccardi and P. Meier, data not shown). When I joined the Meier lab, I started by validating these results and exploring whether TRIM25 might regulate MLKL. I depleted TRIM25 in human HaCaT keratinocytes using siRNA-mediated knockdown and studied the sensitivity to TSZ-induced necroptosis. Knockdown of TRIM25 with a pool of siRNAs resulted in a modest sensitization to TSZ in comparison to the non-targeting control oligos **(Figure 4.1A)**. To further validate this phenotype, I assessed the specificity of the siRNA oligos by deconvoluting the siRNA pool. Knockdown of TRIM25 using individual siRNA oligonucleotides did not sensitize to necroptosis, with the exception of oligo 8, which increased the sensitivity to the same extent as the siRNA pool **(Figure 4.1B)**. Since all four oligonucleotides

downregulated TRIM25 expression to the same extent **(Figure 4.1C),** this suggests that the phenotype observed with the pool of siRNAs is not specific to TRIM25, and is therefore highly likely to be an off-target effect.

Nonetheless, to further investigate whether TRIM25 is directly involved in the modulation of the necroptotic pathway, I knocked out *Trim25* in HaCaT cells using CRISPR-Cas9 technology. As a control, I also generated an *Mlkl*$^{-/-}$ clone. Surprisingly, two of the three *Trim25*$^{-/-}$ clones (C1 and C2) were more resistant to TSZ-induced necroptosis, whereas the third clone (C3) behaved as the WT parental clone **(Figure 4.1D),** despite undetectable levels of TRIM25 expression in all three clones **(Figure 4.1E)**. I noticed that clone C1 and C2 had lower levels of RIPK1 and RIPK3 **(Figure 4.1E)**, providing a likely explanation to why these clones were more resistant. As I started from a single clone to generate the *Trim25*$^{-/-}$ clones, the different response to necroptosis might reflect clonal heterogeneity in the parental population of cells. Nevertheless, the *Trim25*$^{-/-}$ C3 had similar expression levels of RIPK1 and RIPK3 as WT cells, yet this clone did not show any change in sensitivity to necroptosis. Other clones, which also had no alterations in the expression of RIPK1 and RIPK3, were as sensitive to necroptotic stimuli as parental cells (data not shown).

Previous work in the Meier lab suggested that immortalized *Trim25*$^{-/-}$ MEFs were significantly more sensitive to TNF-induced necroptosis in comparison to *Trim25*$^{WT/WT}$ MEFs (data not shown). To independently assess this observation in primary murine cells I tested the sensitivity of primary *Trim25*$^{-/-}$ BMDMs to TNF-induced necroptosis. I isolated BMDMs from three pairs of *Trim25*$^{-/-}$ and *Trim25*$^{WT/WT}$ mice. I confirmed the correct genotype of the mice by measuring *Trim25* mRNA levels by qRT-PCR **(Figure 4.1F)** due to the lack of a specific murine anti-TRIM25 antibody. Characterization of these cells indicated that there was no difference in their sensitivity to cell death following treatment with TSZ or ZS **(Figure 4.1G)**.

Together, these results indicate that TRIM25 is unlikely to regulate necroptosis. Therefore, I stopped evaluating the role of TRIM25 in regulating cell death.

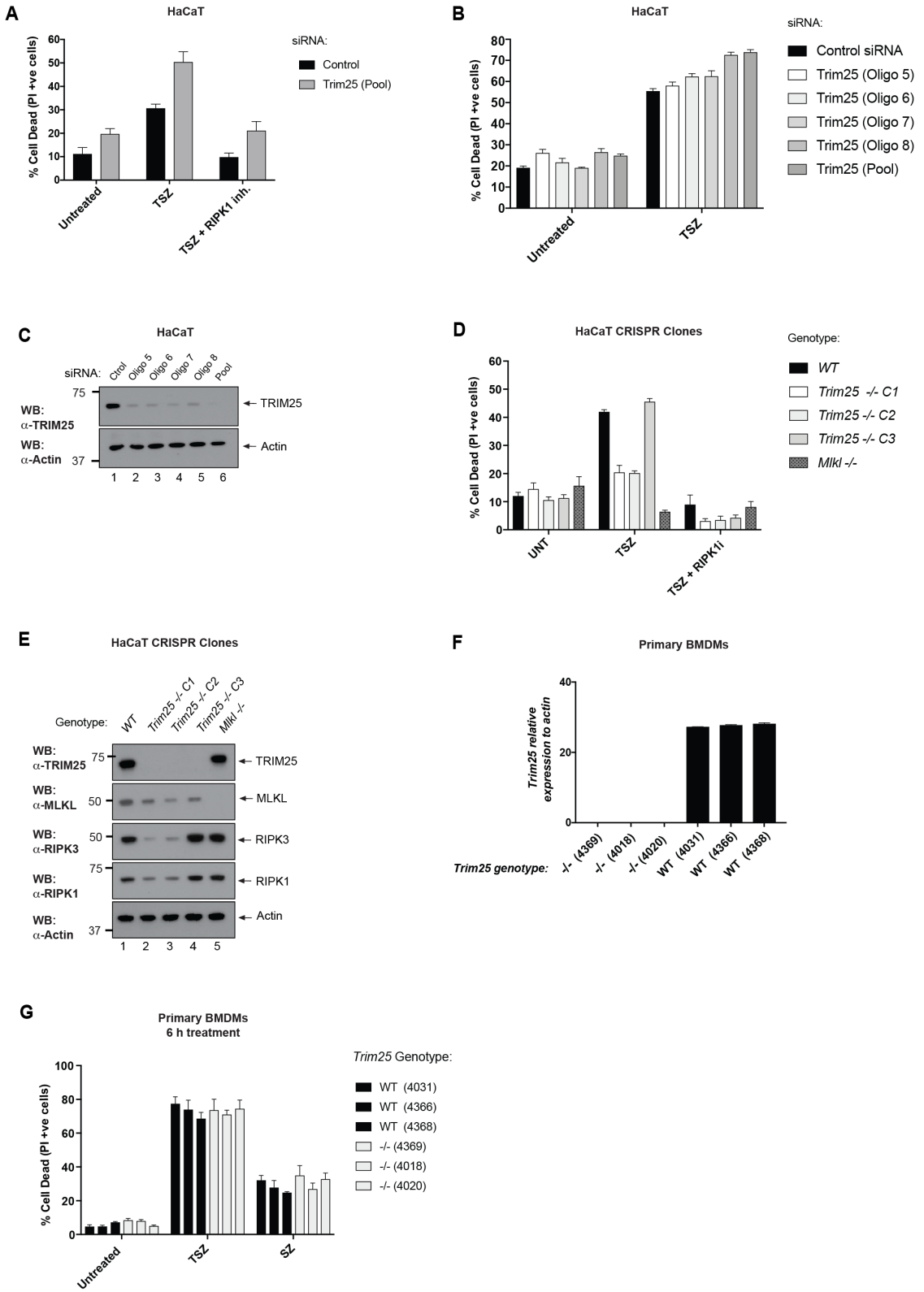

Figure 4.1. TRIM25 does not play a role in TNF-induced necroptosis.

(A) Knockdown of *Trim25* with an siRNA pool of oligonucleotides sensitizes HaCaT cells to TNF-induced necroptosis. HaCaT cells were transfected with *Trim25* -targetting siRNA pool. Following 48 h, cells were stimulated with TSZ and cell death (PI^+ cells) was measured after 24 h of treatment. Data is representative of two independent experiments. (**B)** Deconvolution of siRNA pool targeting *Trim25*. Knockdown of *Trim25* in HaCaT cells (as in A) with individual siRNA oligonucleotides show different phenotypes upon TNF-induced necroptosis. Data is representative of three independent experiments. **(C)** Immunoblot with anti-TRIM25 antibody of lysates of HaCaT cells following siRNA-mediated knockdown shows efficient downregulation in expression for all single siRNA oligonucleotides tested. **(D)** *Trim25* $^{-/-}$ HaCaT clones show different phenotypes upon necroptotic stimulation. HaCaT *Trim25* $^{-/-}$ clones were generated with CRISPR-Cas9 technology and stimulated to undergo TSZ-induced cell death for 24 h. *Trim25* $^{-/-}$ C1 and C2 show protection whereas *Trim25* $^{-/-}$ C3 behaved as parental cells. HaCaT *Mlkl*$^{-/-}$ clones served as a positive control. Data is representative of two independent experiments. **(E)** Immunoblot with the indicated antibodies of the CRISPR cell lines tested in D. *Trim25*$^{-/-}$ C1 and C2 show downregulated expression of key necroptotic components RIPK1 and MLKL, whereas in *Trim25*$^{-/-}$ C3 the expression levels of these proteins are similar to the parental cells. **F)** Primary BMDMs from *Trim25*$^{-/-}$ mice respond as *Trim25*$^{WT/WT}$ BMDMs upon necroptotic stimulation. Primary BMDMs were isolated from 3 pairs of *Trim25*$^{-/-}$ and *Trim25*$^{WT/WT}$ mice as described in Section 2.12.1. Cells were treated as indicated and cell death was measured after 6 h. **(G)** Total RNA isolated from *Trim25*$^{WT/WT}$ and *Trim25*$^{-/-}$ BMDMs was used to quantify *Trim25* mRNA expression by qRT-PCR. Actin was used as a housekeeping gene for normalization.

4.2. LC-MS/MS analysis to identify novel MLKL interactors

With the aim of finding new MLKL interactors and potentially an E3 ligase responsible for MLKL ubiquitylation, I conducted a mass spec experiment. For this, I first tested the ability of several antibodies to immunoprecipitate endogenous murine and human MLKL from cellular extracts. While none of the antibodies was capable of purifying mMLKL (data not shown), I could successfully immunoprecipitate hMLKL from extracts of HT-29 cells **(Figures 4.2A)**. Of note, the immunoprecipitation was more efficient under TSZ conditions, suggesting that the conformational change of active, phosphorylated MLKL might be expose an epitope that allows it to be immunoprecipitated with greater success. Importantly, I was able to copurify endogenous RIPK3, the *bona fide* MLKL interactor, following 8 h of TSZ stimulation.

To identify novel MLKL interactors, HT-29 cells were treated with TSZ for 8 h and endogenous MLKL was immunoprecipitated. An isotype antibody was used as control. Following the immunoprecipitation, the samples were subject to digestion with trypsin prior to LC-MS/MS analysis **(Figures 4.2B)**. The samples of two biological replicates were analysed. To facilitate the identification of relevant groups of related proteins enriched upon MLKL immunoprecipitation, a pathway analysis was performed. The resulting network of MLKL-related proteins can be found in **Supplementary Figure 6.1**. This analysis revealed enrichment of several pathways, such as those related to programmed cell death and apoptotic cleavage. The flotillin complex, recently reported to be involved in necroptosis was also detected [200, 268].

Interestingly, I identified several proteins of the desmosome complex, a complex involved in cell-cell adhesion. In particular, five desmosomal proteins were enriched in the MLKL immunoprecipitated samples among the two replicates **(Figures 4.2C)**. Although MLKL has been reported to translocate to the plasma membrane to induce cell death [188, 193], little is known with regards to its localization at the plasma membrane. Also, the exact mechanism of cell death execution or the potential communication between a cell undergoing necroptosis and its neighbouring cells is poorly understood. The interaction between MLKL

and proteins of the desmosomes prompted me to further investigate these questions.

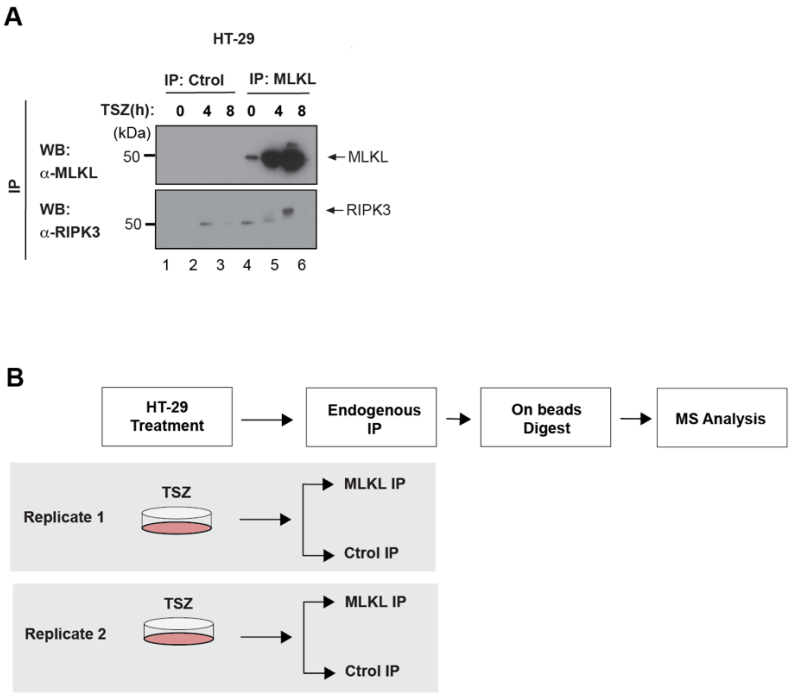

C

Description	Abbrev.	Replicate 1 Ctrol IP # Peptides	Replicate 1 MLKL IP # Peptides	Replicate 2 Ctrol IP # Peptides	Replicate 2 MLKL IP # Peptides
Mixed lineage kinase domain-like protein	MLKL		19		21
Desmoplakin	DSP	1	16		6
Junction plakoglobin	JUP	2	13		3
Desmoglein-1	DSG1		6		
Desmocollin-1	DSC1		3		
Plakophilin-1	PKP1		3		

Figure 4.2. LC-MS/MS analysis to identify novel MLKL interactors.

(A) hMLKL is immunoprecipitated following TSZ treatment. HT-29 cells were treated with necroptotic stimuli (TSZ) for the indicated times and subject to immunoprecipitation with an anti-MLKL antibody or a Control (Ctrol) antibody. Immunoblot with anti-MLKL and anti-RIPK3 antibodies of the purified material is shown. Immunoprecipitation as described in Section 2.10.1.1. **(B)** Graphical representation of the experimental procedures for analysis of MLKL interactors following TSZ treatment for 8 h. Dr. Lu Yu and Dr. Mercedes Calvo performed the LC-MS/MS analysis and the identification of the peptides. **(C)** Table showing the number of peptides identified in each sample for proteins that comprise the desmosome complex, involved in cell-cell adhesion.

4.3. P-MLKL localises to cell-cell contact sites

Considering that desmosomal proteins were enriched in MLKL immunoprecipitated samples, I next investigated the localization of MLKL in the plasma membrane following necroptosis induction.

To this end, HT-29 cells were treated with TSZ for 8 h prior to fixation and permeabilization. To detect active MLKL, cells were stained with an anti-P-MLKL specific antibody. Staining with Wheat Germ Agglutinin (WGA) was used to visualize the plasma membrane. WGA is a lectin that binds to carbohydrate (sialic acid and N-acetylglucosamine) on the plasma membrane [269]. Confocal microscopy analysis showed that P-MLKL was present at the contact sites between adjacent cells **(Figure 4.3A, panel 2).** Importantly, this staining was specific as no P-MLKL signal was detected in untreated conditions, or upon blocking necroptosis with RIPK1i **(Figure 4.3A, panel 1 and 3).** Further, HT-29 *Mlkl*$^{-/-}$ cells treated with TSZ did not show a P-MLKL signal **(Figure 4.3A, panel 4)**. Higher magnification indicate that the P-MLKL signal is positioned at the cell-cell contact sites **(Figures 4.3B).** These images show a clear polarization of P-MLKL towards the site of contact with the neighbouring cells. Of note, image number 3 shows that even when the contact surface between the two cells is small, P-MLKL still is recruited to this site of contact. These results indicate that active MLKL preferentially localises to contact sites of neighbouring cells.

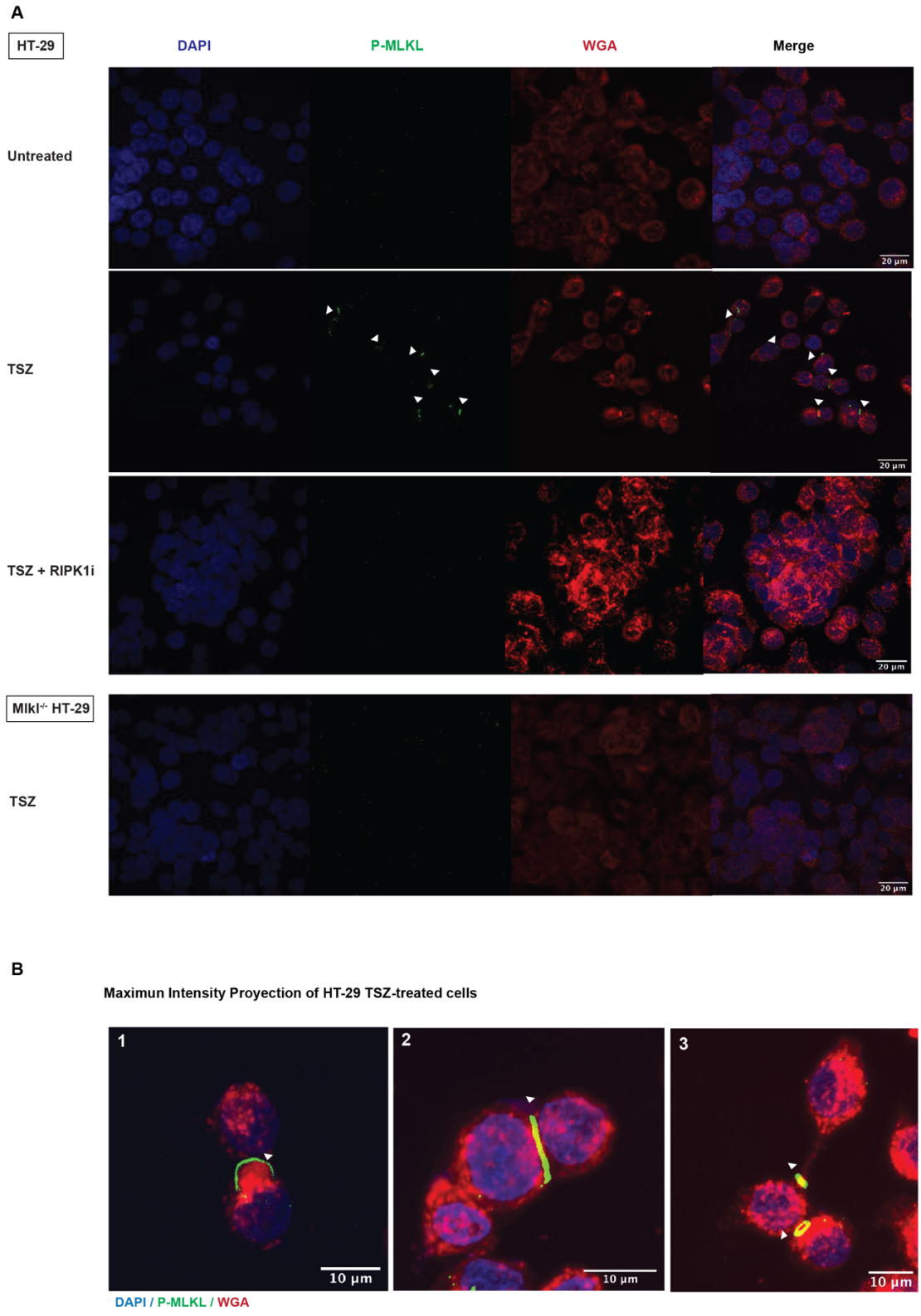

Figure 4.3. P-MLKL localizes to cell-cell contact sites.

(A) Immunofluorescence staining of P-MLKL and WGA in HT-29 cells. HT-29 cells were treated with TSZ for 6 h in the presence or absence of RIPK1i, or left untreated. Following treatment, cells were fixed with 4 % PFA for 10 min, permeabilized with 1 X PBS, 0.5 % Triton X-100 for 10 min and stained with antibodies against P-MLKL (green) and WGA (red). Nuclei were stained using DAPI. White arrows indicate the localization of the P-MLKL signal between two adjacent cells. As a control for P-MLKL staining, *Mlkl*$^{-/-}$ HT-29 cells were treated and immunostained as in A. Scale bar, 20 μM. **(B)** Immunofluorescence staining of P-MLKL and WGA in HT-29 cells. Cells shown in A. (TSZ treated) were acquired at higher resolution (63X objective). Three representative images are shown. White arrows indicate the localization of the P-MLKL signal between two adjacent cells. Scale bar, 10 μM. Representative images of Maximum Intensity Projections (MIP) are shown.

4.3.1. P-MLKL forms 'ring-like' structures at cell-cell contact sites

To gain further insight into the localization of P-MLKL signal, I acquired Z stacks and reconstructed a 3D image in HT-29 cells following TSZ treatment. Interestingly, I observed a significant amount of well-defined ring-like structures forming between two adjacent cells which were specific for P-MLKL **(Figures 4.4A).** These data demonstrate that P-MLKL is predominantly recruited to cell-cell contact sites and forms 'ring-like' structures. To determine whether such P-MLKL rings are a general phenomenon occurring during necroptosis, I analysed LoVo cells, a human colorectal cancer cell line that can undergo necroptosis. Similar to HT-29, P-MLKL rings formed in adjacent cells **(Figures 4.4B)**, suggesting that these rings are a common feature of necroptosis.

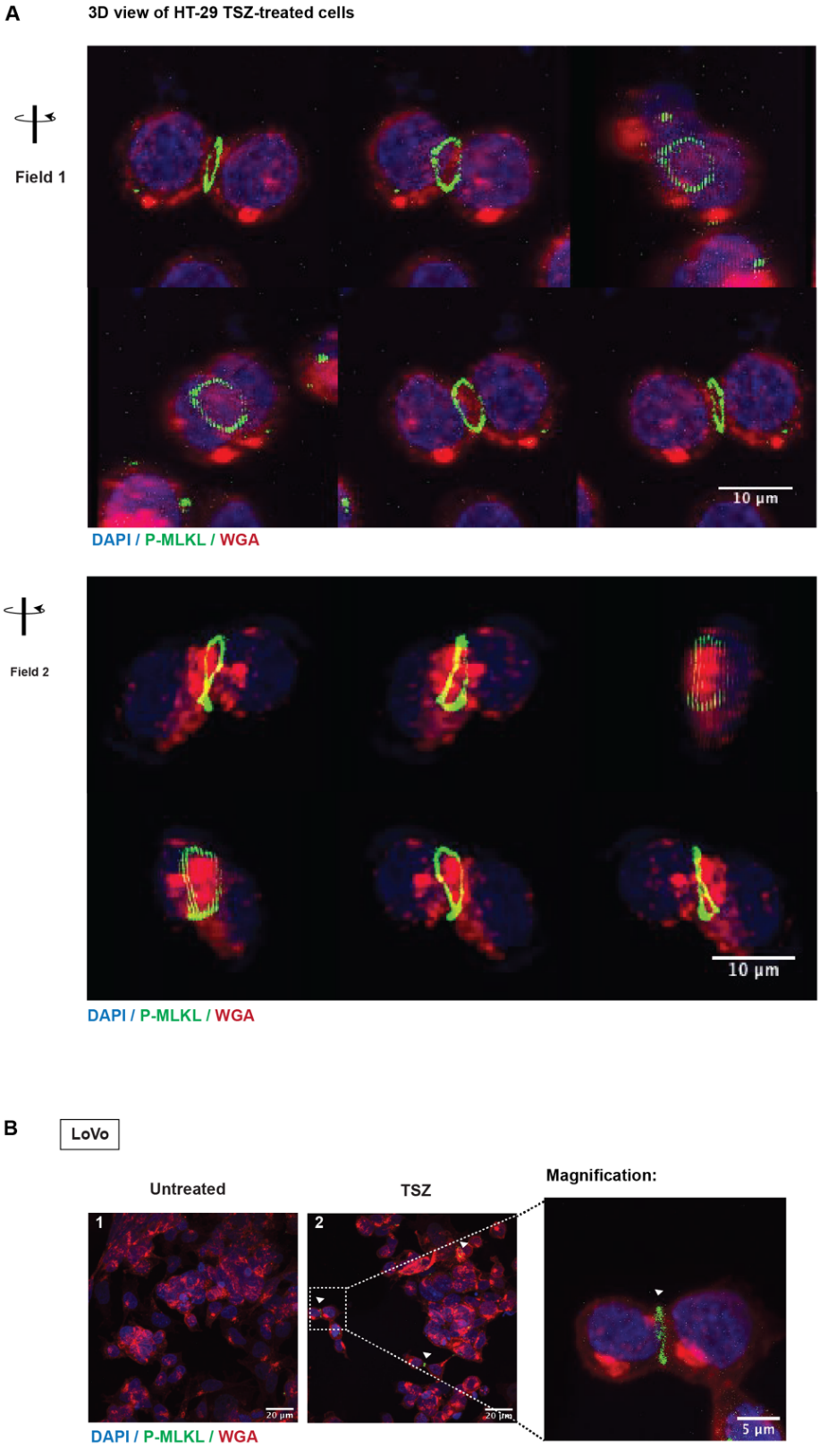

Figure 4.4. P-MLKL forms 'ring-like' structures at cell-cell contact sites.

(A) Immunofluorescence staining of P-MLKL and WGA in HT-29 cells undergoing necroptosis. Figure shows a montage of a 3D projection movie. Two representative montages of movies are shown (Field 1 and Field 2). Scale bar, 10 μM. **(B)** Immunofluorescence staining of P-MLKL and WGA in LoVo cells. LoVo cells were left untreated (panel 1) or treated with TSZ for 18 h (panel 2). Following treatment, cells were fixed with 4% PFA for 10 min, permeabilized with 1X PBS, 0.5 % Triton X-100 for 10 min and stained with antibodies against P-MLKL (green) and WGA (red). Nuclei were stained using DAPI. White arrows indicate the localization of the P-MLKL signal between two adjacent cells. Right panel shows enlarged image corresponding to the white rectangle (Scale bar, 5 μM in magnified image and 20 μM in the remaining images). Representative images of Maximum Intensity Projections (MIP) are shown.

5. Discussion

5.1. Ubiquitin-mediated modulation of MLKL

Necroptosis plays a key role in host defence against numerous pathogens and contributes to the maintenance of tissue homeostasis [201]. Due to the potential deleterious effect of uncontrolled or excessive necroptotic cell death it is not surprising that the core components of the necroptotic machinery are subject to tight regulation. In Chapter 3, I demonstrate that MLKL-mediated necroptosis is regulated in a Ub-dependent manner. In particular, ubiquitylation at K219, a key pseudoactive site residue of MLKL, enhances the ability of MLKL to induce cell death. Using pharmacological inhibitors as well as genetically engineered cell lines I demonstrate that MLKL ubiquitylation occurs in the cytosol and requires RIPK3-mediated phosphorylation. Further I show that ubiquitylation of MLKL influences polymer formation at the plasma membrane. Together, my data highlight the importance of phosphorylation and ubiquitylation. I find that both of these modifications take place simultaneously in the same pool of MLKL molecules and cooperate to induce maximal MLKL activation.

Structural studies of full-length mMLKL support the idea that MLKL is kept in an inactive conformation and undergoes a conformational change upon necroptotic stimulation, leading to MLKL activation. Central to this conformational change is the disruption of the hydrogen bond between K219 and Q343 [178]. For a hydrogen bond to be formed, two electronegative atoms need to interact with the same hydrogen, which is covalently attached to one of the atoms (hydrogen-bond donor) and it interacts electrostatically with the other atom (hydrogen bond acceptor). In the case of mMLKL, the hydrogen bond is formed between the ε-amino group of K219 (N is the hydrogen bond donor) and the oxygen atom of the carbonyl group of Q343 (O is the hydrogen bond acceptor). Given that phosphorylation of MLKL by RIPK3 occurs in proximity to the hydrogen bond (S345), it is thought that phosphorylation impairs the formation of the hydrogen bond, and thus results in MLKL activation [178]. The discovery that K219 is ubiquitylated upon necroptotic stimulation suggests that MLKL's pseudoactive site conformation could be regulated by both phosphorylation and ubiquitylation.

Indeed, both PTMs seem to influence MLKL's killing activity. Considering that Ub is covalently attached to the ε-amino group of K219, this modification will affect the hydrogen bond between K219 and Q343, possibly causing structural rearrangements. Importantly, Murphy *et al*. showed that the mutations K219M or Q343A result in constitutive MLKL activation. Although both mutations abrogate the hydrogen bond, the killing activity of the Q343A mutant was much greater than that of the K219M mutant [178]. This might indicate that additional regulatory mechanisms involving K219 might affect MLKL's killing potential. My observation that K219 is ubiquitylated, and is required for optimal polymer formation and cell death, may help to explain the discrepancy between Q343A and K219M. Accordingly, the Q343 mutant may not only be in an active configuration but may also be ubiquitylated at K219. This may help MLKL to form polymers and execute cell death. In contrast, the K219M mutant form of MLKL may only be in an active state but is not ubiquitylated at this site.

At present it remains unclear how ubiquitylation of K219 enhances MLKL polymer formation and cell death. Ub might help to push MLKL into an active conformation. Such mechanism of regulation is often observed in protein kinases, which are highly dynamic and switch between different conformations, such as a kinase active state and an 'off' state with minimal activity [164]. Toggling between such states can be influenced by many factors, including PTMs, regulatory proteins or ligand binding [164, 270]. In support of this hypothesis, Ub modifications are frequently observed at sites that are important for kinase regulation [271, 272]. For instance, many kinases are ubiquitylated in the activation loop (near the DFG motif), the glycine loop and in the helix αC, which constitute key structural features involved in kinase activation [270, 273]. Computational simulation of ubiquitylation in key regulatory sites using molecular dynamics shows that Ub can influence the structure and dynamics of ZAP-70 in a site-dependent manner, ultimately affecting its activation state [273]. These observations strengthen the hypothesis that Ub could be directly involved in the molecular switch mechanism of MLKL activation. Nonetheless, in the absence of a phosphorylated and ubiquitylated MLKL structure, the specific conformational changes that occur upon MLKL activation and how they contribute to it, remains an open question.

Despite good evidence to suggest that ubiquitylation might directly impose a certain conformational change that favours MLKL's killing activity **(Figure 5.1A)**, other hypothesis is that the ubiquitination at K219 enhances necroptosis by facilitating downstream signalling events **(Figure 5.1B)**. This is supported by the observation that cells expressing MLKL K219R show reduced ability to assemble into higher order oligomers at the plasma membrane. In this regard, one possibility is that proteins containing UBDs might bind to ubiquitylated MLKL, inducing its clustering and aggregation into high order polymers. Considering that more than one residue is ubiquitylated, I cannot rule out the possibility that different ubiquitylation events cooperate to enhance MLKL's killing function.

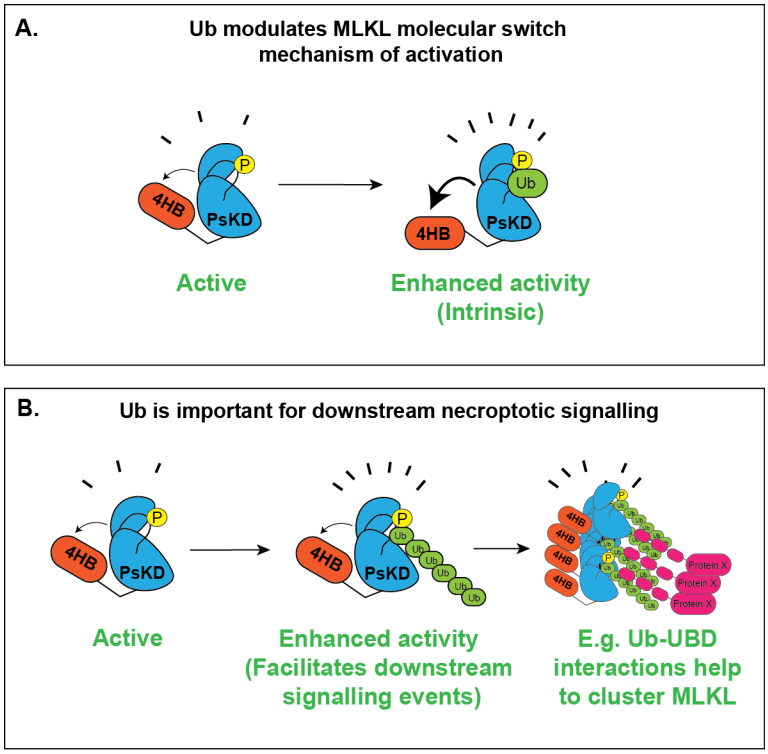

Figure 5.1. Two models of positive modulation for MLKL activity by Ub

Depicted are two possible models that help to explain the ability of Ub to positively regulate MLKL-mediated necroptosis, either by affecting the molecular switch mechanism (A) or by mediating downstream signalling events. For instance, recognition of Ub chains by proteins containing UBDs might help to cluster MLKL molecules and enhance their higher order assembly(B).

A major barrier to study in detail the regulatory events triggered by ubiquitylation at specific residues is due to the difficulty of preparing modified proteins *in vitro* (proteins ubiquitylated at specific residues) and by the impossibility to selectively trigger ubiquitylation in living cells. In the last years, new chemical methods have been developed to induce site-specific ubiquitylation of proteins in mammalian cells [274]. These methods could be applied to characterize in detail the effect of K219 ubiquitylation on MLKL function. In particular, it would facilitate the resolution of the crystal structure of ubiquitylated MLKL. Alternatively, other methods such as computational structural modelling could be applied to predict the consequence of ubiquitylation on MLKL structure, as it has previously been done for other ubiquitinated proteins [273]. In this study, the role of ubiquitylation at K219 was explored by mutation of such residue to R. Nonetheless, given its crucial location within MLKL's pseudoactive site and the fact that it forms a hydrogen bond with Q343, it could be a possibility that the mutation itself has an effect on MLKL's function. Thus, the aforementioned approaches, which do not rely on mutagenesis, would be important to support the pro-death role of ubiquitylation at K219.

At present it is unclear what type of linkage is attached to K219, or whether a single Ub moiety is conjugated to this site. Unfortunately, it is currently not technically possible to address this issue. While in this study I failed to detect M1 and K48-linked Ub chains on MLKL, I could not address the presence of K6-, K11-, K27-, K29- and K33-linked Ub chains. In this regard, although I conducted several attempts using UbiCrest, the results were inconclusive. Therefore, the precise Ub linkage repertoire of MLKL remains to be determined. The use of mass spec in combination with Ub absolute quantification (AQUA) peptides may help to resolve this issue.

In addition to K219, I identified three additional Ks ubiquitylated on MLKL. Future work will be required to address the functional role of these sites. Also, more work will be needed to identify potential additional sites for MLKL ubiquitylation. In support of this, mutation of the four ubiquitylated K residues was not sufficient

to abrogate the ubiquitylation of MLKL (data not shown), suggesting that MLKL is ubiquitylated at additional sites.

Another relevant question that requires further investigation is in regards to the quantification of the stoichiometry of the ubiquitylated K identified by mass spec. In particular, the stoichiometry for ubiquitylation at K219. PTM site stoichiometry indicates the fraction of the protein that is modified with a given PTM at a specific site. Stoichiometry is an important property of PTMs and would be relevant to support the mechanistic model of Ub-dependent MLKL activation. My mass spec data shows that there is an enrichment in the detection of ubiquitylated K219 following necroptosis engagement. However, the fact that the relative abundance of ubiquitylation at K219 is increased by fivefold over the untreated control, could either mean an increase in site stoichiometry from 1% to 5% or from 10% to 50%. It is important to bear in mind that such large differences in site stoichiometry might have difference consequences on overall protein function [1]. Different MS-approaches for determining PTM site stoichiometry have been developed [275]. For instance, the AQUA method allows to accurately measure the absolute amount of a given peptide by spiking a known quantity of the stable isotope labelled peptide standard and comparing the intensity of the native and reference peptides in MS. Standard AQUA-based PTM stoichiometry would require the quantification of both, the peptide containing the diGG remnant at position K219 as well as the correspondent unmodified peptide or total amount of MLKL. Of note, while stoichiometry itself is not an indicator of PTM function, those sites that occur at high stoichiometry are more likely to have a function (e.g. such as regulating MLKL activity in the case of ubiquitylation at K219).

MLKL is not only ubiquitylated in mouse cells, but also in the human setting. Of note, K219 and Q343 residues of mMLKL are evolutionarily conserved among MLKL from different species, suggesting that they serve important functions. The correspondent residues in the human setting are K230 and Q356. Nevertheless, differences between mouse and human are becoming increasingly apparent [165]. One of these differences concerns interactions among the residues of the pseudoactive site. Typically, in protein kinases, the catalytic $\beta 3$ K (K72 in the

archetypal PKA) forms an ionic bond with a canonical glutamate (E) that is located in the αC helix (E91 in PKA, **Figure 5.2A**) [276]. However, in mMLKL an atypical α-helix is formed by the N-terminal segment of the MLKL activation loop, displacing the αC helix from its canonical position. As a result, the catalytic *β3* K of mMLKL (K219) forms a hydrogen bond with Q343 of the activation loop, instead of the canonical E in the αC helix E (**Figure 5.2B**) [178]. In contrast to this unusual arrangement, in hMLKL the canonical ionic bond is formed between K230 and E250 from the αC helix (Figure 5.2C) [183, 277]. In addition to this structural difference, the killing activity of hMLKL seems more tightly modulated. Contrary to mMLKL, phosphomimetic mutations in the activation loop (T357E, S358E) or mutations within hMLKL's pseudoactive site (K230M) are insufficient to cause necroptosis in the absence of stimuli [181]. Of note, various human cancers carry mutations in the pseudoactive site of MLKL. For example, the K230Q mutation is observed in colon carcinoma [181]. This might suggest that these residues are relevant for MLKL activation. Consistent with this idea, expression of $hMLKL^{K230M}$ leads to a slower cell death kinetic following necroptotic stimulation [181], suggesting that this mutation compromises MLKL's killing function. In light of the differences between mouse and human MLKL, it will be interesting to corroborate my findings in human cells. Of note, a whole ubiquitome study of Jurkat cells identified K230 to be ubiquitylated [278], corroborating my findings in murine cells.

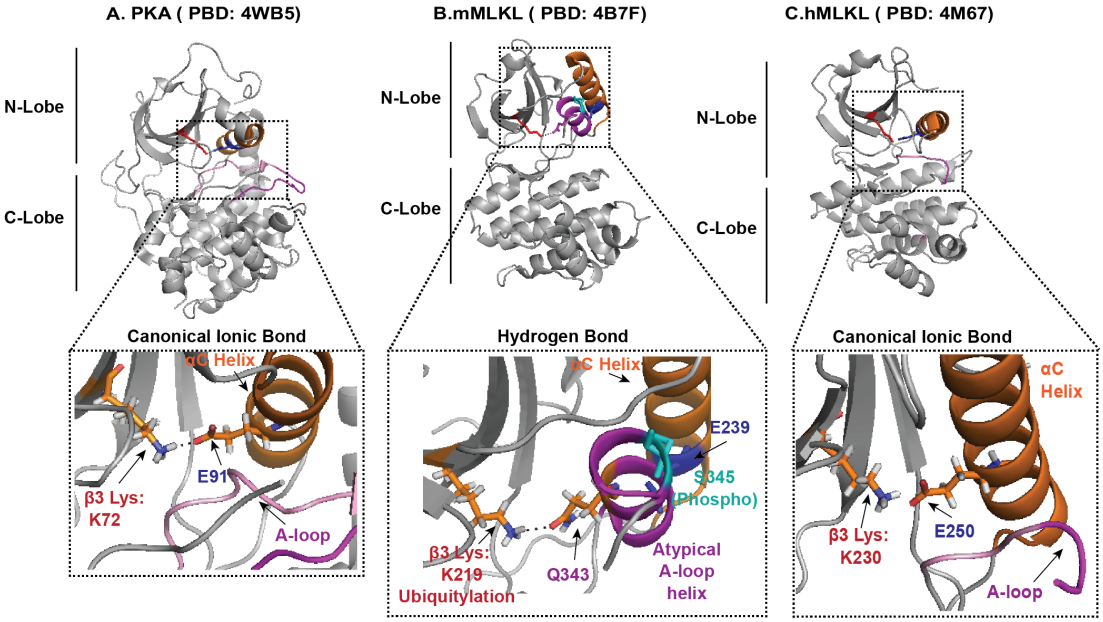

Figure 5.2. Arrangement of key residues in the active site of PKA and the pseudoactive site of mMLKL and hMLKL.

Structure of the kinase domain of human PKA (A, PDB: 4WB5 [259]), and the pseudokinase domain of mMLKL (B, PDB: 4B7F [178]) and hMLKL (C, PDB:4M67 [183]). The kinase/ pseudokinase domain is represented in grey and the active/ pseudoactive site is magnified with key residues and structural motifs highlighted in colours. The side chains of the residues that form the canonical hydrogen bond are represented as sticks and coloured by atom type (carbon atoms in orange, nitrogen atoms in blue, oxygen atoms in red and hydrogen atoms in grey). The αC helix is shown in orange and the activation loop (A-loop) is shown in magenta. A canonical ionic bond between the *β3* K and the E located within the αC helix is formed in PKA (A) and in hMLKL (C). In mMLKL (B), an atypical helix in the A-loop is observed, displacing the canonical location of the αC helix and resulting in the formation of an atypical hydrogen bond between the *β3* K and a Q residue (Q343) within the A-loop. The 3D structures were generated using PyMOL Software.

Of note, necroptosis is not fully blocked in MLKL^{K219R} mutant cells but is merely delayed. Thus, ubiquitylation of K219 seem to regulate the kinetics of cell death. This might be relevant under certain pathogenic settings. In this regard, several studies support a role of necroptotic death in innate immunity. In particular, the most direct evidence to support this is the identification of the virus-encoded

necroptotic inhibitors that target RHIM motifs in RIPK1, RIPK3 and ZBP1 to prevent necrosome assembly [176, 217, 218]. Importantly, mechanisms to counteract necroptosis would not have been retained over millions of years of evolution if necroptosis would not play a role in host defense. Nonetheless, an intriguing point in regards to the physiological role of necroptosis is the fact that RIPK3 and or MLKL expression is lost across different species. For instance, some animals such as the whole Carnivora order (e.g. dogs and cats), appear to lack *Mlkl* gene [279]. On the other hand, birds and marsupials lack *Ripk3* [279]. The fact that components of this pathway are surprisingly poorly conserved, suggests that RIPK3-MLKL-driven necroptosis (as characterized in human and mouse cells) cannot be a universal cell death pathway and therefore it questions its universal role in innate immunity. In this regard, it will be important to determine whether cells from those species that lack *Ripk3* or *Mlkl* can still undergo necroptosis by engaging alternative unidentified proteins that can substitute them. For instance, in those species that lack *Mlkl*, it is possible that a paralogous MLKL-like protein exists. Alternatively, it might just be an indication that RIPK3 has additional functions in other pathways other than necroptosis. On the other hand, because some species still express MLKL but not RIPK3, this might reflect the fact that an alternative mechanism for MLKL activation might exit independent of RIPK3. Another possibility is that those species that cannot engage necroptosis rely more on alternative necrosis-like cell death pathways to combat pathogen infection. Interestingly, a recent study has provided the first evidence of non-RHIM targeting viral antagonist of necroptosis by identifying truncated MLKL homologs (only comprising the pseudokinase domain) within the genome of poxviruses [280]. Viral MLKL (vMLKL) from distinct poxviruses can selectively inhibit necroptosis via distinct mechanisms in human and mouse cells [280]. Thus, it is possible that vMLKL proteins might have exerted selective pressures that have led to distinct mechanistic differences between necroptosis signalling in mouse and human MLKL. Considering the data presented in this study, it would be interesting to investigate whether viral DUBs that target MLKL might exists as a means to counteract necroptosis.

While the physiological role of necroptosis is mostly limited to pathogen infection, and outstanding question still remains in regards to the implication of this pathway in human diseases. In particular, necroptosis has been reported to occur in diseases characterized by sterile inflammatory component such as neurodegenerative diseases, including Alzheimer's disease, Amyotrophic Lateral Sclerosis, Parkinson's disease; renal diseases such as acute kidney injury and cardiovascular diseases including atherosclerosis and ischemia reperfusion injury [281]. However, solid *in vivo* experimental proof for the implication of necroptosis in these diseases is still lacking due to the lack of reliable necroptotic biomarkers to distinguish between unregulated/accidental necrosis and necroptosis. In addition, many *in vivo* studies have relied on the use of RIPK3$^{-/-}$ mice as a mean to demonstrate a role for necroptosis in these conditions. Given the involvement of RIPK3 in inducing inflammation in a cell death independent manner [282], some of the conclusions drawn utilizing the RIPK3$^{-/-}$ mice might be misleading and need to be reproduced in MLKL-deficient background. This concern became evident after the comparison of RIPK3$^{-/-}$, RIPK1^{KD} and MLKL$^{-/-}$ mice in different models of inflammation and tissue injury, and demonstrating that RIPK3 and RIPK1 deficient mice were better protected than MLKL$^{-/-}$ mice [283], presumably due to their contribution to inflammation in a necroptosis-independent manner. Thus, while the inflammatory capacity of necroptosis has been convincingly proven genetically generating knockout mice (e.g. RIPK1$^{-/-}$ mice [284]), an outstanding question still remains as to whether certain pathogenic settings are indeed caused by exacerbated necroptotic cell death and provided this was the case, it also remains to be further investigated what are the molecular mechanisms that allow necroptosis engagement in those disease-specific settings.

Given the potential implication of necroptosis in a variety of inflammatory diseases, the interest in therapeutically targeting this pathway is increasing. In particular, MLKL constitutes a good target candidate since mice lacking MLKL develop normally into healthy animals [178], suggesting that inhibition of MLKL would be well tolerated. My studies help to advance the field by providing a deep understanding at a molecular level of the mechanism involved in MLKL activation. This knowledge might facilitate the development of highly specific

MLKL modulators. For instance, it will open new avenues to explore the possibility of activating MLKL in the context of anti-cancer therapy to overcome apoptotic-resistant cancers.

In addition to MLKL, I also observed ubiquitylated Ks on RIPK1, RIPK3 and Caspase-8. In particular, ubiquitylation on RIPK1 was detected on K163, K307, K115 and K167. Nonetheless, out of this 4 Ks, only ubiquitylation at K307 was enriched following TSZ stimulation **(Supplementary Figure 6.2A)**. Consequently, future studies are required to evaluate the role of ubiquitylation of K307 in necroptosis. Interestingly, K115 of mRIPK1 has been previously reported to be ubiquitylated under necroptotic conditions, although in the human setting [241]. Functional analysis showed that mutation of K115 to R (K115R) reduced its ability to engage necroptotic cell death when reconstituted in HT-29 *Ripk1*$^{-/-}$ cells, in comparison to reconstitution with *WT* hRIPK1 [241]. Mechanistically, cells expressing hRIPK1^{K115R} had reduced auto-phosphorylation at S166 (marker for RIPK1 activation), as well as reduced hRIPK3 phosphorylation, which consequently leads to diminished ability to mediate cell death [241]. The E3 ligase Peli1 was reportedly responsible to mediate K63-linked ubiquitylation at K115 during necroptosis [242], and therefore suggested to be a positive modulator of the pathway. Nevertheless, another study described that Peli1 ubiquitylates RIPK3 to induce its proteasomal degradation and thereby acts as a negative modulator of the pathway [245]. While the reason for these discrepancies are unclear, further studies are required to elucidate the function of Peli1 in necroptosis.

Several previous studies indicated that RIPK3 is ubiquitylated during necroptosis [243, 245, 246, 285]. I detected three Ks ubiquitylated in RIPK3 that have not been reported before: K57, K230 and K469. Following TSZ treatment, increased abundance of ubiquitylation was observed only in K469 **(Supplementary Figure 6.2B).** Given that this K is located few amino acids away from the RHIM domain (458-461), it would be interesting to study its role in the regulation of necroptosis.

Lastly, two ubiquitylated Ks of Caspase-8 (K226 and K274) were detected following necroptotic treatment. In particular, ubiquitylation of K274 was enhanced following TSZ treatment **(Supplementary Figure 6.2C).** While caspase-8 is regulated in a Ub dependent manner during apoptosis [286, 287], the notion that this site is specifically enriched under necroptotic conditions suggests that it serves to inactivate caspase-8.

5.2. MLKL Interactome and localization upon necroptosis engagement

5.2.1. TRIM25 as a putative necroptosis modulator

The identification of the E3 ligase that ubiquitylates MLKL would allow me to corroborate my findings that MLKL-mediated necroptosis is regulated in a Ub-dependent manner. Based on previous MS experiments, and preliminary data obtained in the Meier lab (unpublished observation), I decided to evaluate the role of the E3 ligase TRIM25 in regulating necroptosis.

To this end, I used three different approaches: (1) siRNA mediated knockdown of TRIM25; (2) TRIM25 depletion via the CRISPR-Cas9 system and (3) a genetic mouse model lacking TRIM25. While I was able to validate that TRIM25 can be efficiently knockdown using different siRNA oligonucleotides, I could not reproducibly observe that depletion of TRIM25 had a significant effect on necroptosis. Additionally, although I observed that several of the *Trim25*$^{-/-}$ CRISPR clones were more resistant to necroptosis, this was likely due to decreased expression of RIPK1 and RIPK3. It should be noted that a reduction in RIPK3 expression levels is frequently observed upon passaging of MEFs due to silencing by methylation [288]. Finally, characterization of primary *Trim25*$^{-/-}$ BMDMs did not show any significant difference in necroptotic cell death. While it is well accepted that TRIM25 plays a role in antiviral immunity by ubiquitylating RIG-I and thus positively modulating this pathway, the majority of these studies rely on TRIM25 overexpression [265-267]. Of note, recent data using genetic approaches indicate that endogenous TRIM25 is not required for the ubiquitylation of RIG-I [289]. Nonetheless, the fact that mice with a global deletion of *Trim25* do exhibit greater susceptibility to *in vivo* IAV infection, suggests that there may be an alternative role for TRIM25 in antiviral host defense [289]. In light of my contradictory results, it is unlikely that TRIM25 plays a significant role in regulating MLKL.

5.2.2. MLKL localization following necroptosis induction

I employed a mass spec approach to identify novel MLKL interactors. Although this did not discover any potential E3 ligase or DUB, it identified proteins of desmosome complexes, which are key mediators of cell-cell adhesions. In particular, desmosomes anchor Intermediate Filaments (IF) to the plasma membrane, forming a scaffold that provides mechanical resilience to tissues [290]. This finding raised several questions including whether MLKL is specifically directed to certain regions within the plasma membrane.

Immunofluorescence experiments showed that the accumulation of phosphorylated MLKL occurred predominantly at sites of contact with neighbouring cells. Interestingly, a closer examination revealed that P-MLKL tends to accumulate at cell-cell contact sites, forming 'ring-like' structures. These structures are reminiscent of 'actin rings' which play key roles in various developmental and physiological processes. For example, actomyosin rings can trigger cytokinesis during cell division [291] and mediate the extrusion of apoptotic bodies or oncogene expressing cells from epithelia [292, 293]. Non-constricting actin ring-like structures have been described to form at cell-cell contact sites [294, 295]. In this setting, actin dynamics has a role in positively regulating the strength of cell-cell adhesions. Given the immunofluorescence images of P-MLKL, it will be interesting to investigate whether actin rings influence the localisation of P-MLKL. Likewise, the interaction of MLKL with desmosomal proteins and cadherins should be studied further.

Purified MLKL preferentially binds to certain lipids, including phosphatidylinositol species (PI) and triggers plasma membrane disruption in defined *in vitro* liposome systems [189, 194, 195, 296]. Additionally, two lipid kinases, Inositol Polyphosphate Multikinase (IPMK) and Inositol-Tetrakisphosphate-1kinase (ITPK1) were reported to function as essential auxiliary proteins in human necroptosis via synthesising highly phosphorylated forms of Inositol phosphate [297]. Thus, considering that lipid composition at the plasma membrane might predispose membranes to be targeted by MLKL, it is entirely possible that

modification of plasma membrane composition at cell-cell contact sites by lipid kinases and scramblases could regulate necroptotic signalling.

Interestingly, membrane embedded ring-like structures have been found to be formed by cell-death proteins, such as GASDERMIN-D (GSDMD), within the plasma membrane [298] or BAX in the mitochondrial outer membrane [299, 300]. In both cases, this structure delineates the formation of pores to allow permeabilization of membrane structures. Of note, BAX oligomers display a wide distribution of sizes, ranging from a few tens of nm to 100 nm in diameter. On the other hand, GSDMD ring-like oligomers have an average diameter of 22.6 nm [298, 301]. In contrast, the size of P-MLKL rings is considerably larger (5-8 μm), and tends to be determined by the area of contact with the neighbouring cells.

Lastly, the observation that P-MLKL localises to cell-cell contact sites raises the question of its functional consequence. One hypothesis is that the necroptotic ‘death signal’ can be transmitted from one cell to its neighbour, potentially accelerating the kinetics of cell death. The experimental approach to investigate the aforementioned hypothesis is provided in Section 5.3.3.

5.3. Future Directions

5.3.1. Biological Significance of MLKL Ubiquitylation

Physiologically, necroptosis is important to limit pathogen infection. Accordingly, *Ripk3*$^{-/-}$ and *Mlkl*$^{-/-}$ mice acutely susceptible viral infection [142, 176, 217, 218]. Additionally, several pathogens have evolved strategies to counteract RIPK3-mediated necroptosis [175, 176, 223, 225]. These observations strongly suggest that necroptosis acts as part of an intrinsic host defence mechanism against viruses. Therefore, I will be evaluating the susceptibility of MLKL K219R animals to infections by Murine Cytomegalovirus (MCMV).

MCMV encodes several proteins that supress cell death. The viral Inhibitor of Caspase Activation (vICA) directly targets caspase-8, thus compromising extrinsic apoptosis [302]. In addition, MCMV also encodes the viral protein M45, capable of directly inhibiting necroptosis [176]. M45-dependent inhibition of necroptosis is mediated through its RHIM-like domain. M45 promote pathogenesis by preventing the engagement of necroptosis in infected cells, allowing viral replication. Consequently, a genetically modified strain harbouring mutations in M45 RHIM-like domain (MCMV^{mutRHIM} virus) is unable to replicate and establish a productive infection in WT mice [176]. In contrast, WT mice succumb if infected with MCMV^{WT} virus [176]. Infection of *Ripk3*$^{-/-}$ mice or RIPK3 kinase-dead knockin mice with MCMV^{mutRHIM} virus results in the normalization of virus pathogenesis due to the inability to trigger necroptosis [176]. Similarly, *Mlkl*$^{-/-}$ and *Zbp1*$^{-/-}$ mice also present impaired ability to clear the virus following M45mutRHIM infection [218, 226]. These results demonstrate the requirement of ZBP1, RIPK3 and MLKL in limiting MCMV^{mutRHIM} viral replication via engagement of the necroptotic pathway.

Given the implication of ZBP1-induced necroptosis in MCMV pathogenesis, I will investigate in future studies the susceptibility of *Mlkl*^{K219R} mice to MCMV^{mutRHIM} infection. This can easily be tested by using a model for systemic infection with MCMV, where the MCMV^{mutRHIM} virus is delivered by intraperitoneal (IP) injection and the titre of the virus measured in the spleen 4 days after the infection. This

experiment will be performed in collaboration with Prof. Jan Rehwinkel, who has expertise with this experimental model [218].

In addition to MCMV, other viruses such as Herpes Simples Viruses 1 and 2 (HSV-1 and HSV-2) also counteract RIPK3-driven necroptosis. HSV encodes the RHIM-interfering proteins ICP6 and ICP10 [173, 224].Because mice are the natural host for MCMV I will focus on this virus.

5.3.2. Further mechanistic investigation of MLKL localization

I have determined that P-MLKL forms ring-like structures at cell-cell contact sites (Section 4.3). Additionally, several proteins of the desmosome adhesion complex copurified with MLKL under necroptotic conditions. Future studies should focus on validating this interaction and studying its potential role in mediating MLKL recruitment to cell-cell contact sites. To this end, siRNA-mediated known of demosomal proteins, as well as other proteins involved in cell-cell adhesion could be performed to evaluate the requirement of cell-cell adhesions for the assembly of P-MLKL molecules into a ring-like shape. Additionally, this can also be tested by investigating the colocalization of desmosomal proteins and P-MLKL by immunofluorescence. Lastly one could also investigate whether such rings can be formed in cells that lack any contact with neighbouring cells.

Another important aspect would be to investigate the kinetics of the P-MLKL ring formation and whether upon triggering necroptosis there is any rearrangement of the cytoskeleton that allows the trafficking of P-MLKL to the plasma membrane and/or its assembly into a ring shape. To study this, drugs that affect the cytoskeleton dynamics could be employed in conjunction with immunofluorescence approaches. As previously described, it is possible that actin rings might help in the organization of certain key MLKL interactors along the plasma membrane. Such is the case for neurons, where actin rings are thought to help in the organization of certain proteins along the axolemma, the plasma membrane surrounding the axon [303].

Finally, it will be important to evaluate the functional consequence of the ring-like localization of P-MLKL. Given that this occurs at cell-cell contact sites, it is tempting to speculate that the localisation of P-MLKL serves as a means of communication between cells. From a biological perspective, this might be relevant to enhance the kinetics of cell death execution to combat viral spreading. To test this, it will be important to interfere with the desmosomal localization of P-MLKL and evaluate its consequence. This could be tested using siRNA-mediated knockdown approaches or through pharmacological inhibition. Furthermore, it could also be investigated whether a cell undergoing necroptosis could induce the death of a neighbouring cell in which the pathway cannot be triggered. Experimentally, this can be tested by co-culturing *Mlkl*$^{WT/WT}$ and *Mlkl*$^{-/-}$ cells, followed by treatment with TSZ. The ability of a WT cell to induce the death of adjacent *Mlkl*$^{-/-}$ cells could be assessed by immunofluorescence analysis. Testing these hypotheses might add an extra layer of complexity to the necroptotic pathway.

6. Appendices

6.1. Supplementary Figures

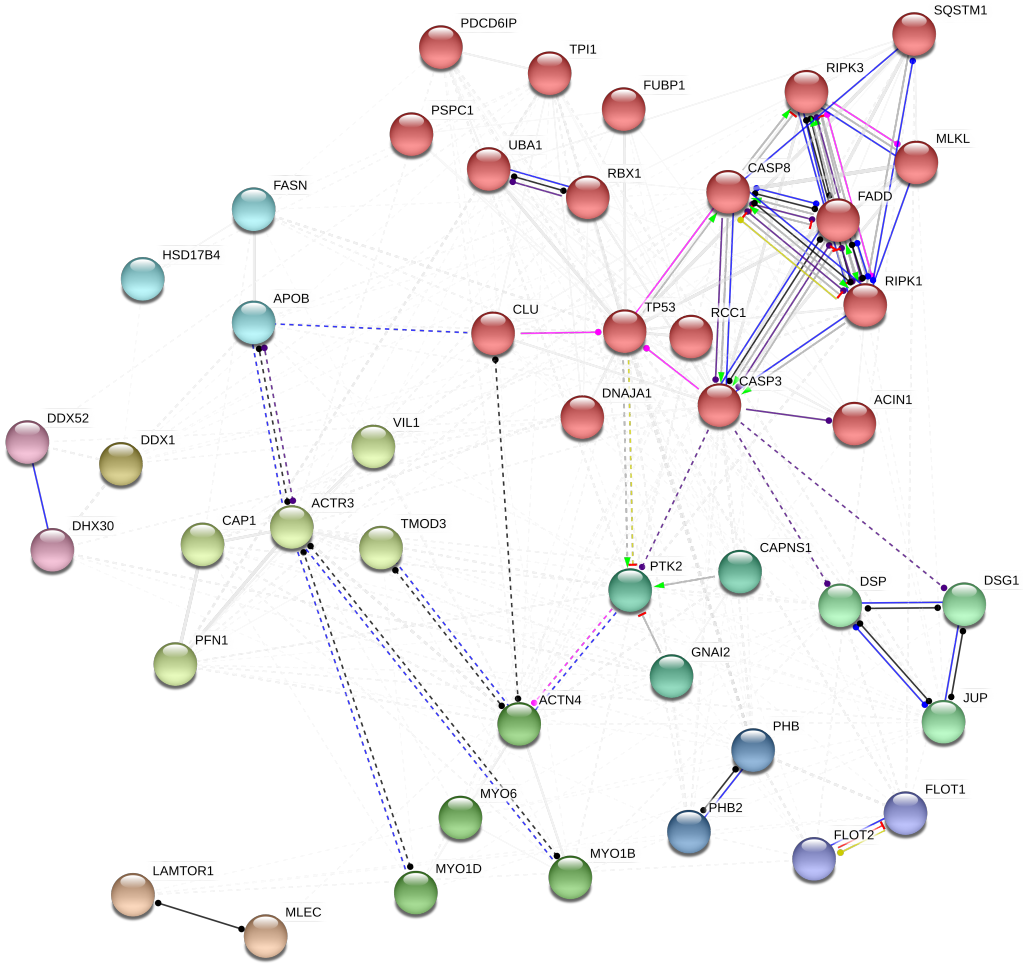

Figure 6.1. MLKL Interactome Network Analysis

The mass-spec experiment described in Section 4.2.B was processed for pathway analysis. Dr. Arnaud Legrand from the Meier Lab processed the raw data using the STRING platform to generate the MLKL interactome network. Interestingly, the pathway analysis shows interactions with desmosomal proteins (desmoplakin (DSP), desmoglein 1 (DSG1), junction plakoglobin (JUP) as well as other proteins reported to regulate MLKL, such as flotillin-1/2 (FLOT1/2) [200, 268].

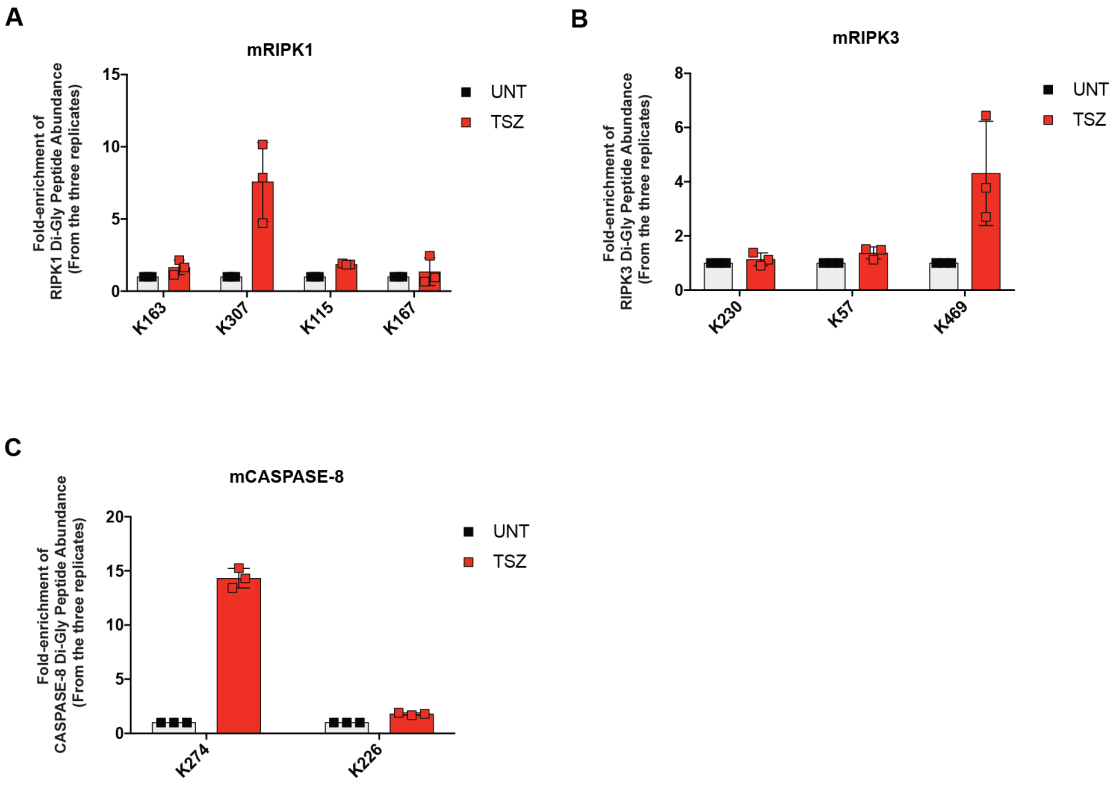

Figure 6.2. Di-Gly peptides identified for RIPK1, RIPK3 and CASPASE-8.

Fold-enrichment upon treatment with TSZ for each di-Gly peptide abundance for proteins RIPK1 (A), RIPK3 (B) and CASPASE-8 (C). Data corresponds to the experiment described in Figure 3.9. The di-Gly peptide abundance in TSZ-treated samples was normalised to the correspondent untreated control. Each dot represents the abundance of the di-Gly peptide in each biological replicate. Error bars indicate SD. Dr. Lu Yu performed the LC-MS/MS experiment, including the identification of the di-Gly peptides and the quantification of peptide abundance.

6.2. Publications

During my PhD I have also contributed to the following published articles:

RIPK1 and Caspase-8 Ensure Chromosome Stability Independently of Their Role in Cell Death and Inflammation. Molecular Cell 2019.

Gianmaria Liccardi, ***Laura Ramos Garcia****, Tencho Tenev, Alessandro Annibaldi, Arnaud J. Legrand, David Robertson, Rebecca Feltham, Holly Anderton, Maurice Darding, Nieves Peltzer, Marius Dannappel, Hannah Schünke, Luca L. Fava, Manuel D.Haschka, Timo Glatter, Alexey Nesvizhskii, Alexander Schmidt, Philip A.Harris, Philip A.Harris ,John Bertin, PeterJ. Gough, Andreas Villunger, John Silke, Manolis Pasparakis, Katiuscia Bianchi, Pascal Meier.*

Identification and Characterization of Novel Receptor-Interacting Serine/Threonine-Protein Kinase 2 Inhibitors Using Structural Similarity Analysis. The Journal of Pharmacology and Experimental Therapeutics. 2018.

Mohamed Salla, Rodrigo Aguayo-Ortiz, Gaddafi I. Danmaliki, Alaa Zare, Ahmed Said, Jack Moore, Vrajeshkumar Pandya, Robin Manaloor, Sunny Fong, Anna R. Blankstein, Spencer B. Gibson, ***Laura Ramos Garcia****, Pascal Meier, Khushwant S. Bhullar, Basil P. Hubbard, Yahya Fiteh, Harissios Vliagoftis, Ing Swie Goping, Dion Brocks, Peter Hwang, Carlos A. Velázquez-Martínez and Shairaz Baksh*

References

1. Prus, G., et al., *Analysis and Interpretation of Protein Post-Translational Modification Site Stoichiometry.* Trends Biochem Sci, 2019.
2. Hornbeck, P.V., et al., *PhosphoSitePlus, 2014: mutations, PTMs and recalibrations.* Nucleic Acids Res, 2015. **43**(Database issue): p. D512-20.
3. Deribe, Y.L., T. Pawson, and I. Dikic, *Post-translational modifications in signal integration.* Nat Struct Mol Biol, 2010. **17**(6): p. 666-72.
4. Khoury, G.A., R.C. Baliban, and C.A. Floudas, *Proteome-wide post-translational modification statistics: frequency analysis and curation of the swiss-prot database.* Sci Rep, 2011. **1**.
5. Clague, M.J., S. Urbe, and D. Komander, *Breaking the chains: deubiquitylating enzyme specificity begets function.* Nat Rev Mol Cell Biol, 2019.
6. Ciechanover, A., et al., *ATP-dependent conjugation of reticulocyte proteins with the polypeptide required for protein degradation.* Proc Natl Acad Sci U S A, 1980. **77**(3): p. 1365-8.
7. Wilkinson, K.D., M.K. Urban, and A.L. Haas, *Ubiquitin is the ATP-dependent proteolysis factor I of rabbit reticulocytes.* J Biol Chem, 1980. **255**(16): p. 7529-32.
8. Hershko, A., et al., *Proposed role of ATP in protein breakdown: conjugation of protein with multiple chains of the polypeptide of ATP-dependent proteolysis.* Proc Natl Acad Sci U S A, 1980. **77**(4): p. 1783-6.
9. Grabbe, C., K. Husnjak, and I. Dikic, *The spatial and temporal organization of ubiquitin networks.* Nat Rev Mol Cell Biol, 2011. **12**(5): p. 295-307.
10. Komander, D. and M. Rape, *The ubiquitin code.* Annu Rev Biochem, 2012. **81**: p. 203-29.
11. Pickart, C.M., *Mechanisms underlying ubiquitination.* Annu Rev Biochem, 2001. **70**: p. 503-33.
12. Buetow, L. and D.T. Huang, *Structural insights into the catalysis and regulation of E3 ubiquitin ligases.* Nat Rev Mol Cell Biol, 2016. **advance online publication**.
13. Rape, M., *Ubiquitylation at the crossroads of development and disease.* Nat Rev Mol Cell Biol, 2018. **19**(1): p. 59-70.
14. Yau, R. and M. Rape, *The increasing complexity of the ubiquitin code.* Nat Cell Biol, 2016. **18**(6): p. 579-86.
15. Trempe, J.F., *Reading the ubiquitin postal code.* Curr Opin Struct Biol, 2011. **21**(6): p. 792-801.
16. Kirisako, T., et al., *A ubiquitin ligase complex assembles linear polyubiquitin chains.* Embo j, 2006. **25**(20): p. 4877-87.
17. Yau, R. and M. Rape, *The increasing complexity of the ubiquitin code.* Nat Cell Biol, 2016. **18**(6): p. 579-586.

18. Hrdinka, M. and M. Gyrd-Hansen, *The Met1-Linked Ubiquitin Machinery: Emerging Themes of (De)regulation.* Mol Cell, 2017. **68**(2): p. 265-280.

19. Swatek, K.N. and D. Komander, *Ubiquitin modifications.* Cell Res, 2016. **26**(4): p. 399-422.

20. Vijay-Kumar, S., C.E. Bugg, and W.J. Cook, *Structure of ubiquitin refined at 1.8 A resolution.* J Mol Biol, 1987. **194**(3): p. 531-44.

21. Jin, J., et al., *Dual E1 activation systems for ubiquitin differentially regulate E2 enzyme charging.* Nature, 2007. **447**(7148): p. 1135-8.

22. Ye, Y. and M. Rape, *Building ubiquitin chains: E2 enzymes at work.* Nat Rev Mol Cell Biol, 2009. **10**(11): p. 755-64.

23. Markson, G., et al., *Analysis of the human E2 ubiquitin conjugating enzyme protein interaction network.* Genome Res, 2009. **19**(10): p. 1905-11.

24. Mattern, M., et al., *Using Ubiquitin Binders to Decipher the Ubiquitin Code.* Trends Biochem Sci, 2019. **44**(7): p. 599-615.

25. Lee, I. and H. Schindelin, *Structural insights into E1-catalyzed ubiquitin activation and transfer to conjugating enzymes.* Cell, 2008. **134**(2): p. 268-78.

26. Schulman, B.A. and J.W. Harper, *Ubiquitin-like protein activation by E1 enzymes: the apex for downstream signalling pathways.* Nat Rev Mol Cell Biol, 2009. **10**(5): p. 319-31.

27. Stewart, M.D., et al., *E2 enzymes: more than just middle men.* Cell Res, 2016. **26**(4): p. 423-40.

28. Eddins, M.J., et al., *Mms2-Ubc13 covalently bound to ubiquitin reveals the structural basis of linkage-specific polyubiquitin chain formation.* Nat Struct Mol Biol, 2006. **13**(10): p. 915-20.

29. Buetow, L. and D.T. Huang, *Structural insights into the catalysis and regulation of E3 ubiquitin ligases.* Nat Rev Mol Cell Biol, 2016. **17**(10): p. 626-42.

30. Deshaies, R.J. and C.A. Joazeiro, *RING domain E3 ubiquitin ligases.* Annu Rev Biochem, 2009. **78**: p. 399-434.

31. Rotin, D. and S. Kumar, *Physiological functions of the HECT family of ubiquitin ligases.* Nat Rev Mol Cell Biol, 2009. **10**(6): p. 398-409.

32. Spratt, D.E., H. Walden, and G.S. Shaw, *RBR E3 ubiquitin ligases: new structures, new insights, new questions.* Biochem J, 2014. **458**(3): p. 421-37.

33. Dikic, I., S. Wakatsuki, and K.J. Walters, *Ubiquitin-binding domains - from structures to functions.* Nat Rev Mol Cell Biol, 2009. **10**(10): p. 659-71.

34. Kulathu, Y. and D. Komander, *Atypical ubiquitylation — the unexplored world of polyubiquitin beyond Lys48 and Lys63 linkages.* Nat Rev Mol Cell Biol, 2012. **13**(8): p. 508-523.

35. Komander, D., et al., *Molecular discrimination of structurally equivalent Lys 63-linked and linear polyubiquitin chains.* EMBO Rep, 2009. **10**(5): p. 466-73.

36. Lange, O.F., et al., *Recognition dynamics up to microseconds revealed from an RDC-derived ubiquitin ensemble in solution.* Science, 2008. **320**(5882): p. 1471-5.

37. Sims, J.J. and R.E. Cohen, *Linkage-specific avidity defines the lysine 63-linked polyubiquitin-binding preference of rap80.* Mol Cell, 2009. **33**(6): p. 775-83.

38. Sato, Y., et al., *Structural basis for specific cleavage of Lys 63-linked polyubiquitin chains.* Nature, 2008. **455**(7211): p. 358-62.

39. Newton, K., et al., *Ubiquitin chain editing revealed by polyubiquitin linkage-specific antibodies.* Cell, 2008. **134**(4): p. 668-78.

40. Cook, W.J., et al., *Structure of a diubiquitin conjugate and a model for interaction with ubiquitin conjugating enzyme (E2).* J Biol Chem, 1992. **267**(23): p. 16467-71.

41. Ryabov, Y. and D. Fushman, *Interdomain mobility in di-ubiquitin revealed by NMR.* Proteins, 2006. **63**(4): p. 787-96.

42. Castaneda, C.A., et al., *Unique structural, dynamical, and functional properties of k11-linked polyubiquitin chains.* Structure, 2013. **21**(7): p. 1168-81.

43. Thrower, J.S., et al., *Recognition of the polyubiquitin proteolytic signal.* Embo j, 2000. **19**(1): p. 94-102.

44. Lu, Y., et al., *Substrate degradation by the proteasome: a single-molecule kinetic analysis.* Science, 2015. **348**(6231): p. 1250834.

45. Flick, K., et al., *Proteolysis-independent regulation of the transcription factor Met4 by a single Lys 48-linked ubiquitin chain.* Nat Cell Biol, 2004. **6**(7): p. 634-41.

46. Chen, Z.J. and L.J. Sun, *Nonproteolytic functions of ubiquitin in cell signaling.* Mol Cell, 2009. **33**(3): p. 275-86.

47. Oh, E., D. Akopian, and M. Rape, *Principles of Ubiquitin-Dependent Signaling.* Annu Rev Cell Dev Biol, 2018. **34**: p. 137-162.

48. Tokunaga, F., et al., *Involvement of linear polyubiquitylation of NEMO in NF-kappaB activation.* Nat Cell Biol, 2009. **11**(2): p. 123-32.

49. Damgaard, R.B., et al., *The ubiquitin ligase XIAP recruits LUBAC for NOD2 signaling in inflammation and innate immunity.* Mol Cell, 2012. **46**(6): p. 746-58.

50. Haas, T.L., et al., *Recruitment of the linear ubiquitin chain assembly complex stabilizes the TNF-R1 signaling complex and is required for TNF-mediated gene induction.* Mol Cell, 2009. **36**(5): p. 831-44.

51. Rahighi, S., et al., *Specific recognition of linear ubiquitin chains by NEMO is important for NF-kappaB activation.* Cell, 2009. **136**(6): p. 1098-109.

52. Kanayama, A., et al., *TAB2 and TAB3 activate the NF-kappaB pathway through binding to polyubiquitin chains.* Mol Cell, 2004. **15**(4): p. 535-48.

53. Grice, G.L., et al., *The Proteasome Distinguishes between Heterotypic and Homotypic Lysine-11-Linked Polyubiquitin Chains.* Cell Rep, 2015. **12**(4): p. 545-53.

54. Meyer, H.J. and M. Rape, *Enhanced protein degradation by branched ubiquitin chains.* Cell, 2014. **157**(4): p. 910-21.

55. Min, M., et al., *Efficient APC/C substrate degradation in cells undergoing mitotic exit depends on K11 ubiquitin linkages.* Mol Biol Cell, 2015. **26**(24): p. 4325-32.

56. Michel, M.A., et al., *Ubiquitin Linkage-Specific Affimers Reveal Insights into K6-Linked Ubiquitin Signaling.* Mol Cell, 2017. **68**(1): p. 233-246.e5.

57. Dammer, E.B., et al., *Polyubiquitin linkage profiles in three models of proteolytic stress suggest the etiology of Alzheimer disease.* J Biol Chem, 2011. **286**(12): p. 10457-65.

58. Geisler, S., et al., *PINK1/Parkin-mediated mitophagy is dependent on VDAC1 and p62/SQSTM1.* Nat Cell Biol, 2010. **12**(2): p. 119-31.

59. Tran, H., et al., *Trabid, a new positive regulator of Wnt-induced transcription with preference for binding and cleaving K63-linked ubiquitin chains.* Genes Dev, 2008. **22**(4): p. 528-42.

60. Jin, J., et al., *Epigenetic regulation of the expression of Il12 and Il23 and autoimmune inflammation by the deubiquitinase Trabid.* Nat Immunol, 2016. **17**(3): p. 259-68.

61. Yuan, W.C., et al., *K33-Linked Polyubiquitination of Coronin 7 by Cul3-KLHL20 Ubiquitin E3 Ligase Regulates Protein Trafficking.* Mol Cell, 2014. **54**(4): p. 586-600.

62. Emmerich, C.H., et al., *Activation of the canonical IKK complex by K63/M1-linked hybrid ubiquitin chains.* Proc Natl Acad Sci U S A, 2013. **110**(38): p. 15247-52.

63. Ohtake, F., et al., *Ubiquitin acetylation inhibits polyubiquitin chain elongation.* EMBO Rep, 2015. **16**(2): p. 192-201.

64. Nakagawa, T. and K. Nakayama, *Protein monoubiquitylation: targets and diverse functions.* Genes Cells, 2015. **20**(7): p. 543-62.

65. Sasaki, A.T., et al., *Ubiquitination of K-Ras enhances activation and facilitates binding to select downstream effectors.* Sci Signal, 2011. **4**(163): p. ra13.

66. Chovatiya, R. and R. Medzhitov, *Stress, inflammation, and defense of homeostasis.* Mol Cell, 2014. **54**(2): p. 281-8.

67. Chen, G.Y. and G. Nunez, *Sterile inflammation: sensing and reacting to damage.* Nat Rev Immunol, 2010. **10**(12): p. 826-37.

68. Mowat, A.M., C.L. Scott, and C.C. Bain, *Barrier-tissue macrophages: functional adaptation to environmental challenges.* Nat Med, 2017. **23**(11): p. 1258-1270.

69. Takeuchi, O. and S. Akira, *Pattern recognition receptors and inflammation.* Cell, 2010. **140**(6): p. 805-20.

70. Paludan, S.R., L.S. Reinert, and V. Hornung, *DNA-stimulated cell death: implications for host defence, inflammatory diseases and cancer.* Nat Rev Immunol, 2019. **19**(3): p. 141-153.

71. Nathan, C. and A. Ding, *Nonresolving inflammation.* Cell, 2010. **140**(6): p. 871-82.

72. Wallach, D., T.B. Kang, and A. Kovalenko, *Concepts of tissue injury and cell death in inflammation: a historical perspective.* Nat Rev Immunol, 2014. **14**(1): p. 51-9.

73. Laster, S.M., J.G. Wood, and L.R. Gooding, *Tumor necrosis factor can induce both apoptic and necrotic forms of cell lysis.* J Immunol, 1988. **141**(8): p. 2629-34.

74. Engelmann, H., et al., *Antibodies to a soluble form of a tumor necrosis factor (TNF) receptor have TNF-like activity.* J Biol Chem, 1990. **265**(24): p. 14497-504.

75. Yatim, N., S. Cullen, and M.L. Albert, *Dying cells actively regulate adaptive immune responses.* Nat Rev Immunol, 2017. **17**(4): p. 262-275.

76. Yatim, N., et al., *RIPK1 and NF-κB signaling in dying cells determines cross-priming of CD8⁺ T cells.* Science, 2015. **350**(6258): p. 328-34.

77. Kroemer, G., et al., *Immunogenic cell death in cancer therapy.* Annu Rev Immunol, 2013. **31**: p. 51-72.

78. Yatim, N., et al., *RIPK1 and NF-kappaB signaling in dying cells determines cross-priming of CD8(+) T cells.* Science, 2015. **350**(6258): p. 328-34.

79. Galluzzi, L., et al., *Molecular mechanisms of cell death: recommendations of the Nomenclature Committee on Cell Death 2018.* Cell Death Differ, 2018. **25**(3): p. 486-541.

80. Galluzzi, L., et al., *Cell death modalities: classification and pathophysiological implications.* Cell Death Differ, 2007. **14**(7): p. 1237-43.

81. Green, D.R., et al., *Immunogenic and tolerogenic cell death.* Nat Rev Immunol, 2009. **9**(5): p. 353-63.

82. Virchow, R., *Cellular pathology. As based upon physiological and pathological histology. Lecture XVI--Atheromatous affection of arteries. 1858.* Nutr Rev, 1989. **47**(1): p. 23-5.

83. Degterev, A., et al., *Chemical inhibitor of nonapoptotic cell death with therapeutic potential for ischemic brain injury.* Nat Chem Biol, 2005. **1**(2): p. 112-9.

84. Degterev, A., et al., *Identification of RIP1 kinase as a specific cellular target of necrostatins.* Nat Chem Biol, 2008. **4**(5): p. 313-21.

85. Soung, Y.H., et al., *Caspase-8 gene is frequently inactivated by the frameshift somatic mutation 1225_1226delTG in hepatocellular carcinomas.* Oncogene, 2005. **24**(1): p. 141-7.

86. Teitz, T., et al., *Caspase 8 is deleted or silenced preferentially in childhood neuroblastomas with amplification of MYCN.* Nat Med, 2000. **6**(5): p. 529-35.

87. Hopkins-Donaldson, S., et al., *Silencing of death receptor and caspase-8 expression in small cell lung carcinoma cell lines and tumors by DNA methylation.* Cell Death Differ, 2003. **10**(3): p. 356-64.

88. Tait, S.W., G. Ichim, and D.R. Green, *Die another way--non-apoptotic mechanisms of cell death.* J Cell Sci, 2014. **127**(Pt 10): p. 2135-44.

89. Pearson, J.S. and J.M. Murphy, *Down the rabbit hole: Is necroptosis truly an innate response to infection?* Cell Microbiol, 2017. **19**(8).

90. Nogusa, S., et al., *RIPK3 Activates Parallel Pathways of MLKL-Driven Necroptosis and FADD-Mediated Apoptosis to Protect against Influenza A Virus.* Cell Host Microbe, 2016. **20**(1): p. 13-24.

91. Dannappel, M., et al., *RIPK1 maintains epithelial homeostasis by inhibiting apoptosis and necroptosis.* Nature, 2014. **513**(7516): p. 90-4.

92. Takahashi, N., et al., *RIPK1 ensures intestinal homeostasis by protecting the epithelium against apoptosis.* Nature, 2014. **513**(7516): p. 95-9.

93. Vanamee, E.S. and D.L. Faustman, *Structural principles of tumor necrosis factor superfamily signaling.* Sci Signal, 2018. **11**(511).

94. Locksley, R.M., N. Killeen, and M.J. Lenardo, *The TNF and TNF receptor superfamilies: integrating mammalian biology.* Cell, 2001. **104**(4): p. 487-501.

95. Walczak, H., *Death receptor-ligand systems in cancer, cell death, and inflammation.* Cold Spring Harb Perspect Biol, 2013. **5**(5): p. a008698.

96. Yi, F., et al., *Beyond Cell Death: New Functions for TNF Family Cytokines in Autoimmunity and Tumor Immunotherapy.* Trends Mol Med, 2018. **24**(7): p. 642-653.

97. Itoh, N., et al., *The polypeptide encoded by the cDNA for human cell surface antigen Fas can mediate apoptosis.* Cell, 1991. **66**(2): p. 233-43.

98. Sheridan, J.P., et al., *Control of TRAIL-induced apoptosis by a family of signaling and decoy receptors.* Science, 1997. **277**(5327): p. 818-21.

99. Pobezinskaya, Y.L. and Z. Liu, *The role of TRADD in death receptor signaling.* Cell Cycle, 2012. **11**(5): p. 871-6.

100. Ward-Kavanagh, L.K., et al., *The TNF Receptor Superfamily in Co-stimulating and Co-inhibitory Responses.* Immunity, 2016. **44**(5): p. 1005-19.

101. Black, R.A., et al., *A metalloproteinase disintegrin that releases tumour-necrosis factor-alpha from cells.* Nature, 1997. **385**(6618): p. 729-33.

102. Richter, C., et al., *The tumor necrosis factor receptor stalk regions define responsiveness to soluble versus membrane-bound ligand.* Mol Cell Biol, 2012. **32**(13): p. 2515-29.

103. Micheau, O. and J. Tschopp, *Induction of TNF receptor I-mediated apoptosis via two sequential signaling complexes.* Cell, 2003. **114**(2): p. 181-90.

104. Annibaldi, A. and P. Meier, *Checkpoints in TNF-Induced Cell Death: Implications in Inflammation and Cancer.* Trends Mol Med, 2018. **24**(1): p. 49-65.

105. Hsu, H., J. Xiong, and D.V. Goeddel, *The TNF receptor 1-associated protein TRADD signals cell death and NF-kappa B activation.* Cell, 1995. **81**(4): p. 495-504.

106. Kelliher, M.A., et al., *The death domain kinase RIP mediates the TNF-induced NF-kappaB signal.* Immunity, 1998. **8**(3): p. 297-303.

107. Hsu, H., et al., *TNF-dependent recruitment of the protein kinase RIP to the TNF receptor-1 signaling complex.* Immunity, 1996. **4**(4): p. 387-96.

108. Stanger, B.Z., et al., *RIP: a novel protein containing a death domain that interacts with Fas/APO-1 (CD95) in yeast and causes cell death.* Cell, 1995. **81**(4): p. 513-23.

109. Rothe, M., et al., *The TNFR2-TRAF signaling complex contains two novel proteins related to baculoviral inhibitor of apoptosis proteins.* Cell, 1995. **83**(7): p. 1243-52.

110. Ermolaeva, M.A., et al., *Function of TRADD in tumor necrosis factor receptor 1 signaling and in TRIF-dependent inflammatory responses.* Nat Immunol, 2008. **9**(9): p. 1037-46.

111. Gyrd-Hansen, M. and P. Meier, *IAPs: from caspase inhibitors to modulators of NF-kappaB, inflammation and cancer.* Nat Rev Cancer, 2010. **10**(8): p. 561-74.

112. Vince, J.E., et al., *TRAF2 must bind to cellular inhibitors of apoptosis for tumor necrosis factor (tnf) to efficiently activate nf-{kappa}b and to prevent tnf-induced apoptosis.* J Biol Chem, 2009. **284**(51): p. 35906-15.

113. Annibaldi, A., et al., *Ubiquitin-Mediated Regulation of RIPK1 Kinase Activity Independent of IKK and MK2.* Mol Cell, 2018. **69**(4): p. 566-580.e5.

114. Witt, A. and D. Vucic, *Diverse ubiquitin linkages regulate RIP kinases-mediated inflammatory and cell death signaling.* Cell Death Differ, 2017. **24**(7): p. 1160-1171.

115. Gerlach, B., et al., *Linear ubiquitination prevents inflammation and regulates immune signalling.* Nature, 2011. **471**(7340): p. 591-6.

116. Ikeda, F., et al., *SHARPIN forms a linear ubiquitin ligase complex regulating NF-kappaB activity and apoptosis.* Nature, 2011. **471**(7340): p. 637-41.

117. Zhang, J., et al., *An unexpected twist to the activation of IKKbeta: TAK1 primes IKKbeta for activation by autophosphorylation.* Biochem J, 2014. **461**(3): p. 531-7.

118. Mathes, E., et al., *NF-kappaB dictates the degradation pathway of IkappaBalpha.* Embo j, 2008. **27**(9): p. 1357-67.

119. Ajibade, A.A., H.Y. Wang, and R.F. Wang, *Cell type-specific function of TAK1 in innate immune signaling.* Trends Immunol, 2013. **34**(7): p. 307-16.

120. Wang, C., et al., *TAK1 is a ubiquitin-dependent kinase of MKK and IKK.* Nature, 2001. **412**(6844): p. 346-51.

121. Wong, W.W., et al., *RIPK1 is not essential for TNFR1-induced activation of NF-kappaB.* Cell Death Differ, 2010. **17**(3): p. 482-7.

122. Ori, D., et al., *Essential roles of K63-linked polyubiquitin-binding proteins TAB2 and TAB3 in B cell activation via MAPKs.* J Immunol, 2013. **190**(8): p. 4037-45.

123. Micheau, O., et al., *NF-kappaB signals induce the expression of c-FLIP.* Mol Cell Biol, 2001. **21**(16): p. 5299-305.

124. Moulin, M., et al., *IAPs limit activation of RIP kinases by TNF receptor 1 during development.* Embo j, 2012. **31**(7): p. 1679-91.

125. Peltzer, N., et al., *HOIP deficiency causes embryonic lethality by aberrant TNFR1-mediated endothelial cell death.* Cell Rep, 2014. **9**(1): p. 153-65.

126. Bertrand, M.J., et al., *cIAP1 and cIAP2 facilitate cancer cell survival by functioning as E3 ligases that promote RIP1 ubiquitination.* Mol Cell, 2008. **30**(6): p. 689-700.

127. Varfolomeev, E., et al., *c-IAP1 and c-IAP2 are critical mediators of tumor necrosis factor alpha (TNFalpha)-induced NF-kappaB activation.* J Biol Chem, 2008. **283**(36): p. 24295-9.

128. Feltham, R., et al., *Mind Bomb Regulates Cell Death during TNF Signaling by Suppressing RIPK1's Cytotoxic Potential.* Cell Rep, 2018. **23**(2): p. 470-484.

129. Elliott, P.R., et al., *SPATA2 Links CYLD to LUBAC, Activates CYLD, and Controls LUBAC Signaling.* Mol Cell, 2016. **63**(6): p. 990-1005.

130. Kupka, S., et al., *SPATA2-Mediated Binding of CYLD to HOIP Enables CYLD Recruitment to Signaling Complexes.* Cell Rep, 2016.

131. Wagner, S.A., et al., *SPATA2 links CYLD to the TNF-alpha receptor signaling complex and modulates the receptor signaling outcomes.* Embo j, 2016. **35**(17): p. 1868-84.

132. Schlicher, L., et al., *SPATA2 promotes CYLD activity and regulates TNF-induced NF-kappaB signaling and cell death.* EMBO Rep, 2016. **17**(10): p. 1485-1497.

133. Hrdinka, M., et al., *CYLD Limits Lys63- and Met1-Linked Ubiquitin at Receptor Complexes to Regulate Innate Immune Signaling.* Cell Rep, 2016. **14**(12): p. 2846-58.

134. Harhaj, E.W. and V.M. Dixit, *Regulation of NF-kappaB by deubiquitinases.* Immunol Rev, 2012. **246**(1): p. 107-24.

135. Dondelinger, Y., P. Vandenabeele, and M.J. Bertrand, *Regulation of RIPK1's cell death function by phosphorylation.* Cell Cycle, 2016. **15**(1): p. 5-6.

136. Dondelinger, Y., et al., *MK2 phosphorylation of RIPK1 regulates TNF-mediated cell death.* Nat Cell Biol, 2017. **19**(10): p. 1237-1247.

137. Jaco, I., et al., *MK2 Phosphorylates RIPK1 to Prevent TNF-Induced Cell Death.* Mol Cell, 2017. **66**(5): p. 698-710.e5.

138. Menon, M.B., et al., *p38(MAPK)/MK2-dependent phosphorylation controls cytotoxic RIPK1 signalling in inflammation and infection.* Nat Cell Biol, 2017. **19**(10): p. 1248-1259.

139. Dondelinger, Y., et al., *NF-kappaB-Independent Role of IKKalpha/IKKbeta in Preventing RIPK1 Kinase-Dependent Apoptotic and Necroptotic Cell Death during TNF Signaling.* Mol Cell, 2015. **60**(1): p. 63-76.

140. Dondelinger, Y., et al., *Serine 25 phosphorylation inhibits RIPK1 kinase-dependent cell death in models of infection and inflammation.* Nat Commun, 2019. **10**(1): p. 1729.

141. Lafont, E., et al., *TBK1 and IKKepsilon prevent TNF-induced cell death by RIPK1 phosphorylation.* Nat Cell Biol, 2018. **20**(12): p. 1389-1399.

142. Cho, Y.S., et al., *Phosphorylation-driven assembly of the RIP1-RIP3 complex regulates programmed necrosis and virus-induced inflammation.* Cell, 2009. **137**(6): p. 1112-23.

143. Peltzer, N., M. Darding, and H. Walczak, *Holding RIPK1 on the Ubiquitin Leash in TNFR1 Signaling.* Trends Cell Biol, 2016.

144. Zhang, D.W., et al., *RIP3, an energy metabolism regulator that switches TNF-induced cell death from apoptosis to necrosis.* Science, 2009. **325**(5938): p. 332-6.

145. Hughes, M.A., et al., *Co-operative and Hierarchical Binding of c-FLIP and Caspase-8: A Unified Model Defines How c-FLIP Isoforms Differentially Control Cell Fate.* Mol Cell, 2016. **61**(6): p. 834-49.

146. Oberst, A., et al., *Catalytic activity of the caspase-8-FLIP(L) complex inhibits RIPK3-dependent necrosis.* Nature, 2011. **471**(7338): p. 363-7.

147. Feng, S., et al., *Cleavage of RIP3 inactivates its caspase-independent apoptosis pathway by removal of kinase domain.* Cell Signal, 2007. **19**(10): p. 2056-67.

148. Zhang, X., J.P. Dowling, and J. Zhang, *RIPK1 can mediate apoptosis in addition to necroptosis during embryonic development.* Cell Death Dis, 2019. **10**(3): p. 245.

149. Newton, K., et al., *Cleavage of RIPK1 by caspase-8 is crucial for limiting apoptosis and necroptosis.* Nature, 2019.

150. O'Donnell, M.A., et al., *Caspase 8 inhibits programmed necrosis by processing CYLD.* Nat Cell Biol, 2011. **13**(12): p. 1437-42.

151. Schleich, K., et al., *Stoichiometry of the CD95 death-inducing signaling complex: experimental and modeling evidence for a death effector domain chain model.* Mol Cell, 2012. **47**(2): p. 306-19.

152. Dickens, L.S., et al., *The 'complexities' of life and death: death receptor signalling platforms.* Exp Cell Res, 2012. **318**(11): p. 1269-77.

153. Tummers, B. and D.R. Green, *Caspase-8: regulating life and death.* Immunol Rev, 2017. **277**(1): p. 76-89.

154. Varfolomeev, E.E., et al., *Targeted disruption of the mouse Caspase 8 gene ablates cell death induction by the TNF receptors, Fas/Apo1, and DR3 and is lethal prenatally.* Immunity, 1998. **9**(2): p. 267-76.

155. Zhang, J., et al., *Fas-mediated apoptosis and activation-induced T-cell proliferation are defective in mice lacking FADD/Mort1.* Nature, 1998. **392**(6673): p. 296-300.

156. Kaiser, W.J., et al., *RIP3 mediates the embryonic lethality of caspase-8-deficient mice.* Nature, 2011. **471**(7338): p. 368-72.

157. Alvarez-Diaz, S., et al., *The Pseudokinase MLKL and the Kinase RIPK3 Have Distinct Roles in Autoimmune Disease Caused by Loss of Death-Receptor-Induced Apoptosis.* Immunity, 2016.

158. Sun, X., et al., *Identification of a novel homotypic interaction motif required for the phosphorylation of receptor-interacting protein (RIP) by RIP3.* J Biol Chem, 2002. **277**(11): p. 9505-11.

159. Oerlemans, M.I., et al., *Inhibition of RIP1-dependent necrosis prevents adverse cardiac remodeling after myocardial ischemia-reperfusion in vivo.* Basic Res Cardiol, 2012. **107**(4): p. 270.

160. Li, J., et al., *The RIP1/RIP3 necrosome forms a functional amyloid signaling complex required for programmed necrosis.* Cell, 2012. **150**(2): p. 339-50.

161. Mompean, M., et al., *The Structure of the Necrosome RIPK1-RIPK3 Core, a Human Hetero-Amyloid Signaling Complex.* Cell, 2018. **173**(5): p. 1244-1253.e10.

162. Li, D. and C. Liu, *Better Together: A Hybrid Amyloid Signals Necroptosis.* Cell, 2018. **173**(5): p. 1068-1070.

163. Shaw, A.S., et al., *Kinases and pseudokinases: lessons from RAF.* Mol Cell Biol, 2014. **34**(9): p. 1538-46.

164. Taylor, S.S. and A.P. Kornev, *Protein kinases: evolution of dynamic regulatory proteins.* Trends Biochem Sci, 2011. **36**(2): p. 65-77.

165. Petrie, E.J., P.E. Czabotar, and J.M. Murphy, *The Structural Basis of Necroptotic Cell Death Signaling.* Trends Biochem Sci, 2019. **44**(1): p. 53-63.

166. Meng, H., et al., *Death-domain dimerization-mediated activation of RIPK1 controls necroptosis and RIPK1-dependent apoptosis.* Proc Natl Acad Sci U S A, 2018. **115**(9): p. E2001-e2009.

167. McQuade, T., Y. Cho, and F.K. Chan, *Positive and negative phosphorylation regulates RIP1- and RIP3-induced programmed necrosis.* Biochem J, 2013. **456**(3): p. 409-15.

168. Wu, X.N., et al., *Distinct roles of RIP1-RIP3 hetero- and RIP3-RIP3 homo-interaction in mediating necroptosis.* Cell Death Differ, 2014. **21**(11): p. 1709-20.

169. Hu, J., et al., *Kinase regulation by hydrophobic spine assembly in cancer.* Mol Cell Biol, 2015. **35**(1): p. 264-76.

170. Sun, L., et al., *Mixed lineage kinase domain-like protein mediates necrosis signaling downstream of RIP3 kinase.* Cell, 2012. **148**(1-2): p. 213-27.

171. Chen, W., et al., *Diverse sequence determinants control human and mouse receptor interacting protein 3 (RIP3) and mixed lineage kinase domain-like (MLKL) interaction in necroptotic signaling.* J Biol Chem, 2013. **288**(23): p. 16247-61.

172. Guo, H., et al., *Species-independent contribution of ZBP1/DAI/DLM-1-triggered necroptosis in host defense against HSV1.* Cell Death Dis, 2018. **9**(8): p. 816.

173. Guo, H., et al., *Herpes simplex virus suppresses necroptosis in human cells.* Cell Host Microbe, 2015. **17**(2): p. 243-51.

174. Omoto, S., et al., *Suppression of RIP3-dependent necroptosis by human cytomegalovirus.* J Biol Chem, 2015. **290**(18): p. 11635-48.

175. Pearson, J.S., et al., *EspL is a bacterial cysteine protease effector that cleaves RHIM proteins to block necroptosis and inflammation.* Nat Microbiol, 2017. **2**: p. 16258.

176. Upton, J.W., W.J. Kaiser, and E.S. Mocarski, *Virus inhibition of RIP3-dependent necrosis.* Cell Host Microbe, 2010. **7**(4): p. 302-13.

177. Wang, H., et al., *Mixed lineage kinase domain-like protein MLKL causes necrotic membrane disruption upon phosphorylation by RIP3.* Mol Cell, 2014. **54**(1): p. 133-146.

178. Murphy, J.M., et al., *The pseudokinase MLKL mediates necroptosis via a molecular switch mechanism.* Immunity, 2013. **39**(3): p. 443-53.

179. Manning, G., et al., *The protein kinase complement of the human genome.* Science, 2002. **298**(5600): p. 1912-34.

180. Hildebrand, J.M., et al., *Activation of the pseudokinase MLKL unleashes the four-helix bundle domain to induce membrane localization and necroptotic cell death.* Proc Natl Acad Sci U S A, 2014. **111**(42): p. 15072-7.

181. Petrie, E.J., et al., *Conformational switching of the pseudokinase domain promotes human MLKL tetramerization and cell death by necroptosis.* Nat Commun, 2018. **9**(1): p. 2422.

182. Davies, K.A., et al., *The brace helices of MLKL mediate interdomain communication and oligomerisation to regulate cell death by necroptosis.* Cell Death Differ, 2018.

183. Xie, T., et al., *Structural insights into RIP3-mediated necroptotic signaling.* Cell Rep, 2013. **5**(1): p. 70-8.

184. Rodriguez, D.A., et al., *Characterization of RIPK3-mediated phosphorylation of the activation loop of MLKL during necroptosis.* Cell Death Differ, 2015.

185. Tanzer, M.C., et al., *Necroptosis signalling is tuned by phosphorylation of MLKL residues outside the pseudokinase domain activation loop.* Biochem J, 2015. **471**(2): p. 255-65.

186. Daub, H., et al., *Kinase-selective enrichment enables quantitative phosphoproteomics of the kinome across the cell cycle.* Mol Cell, 2008. **31**(3): p. 438-48.

187. Dephoure, N., et al., *A quantitative atlas of mitotic phosphorylation.* Proc Natl Acad Sci U S A, 2008. **105**(31): p. 10762-7.

188. Cai, Z., et al., *Plasma membrane translocation of trimerized MLKL protein is required for TNF-induced necroptosis.* Nat Cell Biol, 2014. **16**(1): p. 55-65.

189. Wang, H., et al., *Mixed lineage kinase domain-like protein MLKL causes necrotic membrane disruption upon phosphorylation by RIP3.* Mol Cell, 2014. **54**(1): p. 133-46.

190. Huang, D., et al., *MLKL channel in necroptosis is octamer formed by tetramers in a dyadic process.* Mol Cell Biol, 2016.

191. Liu, S., et al., *MLKL forms disulfide bond-dependent amyloid-like polymers to induce necroptosis.* Proc Natl Acad Sci U S A, 2017. **114**(36): p. E7450-e7459.

192. Petrie, E.J., J.M. Hildebrand, and J.M. Murphy, *Insane in the membrane: a structural perspective of MLKL function in necroptosis.* Immunol Cell Biol, 2017. **95**(2): p. 152-159.

193. Chen, X., et al., *Translocation of mixed lineage kinase domain-like protein to plasma membrane leads to necrotic cell death.* Cell Res, 2014. **24**(1): p. 105-21.

194. Dondelinger, Y., et al., *MLKL compromises plasma membrane integrity by binding to phosphatidylinositol phosphates.* Cell Rep, 2014. **7**(4): p. 971-81.

195. Quarato, G., et al., *Sequential Engagement of Distinct MLKL Phosphatidylinositol-Binding Sites Executes Necroptosis.* Mol Cell, 2016. **61**(4): p. 589-601.

196. Ros, U., et al., *Necroptosis Execution Is Mediated by Plasma Membrane Nanopores Independent of Calcium.* Cell Rep, 2017. **19**(1): p. 175-187.

197. Daskalov, A., et al., *Identification of a novel cell death-inducing domain reveals that fungal amyloid-controlled programmed cell death is related to necroptosis.* Proc Natl Acad Sci U S A, 2016. **113**(10): p. 2720-5.

198. Tanzer, M.C., et al., *Evolutionary divergence of the necroptosis effector MLKL.* Cell Death Differ, 2016.

199. Gong, Y.N., et al., *ESCRT-III Acts Downstream of MLKL to Regulate Necroptotic Cell Death and Its Consequences.* Cell, 2017. **169**(2): p. 286-300.e16.

200. Yoon, S., et al., *MLKL, the Protein that Mediates Necroptosis, Also Regulates Endosomal Trafficking and Extracellular Vesicle Generation.* Immunity, 2017. **47**(1): p. 51-65.e7.

201. Pasparakis, M. and P. Vandenabeele, *Necroptosis and its role in inflammation.* Nature, 2015. **517**(7534): p. 311-20.

202. Feoktistova, M., et al., *cIAPs block Ripoptosome formation, a RIP1/caspase-8 containing intracellular cell death complex differentially regulated by cFLIP isoforms.* Mol Cell, 2011. **43**(3): p. 449-63.

203. Geserick, P., et al., *Cellular IAPs inhibit a cryptic CD95-induced cell death by limiting RIP1 kinase recruitment.* J Cell Biol, 2009. **187**(7): p. 1037-54.

204. Varfolomeev, E., et al., *Molecular determinants of kinase pathway activation by Apo2 ligand/tumor necrosis factor-related apoptosis-inducing ligand.* J Biol Chem, 2005. **280**(49): p. 40599-608.

205. Jouan-Lanhouet, S., et al., *TRAIL induces necroptosis involving RIPK1/RIPK3-dependent PARP-1 activation.* Cell Death Differ, 2012. **19**(12): p. 2003-14.

206. Lafont, E., et al., *The linear ubiquitin chain assembly complex regulates TRAIL-induced gene activation and cell death.* Embo j, 2017. **36**(9): p. 1147-1166.

207. Lafont, E., T. Hartwig, and H. Walczak, *Paving TRAIL's Path with Ubiquitin.* Trends Biochem Sci, 2018. **43**(1): p. 44-60.

208. Kaiser, W.J. and M.K. Offermann, *Apoptosis induced by the toll-like receptor adaptor TRIF is dependent on its receptor interacting protein homotypic interaction motif.* J Immunol, 2005. **174**(8): p. 4942-52.

209. Kaiser, W.J., et al., *Toll-like receptor 3-mediated necrosis via TRIF, RIP3, and MLKL.* J Biol Chem, 2013. **288**(43): p. 31268-79.

210. He, S., et al., *Toll-like receptors activate programmed necrosis in macrophages through a receptor-interacting kinase-3-mediated pathway.* Proc Natl Acad Sci U S A, 2011. **108**(50): p. 20054-9.

211. Tenev, T., et al., *The Ripoptosome, a signaling platform that assembles in response to genotoxic stress and loss of IAPs.* Mol Cell, 2011. **43**(3): p. 432-48.

212. Meylan, E., et al., *RIP1 is an essential mediator of Toll-like receptor 3-induced NF-kappa B activation.* Nat Immunol, 2004. **5**(5): p. 503-7.

213. Polykratis, A., et al., *Cutting edge: RIPK1 Kinase inactive mice are viable and protected from TNF-induced necroptosis in vivo.* J Immunol, 2014. **193**(4): p. 1539-1543.

214. Takaoka, A., et al., *DAI (DLM-1/ZBP1) is a cytosolic DNA sensor and an activator of innate immune response.* Nature, 2007. **448**(7152): p. 501-5.

215. Kaiser, W.J., J.W. Upton, and E.S. Mocarski, *Receptor-interacting protein homotypic interaction motif-dependent control of NF-kappa B activation via the DNA-dependent activator of IFN regulatory factors.* J Immunol, 2008. **181**(9): p. 6427-34.

216. Wang, Z., et al., *Regulation of innate immune responses by DAI (DLM-1/ZBP1) and other DNA-sensing molecules.* Proc Natl Acad Sci U S A, 2008. **105**(14): p. 5477-82.

217. Thapa, R.J., et al., *DAI Senses Influenza A Virus Genomic RNA and Activates RIPK3-Dependent Cell Death.* Cell Host Microbe, 2016.

218. Maelfait, J., et al., *Sensing of viral and endogenous RNA by ZBP1/DAI induces necroptosis.* Embo j, 2017. **36**(17): p. 2529-2543.

219. Sridharan, H., et al., *Murine cytomegalovirus IE3-dependent transcription is required for DAI/ZBP1-mediated necroptosis.* EMBO Rep, 2017. **18**(8): p. 1429-1441.

220. Kuriakose, T. and T.D. Kanneganti, *ZBP1: Innate Sensor Regulating Cell Death and Inflammation.* Trends Immunol, 2018. **39**(2): p. 123-134.

221. Rebsamen, M., et al., *DAI/ZBP1 recruits RIP1 and RIP3 through RIP homotypic interaction motifs to activate NF-kappaB.* EMBO Rep, 2009. **10**(8): p. 916-22.

222. Upton, J.W. and W.J. Kaiser, *DAI Another Way: Necroptotic Control of Viral Infection.* Cell Host Microbe, 2017. **21**(3): p. 290-293.

223. Guo, H., W.J. Kaiser, and E.S. Mocarski, *Manipulation of apoptosis and necroptosis signaling by herpesviruses.* Med Microbiol Immunol, 2015. **204**(3): p. 439-48.

224. Huang, Z., et al., *RIP1/RIP3 binding to HSV-1 ICP6 initiates necroptosis to restrict virus propagation in mice.* Cell Host Microbe, 2015. **17**(2): p. 229-42.

225. Upton, J.W., W.J. Kaiser, and E.S. Mocarski, *Cytomegalovirus M45 cell death suppression requires receptor-interacting protein (RIP) homotypic interaction motif (RHIM)-dependent interaction with RIP1.* J Biol Chem, 2008. **283**(25): p. 16966-70.

226. Upton, J.W., W.J. Kaiser, and E.S. Mocarski, *DAI/ZBP1/DLM-1 complexes with RIP3 to mediate virus-induced programmed necrosis that is targeted by murine cytomegalovirus vIRA.* Cell Host Microbe, 2012. **11**(3): p. 290-7.

227. Lin, J., et al., *RIPK1 counteracts ZBP1-mediated necroptosis to inhibit inflammation.* Nature, 2016. **540**(7631): p. 124-128.

228. Newton, K., et al., *RIPK1 inhibits ZBP1-driven necroptosis during development.* Nature, 2016. **540**(7631): p. 129-133.

229. Gonzalez-Navajas, J.M., et al., *Immunomodulatory functions of type I interferons.* Nat Rev Immunol, 2012. **12**(2): p. 125-35.

230. Thapa, R.J., et al., *Interferon-induced RIP1/RIP3-mediated necrosis requires PKR and is licensed by FADD and caspases.* Proc Natl Acad Sci U S A, 2013. **110**(33): p. E3109-18.

231. McComb, S., et al., *Type-I interferon signaling through ISGF3 complex is required for sustained Rip3 activation and necroptosis in macrophages.* Proc Natl Acad Sci U S A, 2014. **111**(31): p. E3206-13.

232. Legarda, D., et al., *CYLD Proteolysis Protects Macrophages from TNF-Mediated Auto-necroptosis Induced by LPS and Licensed by Type I IFN.* Cell Rep, 2016. **15**(11): p. 2449-61.

233. Sarhan, J., et al., *Constitutive interferon signaling maintains critical threshold of MLKL expression to license necroptosis.* Cell Death Differ, 2019. **26**(2): p. 332-347.

234. Brault, M., et al., *Intracellular Nucleic Acid Sensing Triggers Necroptosis through Synergistic Type I IFN and TNF Signaling.* J Immunol, 2018. **200**(8): p. 2748-2756.

235. Ingram, J.P., et al., *ZBP1/DAI Drives RIPK3-Mediated Cell Death Induced by IFNs in the Absence of RIPK1.* J Immunol, 2019.

236. Rickard, J.A., et al., *RIPK1 regulates RIPK3-MLKL-driven systemic inflammation and emergency hematopoiesis.* Cell, 2014. **157**(5): p. 1175-88.

237. Dillon, C.P., et al., *RIPK1 blocks early postnatal lethality mediated by caspase-8 and RIPK3.* Cell, 2014. **157**(5): p. 1189-202.

238. Kaiser, W.J., et al., *RIP1 suppresses innate immune necrotic as well as apoptotic cell death during mammalian parturition.* Proc Natl Acad Sci U S A, 2014. **111**(21): p. 7753-8.

239. Frank, T., et al., *Cell cycle arrest in mitosis promotes interferon-induced necroptosis.* Cell Death Differ, 2019.

240. de Almagro, M.C., et al., *Cellular IAP proteins and LUBAC differentially regulate necrosome-associated RIP1 ubiquitination.* Cell Death Dis, 2015. **6**: p. e1800.

241. de Almagro, M.C., et al., *Coordinated ubiquitination and phosphorylation of RIP1 regulates necroptotic cell death.* Cell Death Differ, 2016.

242. Wang, H., et al., *PELI1 functions as a dual modulator of necroptosis and apoptosis by regulating ubiquitination of RIPK1 and mRNA levels of c-FLIP.* Proc Natl Acad Sci U S A, 2017. **114**(45): p. 11944-11949.

243. Seo, J., et al., *CHIP controls necroptosis through ubiquitylation- and lysosome-dependent degradation of RIPK3.* Nat Cell Biol, 2016. **18**(3): p. 291-302.

244. Lee, S.B., et al., *The AMPK-Parkin axis negatively regulates necroptosis and tumorigenesis by inhibiting the necrosome.* Nat Cell Biol, 2019. **21**(8): p. 940-951.

245. Choi, S.W., et al., *PELI1 Selectively Targets Kinase-Active RIP3 for Ubiquitylation-Dependent Proteasomal Degradation.* Mol Cell, 2018. **70**(5): p. 920-935.e7.

246. Onizawa, M., et al., *The ubiquitin-modifying enzyme A20 restricts ubiquitination of the kinase RIPK3 and protects cells from necroptosis.* Nat Immunol, 2015. **16**(6): p. 618-27.

247. Kesavardhana, S., et al., *ZBP1/DAI ubiquitination and sensing of influenza vRNPs activate programmed cell death.* J Exp Med, 2017. **214**(8): p. 2217-2229.

248. Lawlor, K.E., et al., *RIPK3 promotes cell death and NLRP3 inflammasome activation in the absence of MLKL.* Nat Commun, 2015. **6**: p. 6282.

249. Hjerpe, R., et al., *Efficient protection and isolation of ubiquitylated proteins using tandem ubiquitin-binding entities.* EMBO Rep, 2009. **10**(11): p. 1250-8.

250. Sims, J.J., et al., *Polyubiquitin-sensor proteins reveal localization and linkage-type dependence of cellular ubiquitin signaling.* Nat Methods, 2012. **9**(3): p. 303-9.

251. Fiil, B.K., et al., *OTULIN restricts Met1-linked ubiquitination to control innate immune signaling.* Mol Cell, 2013. **50**(6): p. 818-830.

252. Wu, Y.T., et al., *zVAD-induced necroptosis in L929 cells depends on autocrine production of TNFalpha mediated by the PKC-MAPKs-AP-1 pathway.* Cell Death Differ, 2011. **18**(1): p. 26-37.

253. Cai, Z. and Z.G. Liu, *Detection of MLKL Oligomerization During Programmed Necrosis.* Methods Mol Biol, 2018. **1857**: p. 85-92.

254. Keusekotten, K., et al., *OTULIN antagonizes LUBAC signaling by specifically hydrolyzing Met1-linked polyubiquitin.* Cell, 2013. **153**(6): p. 1312-26.

255. Hospenthal, M.K., T.E.T. Mevissen, and D. Komander, *Deubiquitinase-based analysis of ubiquitin chain architecture using Ubiquitin Chain Restriction (UbiCRest).* Nat. Protocols, 2015. **10**(2): p. 349-361.

256. Hanks, S.K., A.M. Quinn, and T. Hunter, *The protein kinase family: conserved features and deduced phylogeny of the catalytic domains.* Science, 1988. **241**(4861): p. 42-52.

257. Hu, J., et al., *Mutation that blocks ATP binding creates a pseudokinase stabilizing the scaffolding function of kinase suppressor of Ras, CRAF and BRAF.* Proc Natl Acad Sci U S A, 2011. **108**(15): p. 6067-72.

258. Kannan, N., et al., *Structural and functional diversity of the microbial kinome.* PLoS Biol, 2007. **5**(3): p. e17.

259. Cheung, J., et al., *Structural insights into mis-regulation of protein kinase A in human tumors.* Proc Natl Acad Sci U S A, 2015. **112**(5): p. 1374-9.

260. Martin-Vicente, M., et al., *TRIM25 in the Regulation of the Antiviral Innate Immunity.* Front Immunol, 2017. **8**: p. 1187.

261. Hatakeyama, S., *TRIM proteins and cancer.* Nat Rev Cancer, 2011. **11**(11): p. 792-804.

262. Napolitano, L.M. and G. Meroni, *TRIM family: Pleiotropy and diversification through homomultimer and heteromultimer formation.* IUBMB Life, 2012. **64**(1): p. 64-71.

263. Rajsbaum, R., A. Garcia-Sastre, and G.A. Versteeg, *TRIMmunity: the roles of the TRIM E3-ubiquitin ligase family in innate antiviral immunity.* J Mol Biol, 2014. **426**(6): p. 1265-84.

264. Koliopoulos, M.G., et al., *Functional role of TRIM E3 ligase oligomerization and regulation of catalytic activity.* Embo j, 2016.

265. Gack, M.U., et al., *TRIM25 RING-finger E3 ubiquitin ligase is essential for RIG-I-mediated antiviral activity.* Nature, 2007. **446**(7138): p. 916-920.

266. Gack, M.U., et al., *Roles of RIG-I N-terminal tandem CARD and splice variant in TRIM25-mediated antiviral signal transduction.* Proc Natl Acad Sci U S A, 2008. **105**(43): p. 16743-8.

267. Okamoto, M., et al., *Regulation of RIG-I Activation by K63-Linked Polyubiquitination.* Front Immunol, 2017. **8**: p. 1942.

268. Fan, W., et al., *Flotillin-mediated endocytosis and ALIX-syntenin-1-mediated exocytosis protect the cell membrane from damage caused by necroptosis.* Sci Signal, 2019. **12**(583).

269. Chazotte, B., *Labeling membrane glycoproteins or glycolipids with fluorescent wheat germ agglutinin.* Cold Spring Harb Protoc, 2011. **2011**(5): p. pdb.prot5623.

270. Mobitz, H., *The ABC of protein kinase conformations.* Biochim Biophys Acta, 2015. **1854**(10 Pt B): p. 1555-66.

271. Beltrao, P., et al., *Systematic functional prioritization of protein posttranslational modifications.* Cell, 2012. **150**(2): p. 413-25.

272. Sagar, G.D., et al., *Ubiquitination-induced conformational change within the deiodinase dimer is a switch regulating enzyme activity.* Mol Cell Biol, 2007. **27**(13): p. 4774-83.

273. Ball, K.A., et al., *Non-degradative Ubiquitination of Protein Kinases.* PLoS Comput Biol, 2016. **12**(6): p. e1004898.

274. Fottner, M., et al., *Site-specific ubiquitylation and SUMOylation using genetic-code expansion and sortase.* Nat Chem Biol, 2019. **15**(3): p. 276-284.

275. Ordureau, A., C. Münch, and J.W. Harper, *Quantifying ubiquitin signaling.* Mol Cell, 2015. **58**(4): p. 660-76.

276. Taylor, S.S., et al., *Evolution of the eukaryotic protein kinases as dynamic molecular switches.* Philos Trans R Soc Lond B Biol Sci, 2012. **367**(1602): p. 2517-28.

277. Murphy, J.M., et al., *Insights into the evolution of divergent nucleotide-binding mechanisms among pseudokinases revealed by crystal structures of human and mouse MLKL.* Biochem J, 2014. **457**(3): p. 369-77.

278. Akimov, V., et al., *UbiSite approach for comprehensive mapping of lysine and N-terminal ubiquitination sites.* Nat Struct Mol Biol, 2018. **25**(7): p. 631-640.

279. Dondelinger, Y., et al., *An evolutionary perspective on the necroptotic pathway.* Trends Cell Biol, 2016. **26**(10): p. 721-732.

280. Petrie, E.J., et al., *Viral MLKL Homologs Subvert Necroptotic Cell Death by Sequestering Cellular RIPK3.* Cell Rep, 2019. **28**(13): p. 3309-3319.e5.

281. Choi, M.E., et al., *Necroptosis: a crucial pathogenic mediator of human disease.* JCI Insight, 2019. **4**(15).

282. Orozco, S. and A. Oberst, *RIPK3 in cell death and inflammation: the good, the bad, and the ugly.* Immunol Rev, 2017. **277**(1): p. 102-112.

283. Newton, K., et al., *RIPK3 deficiency or catalytically inactive RIPK1 provides greater benefit than MLKL deficiency in mouse models of inflammation and tissue injury.* Cell Death Differ, 2016.

284. Newton, K., *Multitasking Kinase RIPK1 Regulates Cell Death and Inflammation.* Cold Spring Harb Perspect Biol, 2019.

285. Cao, K. and S.W.G. Tait, *Parkin inhibits necroptosis to prevent cancer.* Nat Cell Biol, 2019. **21**(8): p. 915-916.

286. Jin, Z., et al., *Cullin3-based polyubiquitination and p62-dependent aggregation of caspase-8 mediate extrinsic apoptosis signaling.* Cell, 2009. **137**(4): p. 721-35.

287. Gonzalvez, F., et al., *TRAF2 Sets a threshold for extrinsic apoptosis by tagging caspase-8 with a ubiquitin shutoff timer.* Mol Cell, 2012. **48**(6): p. 888-99.

288. Morgan, M.J. and Y.S. Kim, *The serine threonine kinase RIP3: lost and found.* BMB Rep, 2015. **48**(6): p. 303-12.

289. Hayman, T.J., et al., *RIPLET, and not TRIM25, is required for endogenous RIG-I-dependent antiviral responses.* Immunol Cell Biol, 2019.

290. Delva, E., D.K. Tucker, and A.P. Kowalczyk, *The desmosome.* Cold Spring Harb Perspect Biol, 2009. **1**(2): p. a002543.

291. Maupin, P. and T.D. Pollard, *Arrangement of actin filaments and myosin-like filaments in the contractile ring and of actin-like filaments in the mitotic spindle of dividing HeLa cells.* J Ultrastruct Mol Struct Res, 1986. **94**(1): p. 92-103.

292. Rosenblatt, J., M.C. Raff, and L.P. Cramer, *An epithelial cell destined for apoptosis signals its neighbors to extrude it by an actin- and myosin-dependent mechanism.* Curr Biol, 2001. **11**(23): p. 1847-57.

293. Hogan, C., et al., *Characterization of the interface between normal and transformed epithelial cells.* Nat Cell Biol, 2009. **11**(4): p. 460-7.

294. Schwayer, C., et al., *Actin Rings of Power.* Dev Cell, 2016. **37**(6): p. 493-506.

295. Zhang, J., et al., *Actin at cell-cell junctions is composed of two dynamic and functional populations.* J Cell Sci, 2005. **118**(Pt 23): p. 5549-62.

296. Su, L., et al., *A plug release mechanism for membrane permeation by MLKL.* Structure, 2014. **22**(10): p. 1489-500.

297. Dovey, C.M., et al., *MLKL Requires the Inositol Phosphate Code to Execute Necroptosis.* Mol Cell, 2018. **70**(5): p. 936-948.e7.

298. Mulvihill, E., et al., *Mechanism of membrane pore formation by human gasdermin-D.* Embo j, 2018. **37**(14).

299. Salvador-Gallego, R., et al., *Bax assembly into rings and arcs in apoptotic mitochondria is linked to membrane pores.* Embo j, 2016. **35**(4): p. 389-401.

300. Grosse, L., et al., *Bax assembles into large ring-like structures remodeling the mitochondrial outer membrane in apoptosis.* Embo j, 2016. **35**(4): p. 402-13.

301. Ding, J., et al., *Pore-forming activity and structural autoinhibition of the gasdermin family.* Nature, 2016. **535**(7610): p. 111-6.

302. Mocarski, E.S., J.W. Upton, and W.J. Kaiser, *Viral infection and the evolution of caspase 8-regulated apoptotic and necrotic death pathways.* Nat Rev Immunol, 2012. **12**(2): p. 79-88.

303. Xu, K., G. Zhong, and X. Zhuang, *Actin, spectrin, and associated proteins form a periodic cytoskeletal structure in axons.* Science, 2013. **339**(6118): p. 452-6.